RAI Volume 3, Chapter 2.2.1.3.6, First Set, Number 2:

Explain how the TSPA seepage conceptualization and abstraction are consistent with observations and interpretations of the presence of liquid water in the Passive Test in the Enhanced Characterization of the Repository Block (ECRB) drift.

Explain how the volume of water entering a drift is not underestimated by the TSPA seepage abstraction, which neglects vapor migration into the drifts through fractures or other air pathways, redistribution within the drift, and subsequent condensation. See related RAI from Scenario Chapter, Set 5, RAI #3. This information is needed to verify compliance with 10 CFR 63.114(a), (c), (e), and (g).

Basis: DOE concluded (SAR Section 2.3.3.2.2.2) that observations related to the presence of liquid water in the Passive Test were consistent with condensation, and not consistent with water dripping into the drift. The distribution of water in the drift of the Passive Test is qualitatively explained by condensation after gas-phase redistribution driven by small temperature and relative humidity variations (SAR Section 2.3.3.2.2.2.5). Similar variations of temperature and relative humidity would be expected to occur after the thermal perturbation period in emplacement drifts, in both the 10,000-yr and post-10,000-yr periods. Open vapor air pathways may include interconnected fractures and other pathways, such as open boreholes.

Salve and Kneafsey (2005) describe how observations of liquid water in the Passive Test (BSC, 2004, Section 6.10.2.2) of the ECRB drift can be explained using a conceptual model of vapor migration through the fracture network and into the drift. They describe three models for vapor flux into the drift, and the degree to which each model appears to best fit the observations of hydrologic conditions and liquid water in the drift. In their models that best fit the observations, vapor migration through the fracture network acts as the supply of water to the in-drift environment. Salve and Kneafsey (2005) suggest that evaporation directly from the drift wall surface did not appear adequate as a supply of water to support observations.

The origin of liquid water in drifts during the later stages of the thermal period and continuing through the ambient period may be a combination of condensation and seepage. The in-drift condensation submodel (SAR Section 2.3.5.4.2.4) does not account for the processes nor the period of concern mentioned in this RAI.

1. RESPONSE

This response explains how the DOE abstraction estimate of the contribution of in-drift condensation is consistent with observation of condensation within the closed nonventilated sections of the Enhanced Characterization of the Repository Block (ECRB). The total system performance assessment (TSPA) seepage conceptualization and abstraction are consistent with observations and interpretations of the presence of liquid water in the Passive Test within the ECRB. Condensation as implemented in TSPA conservatively estimates the rate of vapor influx into the drifts and is consistent with the models of vapor influx into drifts discussed by Salve and Kneafsey (2005). The models analyzed by Salve and Kneafsey (2005) relate to and are in agreement with the model vapor influx into the drift implemented in the TSPA condensation model. The analysis shows minimal effects of vapor flux through rockbolt boreholes on the available moisture and the potential for condensation within the drift. The response to RAI 3.2.2.1.3.6-003 presents the effects of liquid/vapor reflux in these open rockbolt boreholes. The analysis provided in this response shows that the TSPA condensation model incorporates the contribution of condensation to the liquid volume of water entering the drift, and the effect of vapor influx and liquid/vapor reflux, through open rockbolt boreholes, on this estimate is negligible.

1.1 SEEPAGE CONCEPTUALIZATION AND CONSISTENCY WITH ECRB OBSERVATIONS

The seepage model used for the TSPA represents the liquid-phase hydrologic processes in the host rock that control the influx of water to the emplacement drifts (SAR Sections 2.3.3.2 and 2.3.3.3). The TSPA seepage abstraction provides an estimate of the liquid flux entering drift under both ambient and thermally perturbed conditions (SAR Section 2.3.3.4). In addition to the seepage, the volume of liquid water generated by the exchange of vapor between the host rock and drifts, as inferred by Salve and Kneafsey (2005) from the ECRB observations, is considered in the in-drift condensation model (SAR Section 2.3.5.4.2) and in thermal-hydrologic simulations developed for model support (SAR Section 2.3.5.4.1).

The conceptual framework for seepage modeling does not include the reduction of seepage by evaporation in the repository as a model simplification, and therefore it is conservative with respect to the availability of water for interaction with the Engineered Barrier System (EBS) (SAR Section 2.3.3.2.1.2). Vapor influx to the drifts is considered in the condensation model, where heating is included; if gas-phase processes were included in the seepage model, a consistent treatment would include evaporative reduction of seepage by the lower humidity associated with warmer drift conditions. Both condensation and seepage contribute to liquid water flux in the EBS, which is represented in the TSPA by summing the contributions from both condensation and seepage models. The vapor flux and condensation processes that contribute to the observed ECRB conditions are addressed in the condensation model. Therefore, the conceptual basis for seepage modeling is consistent with the ECRB observations.

1.2 COMPARISON OF THE IN-DRIFT CONDENSATION MODEL WITH ECRB OBSERVATIONS

Thermal gradients in the repository may lead to condensation of moisture in cooler parts of the emplacement drifts. Such effects are included in the TSPA using the condensation model (SAR Section 2.3.5.4.2). The condensation model describes the phenomena of evaporation of water from the drift wall and invert, transport of water along the drift, and condensation at cooler locations. There are two outcomes of these processes that bound the possibilities for condensation. If axial transport of water vapor is sufficiently strong, condensation will occur only in unheated parts of the emplacement drifts, and relative humidity in the emplacement areas will be low. Alternatively, if axial transport is limited, relative humidity will be higher and local condensation in the emplacement area may occur (SNL 2007, Sections 6.3.7.2 and 6.1[a]).

As discussed in SAR Section 2.3.5.4.2, observations from the Passive Test in the ECRB showed that evaporation and condensation occur in response to small thermal gradients and, by inference, could be important processes in the repository. Parts of the ECRB that were in the vicinity of heat sources (heat from the tunnel boring machine) remained dry, while adjacent unheated regions were wet. Condensate was observed on thermally conductive surfaces after the ECRB bulkhead doors had been closed for periods ranging from several weeks to a few months (BSC 2004, Section 6.10.2.2; Figure 6-113). The ECRB observations are consistent with the condensation model representation that moisture can: (1) evaporate from warmer areas, (2) migrate along the drift as vapor driven by natural convection processes, and (3) condense at cooler locations. In the repository, water from the rock will evaporate from the drift walls at warmer locations and condense at colder locations. For certain conditions, condensation may occur at cooler waste package locations. The rates of evaporation and condensation, as well as the rate of water vapor transport in the drift, will determine the humidity in the drift and the extent of condensation.

As implemented in the TSPA (SNL 2008, Section 6.3.3.2), the condensation model assumes "wet" drift walls (partial H_2O pressure equal to the saturated vapor pressure) at all waste package locations, subject only to the constraint that the total evaporation not exceed the percolation flux incident on the drift plus the contribution of capillary pumping. This condition maximizes the availability of moisture for evaporation, and potentially causes the rate of condensation to be overestimated, because it does not account for: (1) lowering of capillary vapor pressure in the rock at the drift wall as a result of evaporation from the rock surface, or (2) flow resistance that vapor transport would encounter through a zone of relatively dry rock around the opening. Nevertheless, the resulting condensation is predicted to occur mostly outside the heated area (SNL 2007, Section 6.3.3.1). Salve and Kneafsey (2005) considered and rejected direct evaporation from water films at the drift-wall because it acted too quickly, not because it could not provide the observed moisture flux. Hence, the condensation model boundary condition (which uses 100% relative humidity at the drift-wall and therefore provides moisture at a faster rate than observed in the ECRB test) is conservative with respect to the availability of water to enter the emplacement drifts as vapor, and is consistent with the analysis by Salve and Kneafsey (2005).

Finally, the in-drift condensation model does apply to the 10,000-year and post-10,000-year periods mentioned in the RAI, but condensation in the emplacement areas is not predicted throughout much of this period for many of the cases considered. Cases included in the model documentation extend to 300,000 years (SNL 2007, Section 6.1[a]). The model documentation recognizes three stages of thermal-hydrologic behavior driving potential condensation (SNL 2007, Section 6.3.3.1). This RAI response relates to Stage 3 only, when the entire drift and the surfaces of the waste packages have cooled to below the boiling temperature. No condensation is possible in Stage 1, and the TSPA represents Stage 2 by a bounding approximation (SNL 2007, Section 6.2[a]). During Stage 2, the production and transport of water vapor are strongly thermally driven and are not closely comparable to conditions in the ECRB passive test. The analysis of Salve and Kneafsey (2005) did not address strongly thermally driven processes.

1.3 DISCUSSION OF THE RESULTS FROM SALVE AND KNEAFSEY (2005)

Salve and Kneafsey (2005) analyzed how transient rehydration of the ECRB drift segments occurred after the bulkheads were closed, following periods of active ventilation. During ventilation, the ECRB drift warmed and dried out, and moisture was extracted from the rock because of the negative ventilation pressure. After isolation, the drift and surrounding rock cooled and became more humid, to the point where condensation occurred as discussed earlier. Salve and Kneafsey (2005) evaluated three models that describe the transient influx of water vapor into the drift:

- Advection of air through the mountain (mixing)—the mixed tank model
- Molecular diffusion into the drift from a 100% relative humidity boundary at the drift wall, equivalent to the "wet" drift-wall boundary condition used in the condensation model—the diffusion model
- Diffusion of water vapor from a 100% relative humidity boundary within the rock, beyond a dryout zone around the opening, through the fracture network (with fluid flow assumed to be inactive)—the diffusion through inactive rind model.

The authors (Salve and Kneafsey 2005) suggested that evaporation directly from the drift wall surface did not appear adequate as a supply of water to support observations. As stated, this suggestion is not supported by the results. The diffusion-only model and diffusion model with an inactive 1-cm rind both produced vapor influx at a faster rate than observed in the passive test (Salve and Kneafsey 2005, Figure 11). Better agreement was obtained with the mixing model and the diffusion model with an inactive 5-cm rind, indicating there is resistance to mass transfer between the host rock and the drift opening. Importantly, the transient rate of moisture influx observed by Salve and Kneafsey (2005) does not represent repository conditions, which will be slowly varying over thousands of years. The availability of moisture for condensation in the repository is bounded by the "wet" drift-wall boundary condition used in the condensation model.

Of the two mechanisms for vapor transport that Salve and Kneafsey (2005) concluded were plausible for the rehydration of the ECRB drift, diffusion of water vapor into the drift is included explicitly in the thermal-hydrologic models that support performance assessment. The three-dimensional thermal-hydrologic models used to validate the multiscale model (SAR Section 2.3.5.4.1) and to develop the bounding abstraction for drift-wall condensation during Stage 2 (SNL 2007, Section 6.2.2[a]), include the migration of water vapor through a dryout zone, into the emplacement drift.

The other mechanism proposed by Salve and Kneafsey (2005) was gas-phase advection in response to large-scale pressure gradients. This mechanism is essentially the same as the barometric pumping effect that has been evaluated with respect to the effect on in-drift condensation (SAR Section 2.3.5.4.2.1). Large-scale gas flow in or near the repository will be dominated by the emplacement drifts, access drifts, and exhaust drifts, all of which are likely to remain open to gas flow for many thousands of years. In other words, the presence of these openings will ensure that most gas movement in response to far-field conditions (e.g., barometric pressure changes) will take place along the openings. The effect of axial gas movement into or out of the heated parts of an emplacement drift will be to dry out the drift and the surrounding rock (SNL 2007, p. 6-113). This is consistent with the advective mechanism proposed by Salve and Kneafsey (2005) when their concept is applied to actual repository conditions. Thus, both mechanisms favored by Salve and Kneafsey (2005) are part of the conceptual framework for the thermal-hydrologic model and the condensation model that support performance assessment.

1.4 VAPOR INFLUX THROUGH OPEN ROCKBOLT BOREHOLES IN THE DRIFT WALL

This section considers the effects of vapor flux through other pathways (including open boreholes drilled through the drift walls) as requested by NRC during the clarification call for RAI 3.2.2.1.3.6-002. The RAI and clarifying information propose that vapor influx through open boreholes into the emplacement drifts, similar to the influx observed by Salve and Keafsey (2005) into the ECRB drift, could introduce enough moisture to cause condensation that is not represented by the condensation or drift seepage models. The hypothesis is that open boreholes, such as those used for rock bolts, may act as pathways that increase the availability of moisture beyond what is represented in the models and, therefore, increase the rate or extent of drift-wall condensation beyond what is predicted.

As discussed in the condensation model description (SAR Section 2.3.5.4.2.1), condensation cannot occur anywhere in the emplacement drifts while the host-rock temperature is greater than boiling (initial cooling stage). During this stage water vapor will be generated as the host rock moisture and incident percolation flux are vaporized. Some of this vapor will enter the drift opening, and migrate to cooler, unheated parts of the drift where it will condense. After the drift wall temperature cools below boiling in parts of the drift (intermediate cooling stage), condensation is possible at the locations of the coolest waste packages (SAR Section 2.3.5.4.2.3.2). Eventually the drift-wall temperature cools below boiling along the entire length of the emplacement drift (final cooling stage) and condensation becomes increasingly likely, depending on percolation flux in the rock, and the axial mobility of water vapor in the drift.

Open rockbolt boreholes may contribute to the availability of moisture for evaporation during the hottest part of the thermal period (within approximately 2,000 years after repository closure), but in later time the rate of evaporation decreases substantially. Evaporation and condensation as represented by the condensation model (SAR Section 2.3.5.4.2) show that there is limited potential for open boreholes to increase condensation. The primary reasons are that: 1) water vapor migrates away from the heated parts of the drift and condenses in the unheated parts, regardless of the percolation flux; and 2) the rate of evaporation from the rock approaches zero because the vapor mass fraction of the gas in the drift approaches the equilibrium vapor mass fraction for the prevailing temperature at the drift wall.

Drift-wall condensation occurs only for the 1,000-year case used for the TSPA (SAR Section 2.3.5.4.2.4), which is applied during the final cooling stage, but only from when the drift wall cools below boiling until 2,000 years after closure. During this period, evaporation occurs near the center of each emplacement drift, and condensation occurs closer to the ends (example results for Drift #7 from the model are plotted in Figure 1). Importantly, for the 1,000-year case, when drift-wall condensation can occur, the rate of evaporation from the drift wall exceeds the incident percolation flux, because of the capillary pumping feature of the condensation model (SNL 2007, Section 6.3.5.1.4). This is shown by evaporation rates that exceed unity, when normalized by the average percolation incident on the drift (Figures 1 and 2). The drift opening captures as much as two to three times as much flux as that incident on the opening footprint, particularly when drift-wall condensation is strongest (Figure 1). Further, open rockbolt boreholes would access rock that is at a lower temperature, and would therefore tend to decrease humidity at the drift wall during the thermal period, which may lead to liquid/vapor reflux in these open boreholes. However, as discussed in the response to RAI 3.2.2.1.3.6-003, vapor/liquid reflux during the thermal period has little effect on seepage. Thus, while the condensation model does not explicitly account for open rockbolt boreholes, it captures percolation from a distance comparable to or greater than the reach of rock bolt boreholes, when evaporation is active near the center of each drift. The occurrence of drift wall condensation during this period, as predicted by the condensation model for the 1,000-year case, is included in the TSPA and treated as seepage (SNL 2008, Section 6.3.3.2).

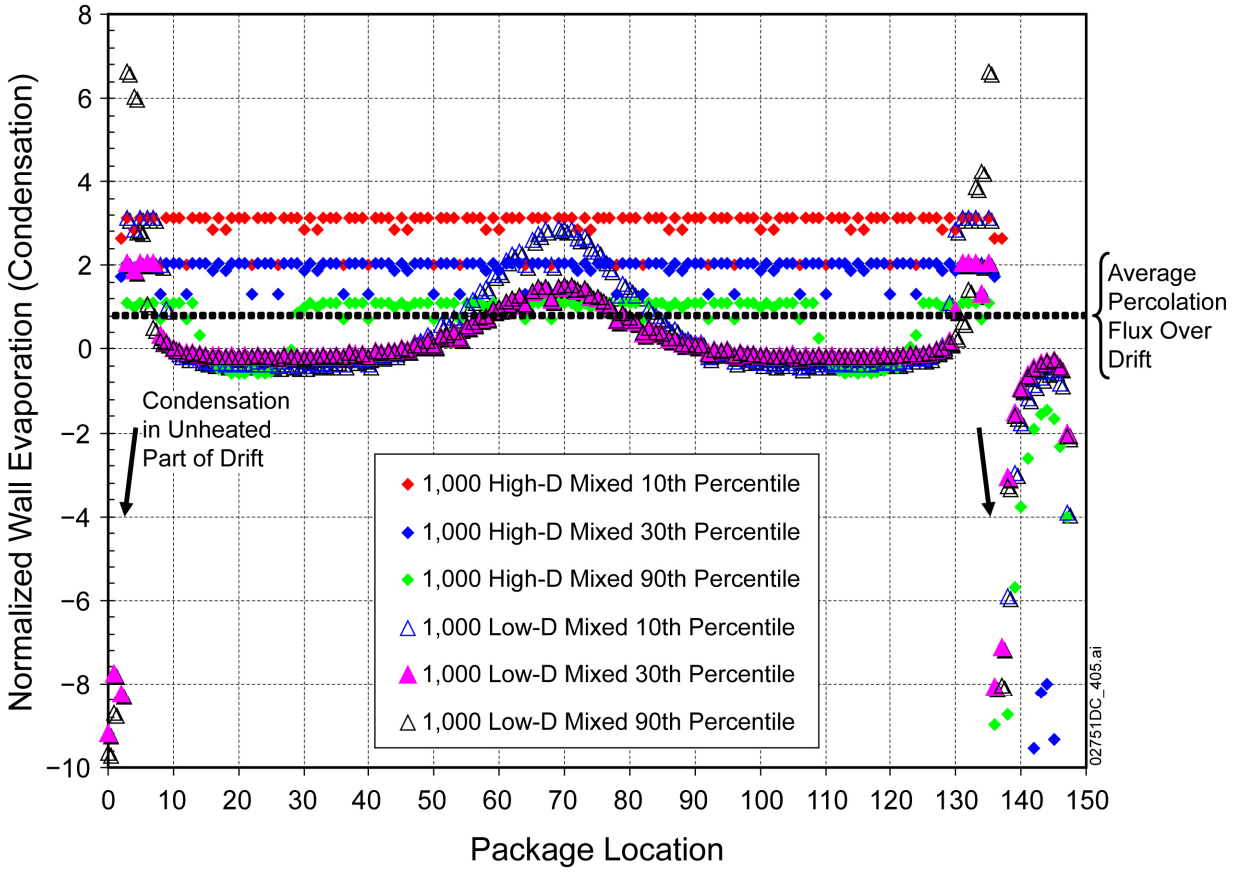

NOTES: "High-D" is the high-dispersion case, and "Low-D" the low dispersion case, from the condensation model (SNL 2007, Section 8.3). Average flux values for Drift #7, based on the 10th, 30th, and 90th percentile percolation fields as noted (glacial-transition period) were used for these calculations.

Figure 1. Profiles of Evaporation (Condensation) Rate with Position in Emplacement Drift #7 from Condensation Model, Including Unheated Ends of Drift, at 1,000 Years after Closure

The effect disappears later in time (Figure 2) when no condensation occurs in the heated part of the drift, and the rate of evaporation is substantially smaller. This occurs even though the condensation model uses a bounding, 100% relative humidity condition at the drift wall to represent availability of moisture for evaporation. This is because the rate of evaporation approaches zero throughout much of the drift (Figure 2). Near the ends of the heated region (where waste packages are emplaced) the evaporation rate remains high because the proximity to the unheated region allows the vapor to migrate away. This means that locally, the partial pressure of water is less than the equilibrium vapor pressure for the local temperature of the drift wall, driving evaporation. This effect does not lead to condensation in the emplacement area. The results described here were obtained even with the lower-bound dispersivity parameter representing low axial mobility of vapor (SAR Section 2.3.5.4.3.2.1).

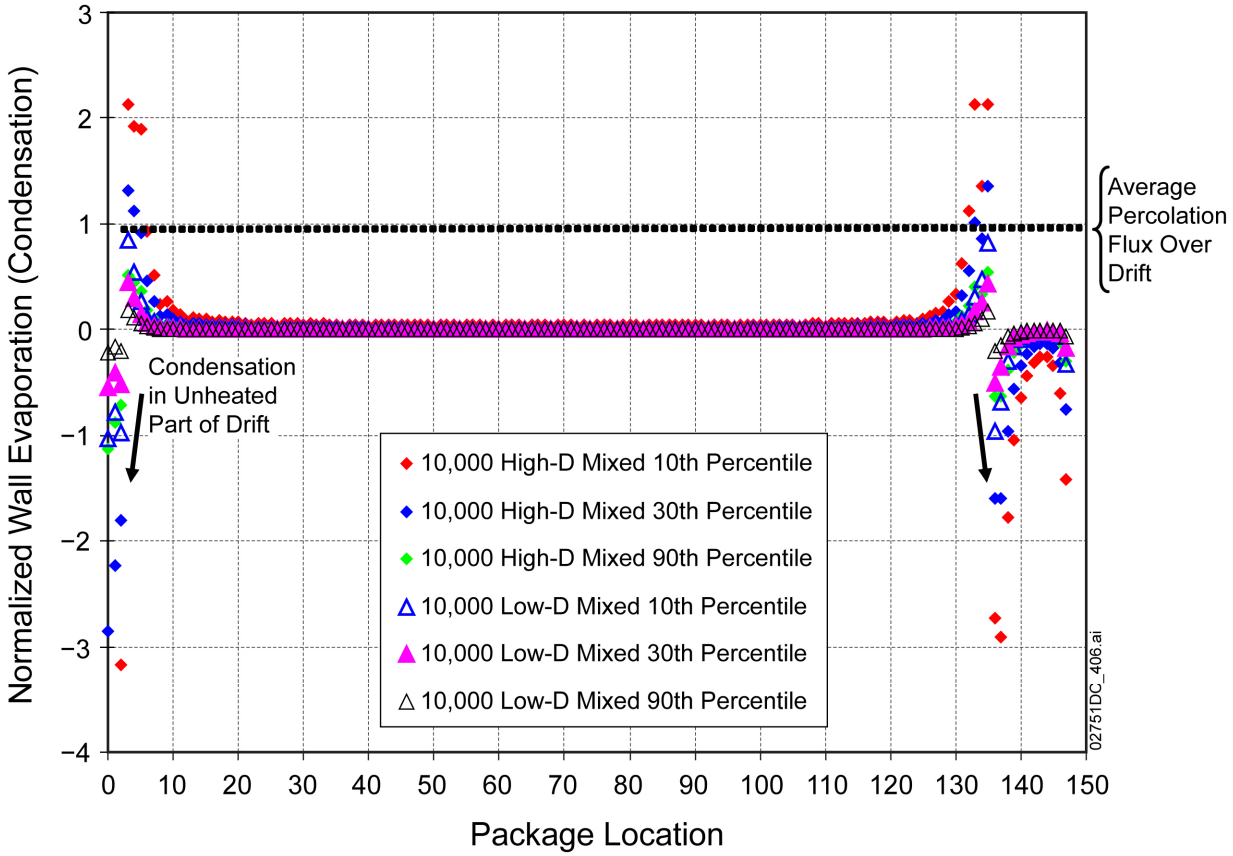

NOTES: "High-D" is the high-dispersion case, and "Low-D" the low dispersion case, from the condensation model (SNL 2007, Section 8.3). Average flux values for Drift #7, based on the 10th, 30th, and 90th percentile percolation fields as noted (glacial transition period) were used for these calculations.

Figure 2. Profiles of Evaporation (Condensation) Rate with Position in Emplacement Drift #7 from Condensation Model, Including Unheated Ends of Drift, at 10,000 Years after Closure

1.5 SUMMARY

In summary, observations in the unventilated portions of the ECRB drift show that evaporation and condensation occur in response to small thermal gradients, and there is resistance to mass transfer between the host rock and the drift opening (SNL 2004, Section 6.10; Salve and Kneafsey 2005). The approach used in the TSPA model, which sums contributions from ambient seepage and drift-wall condensation, each of which is based on conservative simplifications, is consistent with the ECRB observations (SNL 2007, Sections 6.3.7.2 and 6.1[a]).

Large-scale gas movement will be dominated by the underground openings, and gas movement along the openings will generally result in dryout of the heated areas. During early time (up to 2,000 years), evaporation and condensation can occur in the emplacement areas, as represented in the TSPA by the condensation model. During this stage, the rate of evaporation substantially exceeds the average percolation flux incident on the drift, because of the capillary pumping feature of the model. The presence of open rockbolt boreholes during this period, as conduits to cooler rock, would tend to decrease the humidity at the drift wall and thus decrease the

availability of moisture. Later in time, condensation will no longer occur in the emplacement area but will occur only in the unheated area, because of axial vapor transport. The rate of evaporation will decrease substantially, throughout much of the emplacement drift, in later time, in a manner that will be unaffected by increased availability of moisture due to open rockbolt boreholes.

2. COMMITMENTS TO NRC

None.

3. DESCRIPTION OF PROPOSED LA CHANGE

None.

4. REFERENCES

BSC (Bechtel SAIC Company) 2004. *In Situ Field Testing of Processes*. ANL-NBS-HS-000005 REV 03. Las Vegas, Nevada: Bechtel SAIC Company. ACC: DOC.20041109.0001; DOC.20051010.0001; DOC.20060508.0001; DOC.20080724.0006.

Salve, R. and Kneafsey, T.J. 2005. "Vapor-Phase Transport in the Near-Drift Environment at Yucca Mountain." *Water Resources Research*, *41*. Washington, D.C.: American Geophysical Union.

SNL (Sandia National Laboratories) 2007. *In-Drift Natural Convection and Condensation.* MDL-EBS-MD-000001 REV 00 AD 01. Las Vegas, Nevada: Sandia National Laboratories. ACC: DOC.20050330.0001; DOC.20051122.0005; DOC.20070907.0004; LLR.20080324.0007.

SNL 2008. *Total System Performance Assessment Model /Analysis for the License Application.* MDL-WIS-PA-000005 REV 00 AD 01. Las Vegas, Nevada: Sandia National Laboratories. ACC: DOC.20080312.0001; LLR.20080414.0037; LLR.20080507.0002; LLR.20080522.0113; DOC.20080724.0005; DOC.20090106.0001[a].

NOTE: [a]Provided as an enclosure to letter from Williams to Sulima dtd 02/17/2009. "Yucca Mountain – Request for Additional Information Re: License Application (Safety Analysis Report Section 2.1), Safety Evaluation Report Volume 3 – Postclosure Chapters 2.2.1.1 and 2.2.1.3.7 – Submittal of Department of Energy Reference Citations."

RAI Volume 3, Chapter 2.2.1.3.6, First Set, Number 4:

> Explain how averaging seepage rates from individual waste package locations to create representative seepage rates for each percolation subregion impacts EBS radionuclide releases and doses. In addition, provide the technical basis for the assumption that five percolation subregions are sufficient to represent seepage and EBS release variability over the repository footprint. Consideration should be given to both the nominal and seismic ground motion scenarios. This information is needed to verify compliance with 10 CFR 63.114(b).
>
> Basis: One representative waste package with one representative seepage rate is used to calculate EBS release from individual percolation subregions (SNL, 2008a, p. 6.3.7-2). Given the nonlinearity in estimating seepage, it is not clear how averaging to obtain representative values for each percolation subregion may affect EBS release. In addition, justification is not apparent in SAR Section 2.3.5.4.1.4.1 or SNL (2008b, Section 8.3) for why five percolation subregions is sufficiently representative of seepage and EBS radionuclide release variability.

1. RESPONSE

1.1 JUSTIFICATION FOR THE USE OF AVERAGE SEEPAGE RATES IN THE TSPA MODEL

As described in SAR Section 2.3.5.4.1.3.1, the drift seepage submodel uses as input the comprehensive set of output from the multiscale thermal-hydrologic model (MSTHM), which includes the percolation flux at the repository level. The percolation flux at the repository level at each MSTHM subdomain location is used as input to the calculations outlined in *Abstraction of Drift Seepage* (SNL 2007, Section 6.7.1) to obtain: 1) the fraction of waste packages expected to experience seepage, and 2) the seepage rate (m^3/yr per waste package) onto those waste packages that experience seepage. In the MSTHM comprehensive output, the magnitude of percolation flux varies spatially across the repository footprint. This spatial variability is demonstrated in a cumulative distribution function (CDF) of percolation flux values described in Section 1.2.

The spatial variability of seepage within each percolation subregion is summarized by the results presented in Figure 1, which shows CDFs of the quantile position of the average seepage rate within the spatial distribution of seepage. This probabilistic analysis considers an epistemic sample of size 300, as was used in the model. Figure 1 was made by calculating the seepage rate at 100 randomly selected MSTHM subdomain locations in each percolation subregion. For each sample element, the quantile position of the average seepage rate within the spatial distribution of seepage rate (for subdomain locations experiencing seepage rate greater than the threshold value of 0.1 kg/yr per waste package as described in SNL 2008a, Section 6.3.3.1.3) was calculated for each percolation subregion, and the distribution of these quantiles (over the epistemic sample) is shown in Figure 1. For all values of this distribution higher than 0.5, the spatial distribution of seepage is skewed to the right. Figure 1(a) shows that for 10,000 years after closure, the quantile position of the average seepage rate is above 0.5 in all subregions for

most epistemic sample elements; thus, the local seepage rate at most waste package locations in each subregion is less than the average seepage rate. A similar conclusion holds for 1,000,000 years after closure, as displayed in Figure 1(b).

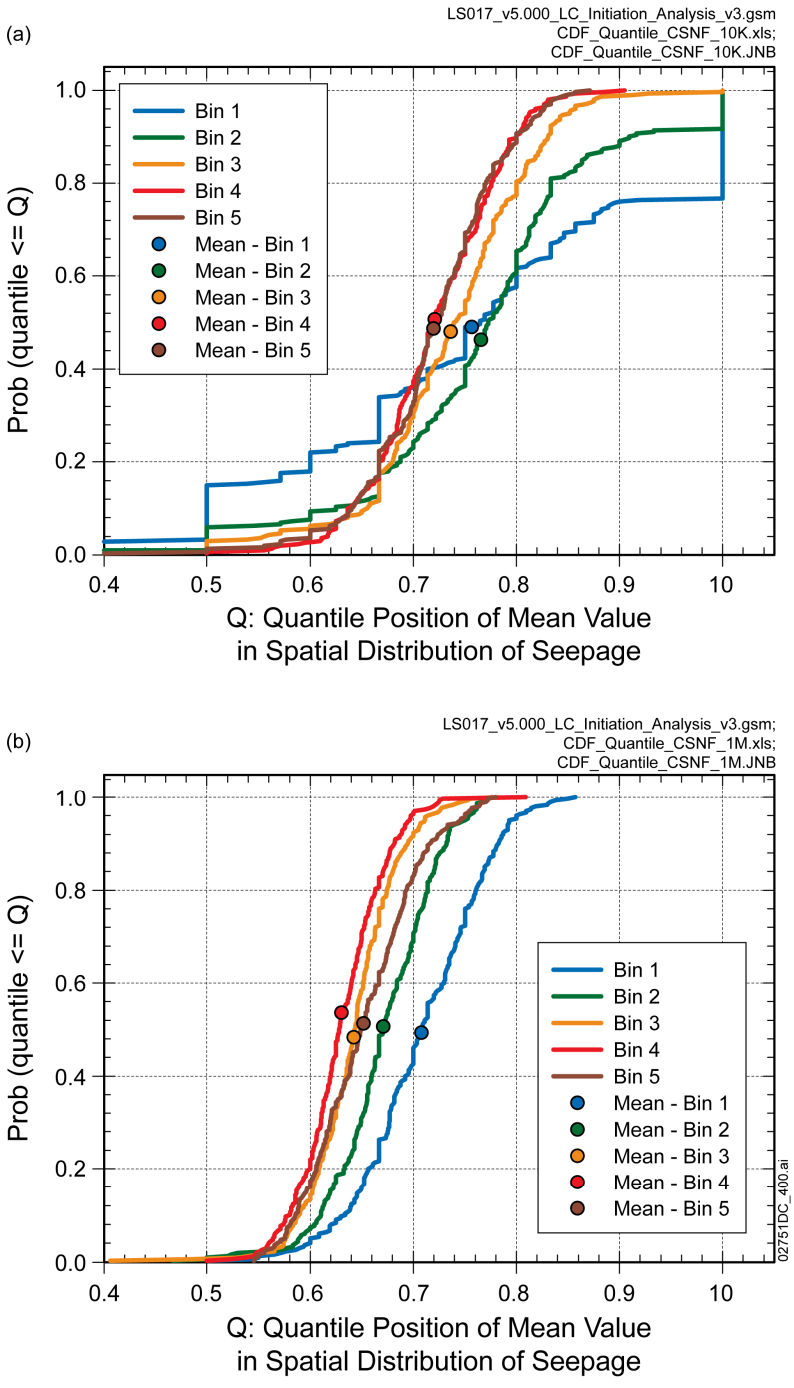

Figure 1 Distribution of Quantile Position of Average Seepage per Percolation Subregion at (a) 10,000 Years and (b) 1,000,000 Years after Closure

To evaluate the effect on radionuclide releases of applying an average seepage rate to all the waste packages experiencing seepage (i.e., flux greater than 0.1 kg/year) in each percolation subregion, the radionuclides considered in the TSPA model can be grouped into two categories. The first category comprises radionuclides without solubility limits (such as ^{129}I and ^{99}Tc), while the second category encompasses those with solubility limits (such as ^{242}Pu). For the highly mobile radionuclides (i.e., nonsorbing and high dissolved concentration limits), the use of spatially averaged seepage rate does not affect their movement. The release rates of these radionuclides are dependent on other factors (as is seen in the stepwise regression analysis in SNL 2008a, Figure K7.3-10) and show very little or no correlation to the amount of seepage.

For solubility-limited radionuclides, the use of average seepage rates is likely to overstate the release rate when the distribution of spatially variable seepage is skewed to the right (i.e., the average seepage rate is largely determined by a few locations with high seepage rates). The application of equal water volumes to all waste packages in seeping locations (i.e., with seepage rate higher than 0.1 kg/year) conservatively estimates the releases of solubility-limited radionuclides, since each waste package in a percolation subregion is assumed to contain the same quantity of radionuclides and the same dissolved concentration limits. In other words, while sufficient radionuclides are available to maintain concentrations at the solubility limits, application of equal water volumes to each waste package in a percolation subregion maximizes the total mass released from the waste packages. In contrast, if spatially variable seepage rates were applied to each waste package, in time, solubility-limited radionuclides within waste packages in high-flow locations may be depleted, resulting in reduced total releases of radionuclides from all waste packages in the subregion.

To confirm the adequacy of using an average seepage rate per waste package for each percolation subregion, cumulative EBS releases are compared between a model with spatially variable seepage rates and spatially variable thermal hydrology (comprehensive case) and a model with a spatially averaged seepage rate and representative thermal hydrology (average case). With the exception of the infiltration and thermal conductivity uncertainties, which are varied in the analysis to evaluate different seepage and thermal hydrology conditions, this analysis is performed for a single realization (i.e., one set of values of epistemic parameters). This differs from the proposed response presented by DOE in the RAI clarification meeting which was to consider the entire epistemic sample set of 300. A single realization was selected instead of a multiple realization analysis because the results show the impact of spatial variability without the additional influence of epistemic uncertainty. Furthermore, the parameter values used in this stylized analysis do not correspond to one of the 300 epistemic sample elements used in the TSPA results presented in SAR Section 2.4. Similar to the analysis of spatial discretization presented in SAR Section 2.4.2.3.2.2.2, this analysis compares cumulative EBS releases for percolation subregion 3 applying the 10th-percentile infiltration map and low thermal conductivity uncertainty; percolation subregion 3 applying the 50th-percentile infiltration map and mean thermal conductivity uncertainty; percolation subregion 3 applying the 90th-percentile infiltration map and high thermal conductivity uncertainty; and percolation subregion 5 applying the 90th-percentile infiltration map and high thermal conductivity uncertainty. For comparisons between spatially variable and average cases, the same infiltration and thermal conductivity uncertainties are applied. Moreover, the comparison has been

performed on three representative radionuclides: ^{242}Pu, ^{129}I and ^{99}Tc. These single realization analyses use the stylized model (rather than the full TSPA model) that is described in the spatial discretization analysis in SAR Section 2.4.2.3.2.2.2.

The comprehensive case considers a single failed waste package at each MSTHM subdomain location of the considered percolation subregion (1,300 and 164 for percolation subregions 3 and 5, respectively). For each subdomain location, spatially discrete values of percolation flux and thermal hydrology are used to determine the rate of seepage at each subdomain location and the subsequent release of radionuclides from an early failed waste package or a waste package under an early failed drip shield. The average case considers the average seepage rate, as calculated in the TSPA model by the Seepage DLL software, and applies the calculated average seepage rate (i.e., average over all waste packages in a seeping environment) and the representative thermal hydrology to a single waste package failure. The resulting EBS release is then multiplied by a comparable number of waste package failures in order to match the number of packages considered in the comprehensive case. For the early failure waste package cases, the comparable number of waste package failures is the number of MSTHM subdomain locations considered in the comprehensive case. In the early failure drip shield case, the comparable number of waste packages is the product of the number of MSTHM subdomain locations considered in the comprehensive case and the seepage fraction calculated by the Seepage DLL in the average case. The seepage fraction adjustment is imposed because a waste package under an early failure drip shield is assumed to fail by localized corrosion and localized corrosion can only occur if seepage contacts the waste package (SNL 2008a, Section 6.4.1.3).

Examination of the drip shield early failure and the waste package early failure modeling cases allows an evaluation of the advective and diffusive components of release of radionuclides from the EBS, respectively. The mechanisms encountered in the seismic ground motion and nominal modeling cases with respect to radionuclides releases have therefore been considered.

Some differences between the comprehensive and average cases are expected. Use of the spatially variable thermal hydrology may result in earlier or later arrival of seepage, thus the onset of transport may vary. In addition, because the comprehensive and average cases are implemented using different software, small differences may be introduced into the model results due to different sampling of the flow focusing factor.

Results displayed in Figures 2 and 3 show a good agreement between the comprehensive and average cases for EBS cumulative releases of ^{99}Tc, ^{129}I, and ^{242}Pu. For highly mobile radionuclides (^{129}I and ^{99}Tc), the EBS releases from the comprehensive case, using the spatially variable thermal hydrology histories from the MSTHM comprehensive data set, generally begin earlier than the cases that used a representative thermal hydrology history. The exception occurs for the cases that use the 90th percentile infiltration and high host-rock thermal conductivity where the releases from the EBS are initiated at about the same times. Since the TSPA model requires the waste package temperature to drop below 100°C before transport from the EBS can be initiated, and since there is some spread between the lower bound and the mean waste package temperatures from the comprehensive thermal hydrology data set (Figure 7.3.4-a(b) through 7.3.4-5(b), SNL 2008a), the EBS releases from the comprehensive cases start earlier

than those that used the representative thermal hydrology data. However, the cumulative mass released is the same for both the comprehensive case and the average seepage case.

The cumulative EBS release for a solubility-limited radionuclide (^{242}Pu) is generally higher in the comprehensive case than in the average case while the cumulative release is relatively small. This higher cumulative release comes from the earlier onset of seepage in some locations in the comprehensive case. However, by about 500,000 years in the drip shield early failure modeling case and 30,000 years in the waste package early failure modeling case, the total cumulative EBS mass release of ^{242}Pu from the average case exceeds the EBS mass release from the comprehensive case. For solubility-limited radionuclides, while sufficient radionuclides are available to maintain concentrations at the solubility limits, application of average water volumes to all waste packages in a percolation subregion increases the total mass released from the waste packages as compared to the total mass released when spatially variable seepage rates are used.

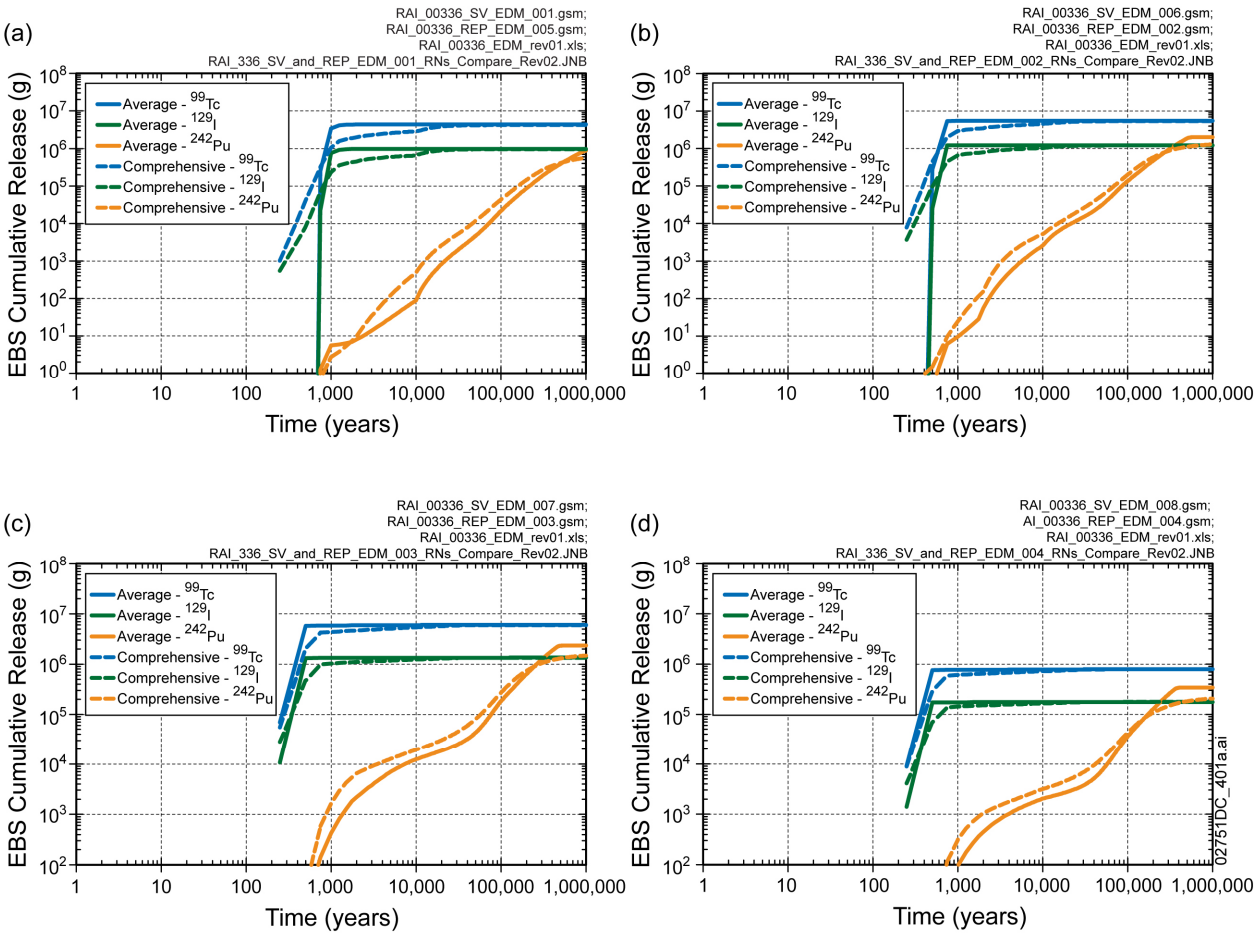

Figure 2 Comparison of Cumulative Releases of ^{99}Tc, ^{129}I, and ^{242}Pu Out of the EBS between Average and Comprehensive Cases for Percolation Subregion 3 and (a) 10th Percentile Infiltration Map, (b) 50th Percentile Infiltration Map, (c) 90th Percentile Infiltration Map, and (d) for Percolation Subregion 5, 90th Percentile Infiltration Map for a Single Realization of the Drip Shield Early Failure Modeling Case

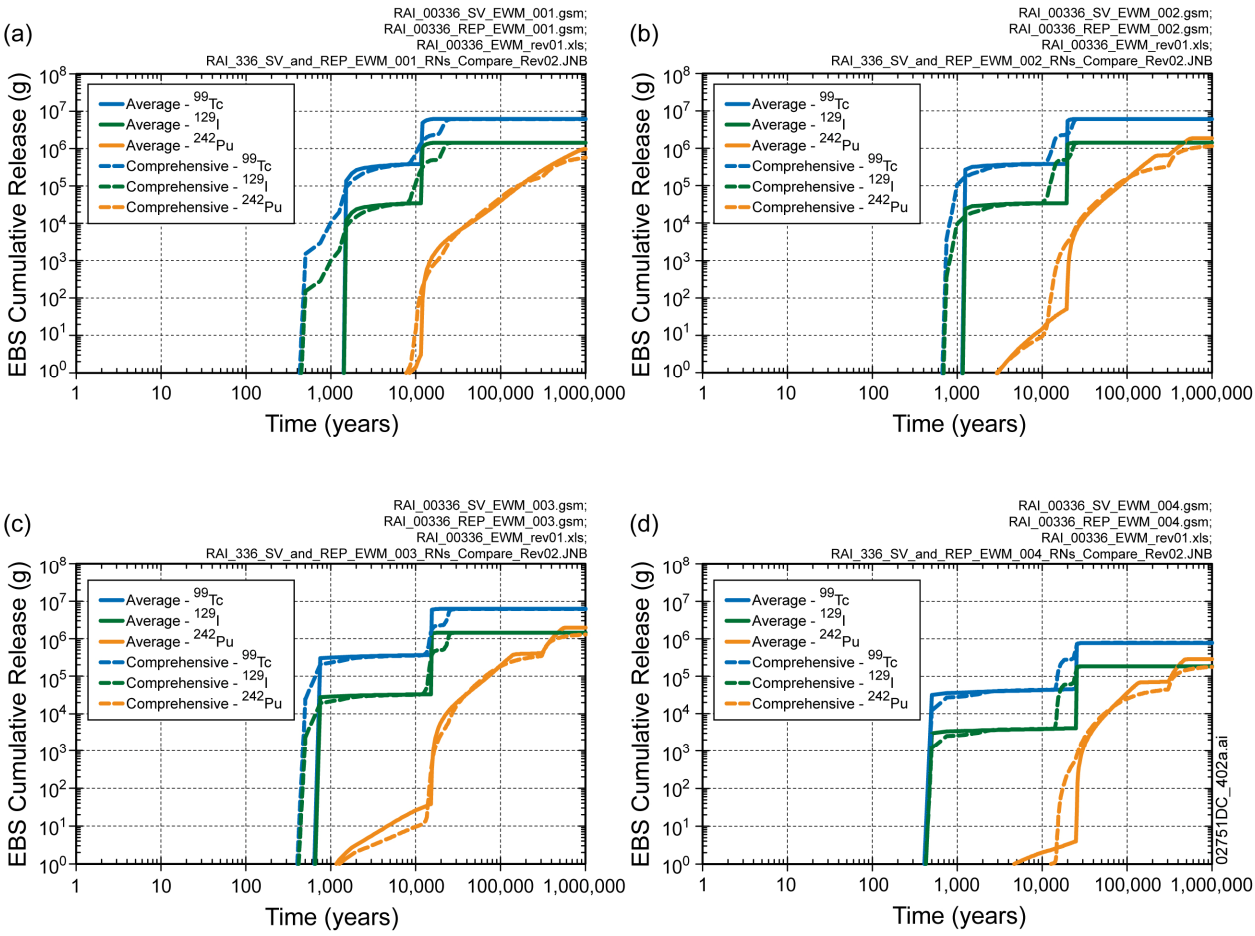

Figure 3 Comparison of Cumulative Releases of ^{99}Tc, ^{129}I, and ^{242}Pu Out of the EBS between Average and Comprehensive Cases for Percolation Subregion 3 and (a) 10th Percentile Infiltration Map, (b) 50th Percentile Infiltration Map, (c) 90th Percentile Infiltration Map, and (d) for Percolation Subregion 5 90th Percentile Infiltration Map for a Single Realization of the Waste Package Early Failure Modeling Case

1.2 JUSTIFICATION OF THE SELECTION OF FIVE PERCOLATION SUBREGIONS

Use of several percolation subregions enables analyses that provide insight into the effect of spatial variability on EBS releases and on annual dose to the reasonably maximally exposed individual (RMEI) (e.g., SNL 2008a, Figures J6.2-13 and J6.3-13). As described in *Total System Performance Assessment Model/Analysis for the License Application* (SNL 2008a, Section 7.3.4.2), the selection of five percolation subregions was a balance between a minimum number of subregions that would adequately capture the variability of the EBS thermal-hydrologic environment across the repository and the increased computational burden associated with additional subregions.

Total System Performance Assessment Model/Analysis for the License Application (SNL 2008a, Section 7.3.4.2.1) gives the rationale for defining the five subregions using the spatial distribution of percolation flux. Percolation flux at the base of the Upper Paintbrush non-welded

vitric (PTn) unit was selected as the primary parameter to discretize the repository into subdomains because: (1) thermal hydrologic response in the emplacement drifts is sensitive to percolation flux; (2) chemical environment for radionuclide mobility is driven by thermal hydrologic conditions; (3) percolation flux is the boundary condition for the drift seepage submodel; and (4) variability in drift seepage is the primary cause of variability in advective radionuclide releases from the EBS. The selection of the five subregions is based on a discretization of the cumulative spatial distribution of percolation flux for the glacial transition climate with the 10th percentile infiltration case. The cumulative distribution function (CDF) described in Table 6-26 of *Particle Tracking Model and Abstraction of Transport Processes* (SNL 2008b) is displayed in Figure 4.

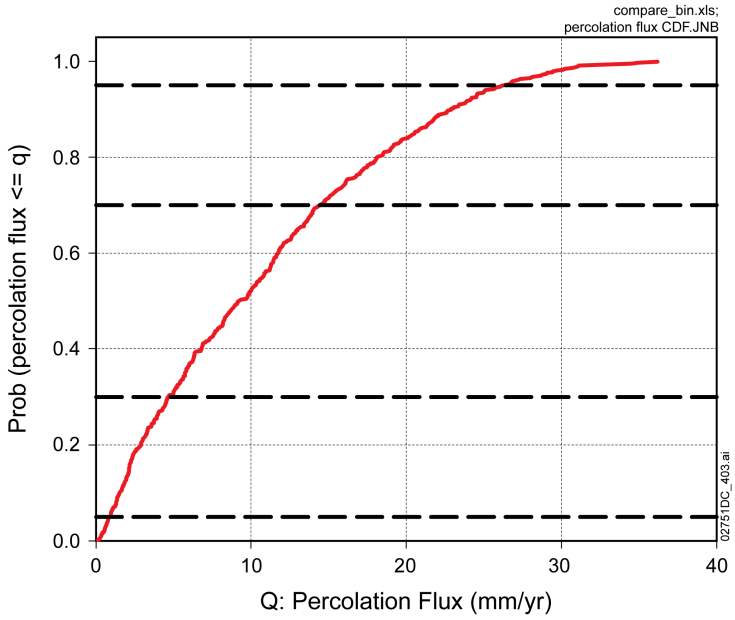

Figure 4 Cumulative Distribution Function of Percolation for Glacial Transition Climate, 10th Percentile Infiltration Scenario (as described in Table 6-26 of SNL 2008b)

The horizontal dashed lines in Figure 4 split the CDF into five bins delimited with the 5th, 30th, 70th, and 95th percentiles. Even though this discretization was essentially based on the glacial-transition, 10th-percentile flow field, analysis for other climates and infiltration maps, show similar results (SNL 2008b, Table 6-26). As noted in *Particle Tracking Model and Abstraction of Transport Processes* (SNL 2008b, Section 6.5.15[a]), if a subregion is identified for a particular subdomain in the glacial-transition, 10th-percentile flow field, it is very often identified as the same subregion for the other flow fields. Based upon this result, it was considered acceptable to use subregions from one flow field to approximate all infiltration scenarios and climate states. Therefore, the 10th-percentile infiltration scenario for the glacial transition climate, shown in Figure 4, was used to define the five percolation subregions for all simulations, including the post-10,000-year climate. There are 163, 817, 1,300, 820, and 164 subdomains (i.e., percolation values and thermal hydrologic data sets) for percolation subregions 1, 2, 3, 4, and 5, respectively.

EBS releases are adequately estimated using average seepage rates in each of the TSPA model percolation subregions as demonstrated in the seepage analysis presented in this response and the validation analyses presented in *Total System Performance Assessment Model /Analysis for the License Application* (SNL 2008a, Section 7.3.4). Consequently, EBS releases would not be substantially different if more refinement in spatial variability were represented by the use of additional percolation subregions. Thus, the use of five percolation subregions is a reasonable discretization for the TSPA model.

1.3 SUMMARY

Averaging seepage rates from individual waste package locations that have seepage rates above the threshold value, and using this average rate for the representative waste package for each percolation subregion, tends to maximize the total mass release from the EBS and is consequently conservative in terms of estimation of the annual dose to the RMEI. Because the use of average seepage rates is adequate to estimate radionuclide releases from each percolation subregion, the use of five subregions to represent spatial variability in percolation and seepage is adequate. Therefore, together, these results demonstrate that the discretization of the repository into five subregions based on the percolation CDF is a sufficient representation in the TSPA model of the spatial variability in percolation and seepage.

2. COMMITMENTS TO NRC

None.

3. DESCRIPTION OF PROPOSED LA CHANGE

None.

4. REFERENCES

SNL (Sandia National Laboratories) 2007. *Abstraction of Drift Seepage.* MDL-NBS-HS-000019 REV 01 AD 01. Las Vegas, Nevada: Sandia National Laboratories. ACC: DOC.20070807.0001; DOC.20080813.0004; DOC.20081118.0049[a].

SNL 2008a. *Total System Performance Assessment Model /Analysis for the License Application.* MDL-WIS-PA-000005 REV 00 AD 01. Las Vegas, Nevada: Sandia National Laboratories. ACC: DOC.20080312.0001; LLR.20080414.0037.

SNL 2008b. *Particle Tracking Model and Abstraction of Transport Processes.* MDL-NBS-HS-000020 REV 02 AD 02. Las Vegas, Nevada: Sandia National Laboratories. ACC: DOC.20080129.0008; DOC.20070920.0003.

NOTE: [a]Provided as an enclosure to letter from Williams to Sulima dtd 02/17/2009. "Yucca Mountain – Request for Additional Information Re: License Application (Safety Analysis Report Section 2.1), Safety Evaluation Report Volume 3 – Postclosure Chapters 2.2.1.1 and 2.2.1.3.7 – Submittal of Department of Energy Reference Citations"

RAI Volume 3, Chapter 2.2.1.3.6, First Set, Number 5:

> Explain how the magnitude and timing of seepage is related to percolation, net infiltration, and precipitation over the repository footprint. To support this explanation, provide a summary table consistent with TSPA-LA results that contains (i) precipitation, (ii) net infiltration (using weights from SNL, 2008), (iii) net infiltration (using GLUE-derived weights), (iv) percolation at repository horizon, and (v) seepage all averaged over the same domain (i.e., repository). The summary values for seepage also should include flux values for percolation subregion and seeping environment in the percolation subregion, and seepage fraction. Consider the nominal and seismic ground motion cases, and the glacial transition and post-10,000-yr climates (percolation and seepage only). This information is needed to verify compliance with 10 CFR 63.114(b).
>
> **Basis:** It is difficult to extract from the SAR a consistent set of values to use in a comparison of flux values on and through the mountain because of the different procedures used to develop summary values in SAR Sections 2.1, 2.3.1, 2.3.2, 2.3.3, and 2.4. The summary values are derived from (i) different modeling domains, (ii) infiltration uncertainty scenarios, (iii) unadjusted and adjusted net infiltration weights (for the latter, GLUE-derived weights), (iv) areas based on the entire repository or percolation region and seeping environment, (v) different rock types, and (vi) calculations from an example exercise.

1. RESPONSE

This response provides a summary of a consistent set of values to use in a comparison of precipitation and the resulting water flux through the mountain and the repository horizon. Table 1 summarizes precipitation, infiltration, percolation, and seepage values averaged over the repository footprint for each infiltration case (10th, 30th, 50th, and 90th percentiles) and climate state. Table 1 also includes mean values calculated using the generalized likelihood uncertainty estimation (GLUE) methodology weighting factors (SAR Section 2.3.2.4.1.2.4.5) for the percolation and seepage rates, as well as for the unsaturated zone flow model upper boundary net infiltration. The values in Table 1 for precipitation and net infiltration are consistent with the percolation flux values and the TSPA model seepage results. The seepage results in Table 1 are averaged over the repository footprint over both seeping and nonseeping waste package locations.

Sections 1.1 through 1.3 outline the relationship between precipitation, net infiltration, percolation, and seepage, including a discussion of the consistency between the values presented in Table 1 and those in the SAR for the different modeling domains and infiltration cases).

- Section 1.1 discusses of the precipitation and net infiltration results from the Infiltration Model presented in SAR Section 2.3.1.

- Section 1.2 discusses of the unsaturated zone flow model upper boundary net infiltration and percolation results at the base of the Upper Paintbrush nonwelded vitric (PTn) unit. These results are presented in SAR Section 2.3.2.

- Section 1.3 presents the average repository percolation and seepage results for the nominal and seismic ground motion cases, including the average seepage fractions, for each percolation subregion and for each climate state. Repository average results for the multiscale thermal-hydrologic model (MSTHM) percolation rates at the base of the PTn unit and TSPA seepage model results are presented in SAR Sections 2.1, 2.3.5, and 2.4.

Table 1. Precipitation, Net Infiltration, Percolation, and Seepage Averaged over the Repository Footprint

Infiltration Percentile[a]	Climate State	Precipitation (mm/yr)[b]	Unsaturated Zone Flow Model Upper Boundary Net Infiltration (mm/yr) [c]	MSTHM Percolation at the Base of PTn[d]		Seepage (m^3/yr per waste package)[e]	
			2007	mm/yr	m^3/yr per Waste Package	Nominal	Seismic
10th *p* = 0.6191	Present-Day	150.9	4.0	4.09	0.115	0.001	0.001
	Monsoon	216.2	7.7	7.82	0.219	0.005	0.006
	Glacial-Transition	284.4	11.8	12.14	0.341	0.016	0.020
	Post-10,000-year	—	—	21.50	0.603	0.042	0.241
30th *p* = 0.1568	Present-Day	168.2	10.1	10.23	0.287	0.008	0.008
	Monsoon	157.8	15.9	16.11	0.452	0.026	0.027
	Glacial-Transition	277.3	25.8	26.28	0.737	0.070	0.082
	Post-10,000-year	—	—	40.37	1.132	0.148	0.612
50th *p* = 0.1645	Present-Day	198.2	14.4	14.63	0.410	0.015	0.016
	Monsoon	252.1	19.3	19.53	0.548	0.037	0.037
	Glacial-Transition	233.6	35.3	36.17	1.015	0.109	0.123
	Post-10,000-year	—	—	51.78	1.452	0.195	0.804
90th *p* = 0.0596	Present-Day	222.7	33.7	34.08	0.956	0.072	0.074
	Monsoon	324.7	91.4	92.4	2.592	0.438	0.446
	Glacial-Transition	300.0	68.6	69.69	1.955	0.278	0.312
	Post-10,000-year	—	—	61.60	1.728	0.226	0.960
Unweighted Mean Results[f]	Present-Day	181.8	17.25	—	—	—	—
	Monsoon	288.1	37.93	—	—	—	—
	Glacial-Transition	296.7	38.69	—	—	—	—
	Post-10,000-year	—	—	—	—	—	—
Weighted Mean Results	Present-Day	—	8.44	8.57	0.24	0.01	0.01
	Monsoon	—	15.88	16.09	0.45	0.04	0.04
	Glacial-Transition	—	21.25	21.74	0.61	0.06	0.06
	Post-10,000-year	—	—	31.83	0.89	0.10	0.43

NOTE: Precipitation over repository footprint equals precipitation over infiltration domain multiplied by 1.047.

Source: [a]GLUE probability weighting factors for the 10th, 30th, 50th, and 90th percentile infiltration cases: SAR Section 2.3.2.4.1.2.4.5.5. [b] SAR Tables 2.3.1-2, 2.3.1-3, and 2.3.1-4. [c]Unsaturated zone flow model results for the average upper boundary net infiltration over the 2007 repository footprint. [d] Data extracted from the MSTHM input to the TSPA model, SAR Section 2.3.5.4.1.3.2.The percolation flux (m^3/yr) was calculated using the cross-sectional area used in the calculation of seepage in the TSPA model (5.5m drift diameter x 5.1m waste package length). [e]The seepage values were extracted from the nominal and seismic ground motion modeling cases for 1,000,000 years.
[f]SAR Tables 2.3.1-2, 2.3.1-3, and 2.3.1-4. Unweighted Mean net infiltration is based on unweighted probability of the infiltration percentiles (0.2, 0.2, 0.3, 0.3) documented in SAR Section 2.3.2.4.1.2.4.5.1.

1.1 PRECIPITATION AND NET INFILTRATION SUMMARY RESULTS

Table 2 presents precipitation and net infiltration results for each pre-10,000-year climate state. These results are spatially averaged over the infiltration model domain and over the vertical projection of the 2002 repository footprint for each of the four infiltration percentile maps used in the TSPA model. The unweighted mean precipitation and net infiltration values in Table 2 are based on all 40 realizations of the infiltration model (SAR Section 2.3.1.3.3.1.2, p. 2.3.1-67). In addition, Table 2 presents the weighted mean net infiltration using GLUE methodology weighting factors (SAR Section 2.3.2.4.1.2.4.5). As discussed in SAR Section 2.3.2.4.1.2.4.5.1, the 10th, 30th, 50th, and 90th percentile infiltration maps from the infiltration model have prior weights of 0.2, 0.2, 0.3, and 0.3, respectively. The resulting weights after calibration, using the GLUE methodology, are 0.6191, 0.1568, 0.1645, and 0.0596, respectively. SAR Section 2.1 (p. 2.1-18) includes a discussion of the estimated average net infiltration ranges as a percentage of the precipitation, consistent with the data presented in SAR Section 2.3.1 and Table 2, averaged over the infiltration model domain. A significant reduction of precipitation is reflected in the ratio of net infiltration to precipitation included in Table 2 and also in the ratio of percolation to precipitation shown in Table 11.

It should be noted that the precipitation values in Tables 1 and 2 correspond to specific realizations of the infiltration model (Mass Accounting System for Soil Infiltration and Flow – MASSIF) selected as representative of the 10th, 30th, 50th, and 90th percentile net infiltration cases; they do not represent the respective percentiles of precipitation. The precipitation value presented for the realization selected for the 10th percentile net infiltration map for the monsoon climate state is larger than the precipitation value for the 30th percentile net infiltration map. The same is observed when comparing the precipitation presented for 10th, 30th, and 50th percentile net infiltration maps selected for the glacial-transition climate. This is due to differences in the sampled values uncertain parameters used in each of the 40 infiltration model realizations. Some of the parameters that were varied included stochastic parameters describing precipitation. It is also noteworthy that the maximum value of average annual precipitation for the monsoon climate is larger than that for the glacial-transition climate, because more extreme precipitation events are predicted for the monsoon than for glacial-transition climate.

The infiltration model provides four net infiltration maps to serve as the upper boundary condition flux for the site-scale unsaturated zone flow model, (SAR Section 2.3.2.4.1.2.4.5) for each of the three climate states in the pre-10,000-year period: present-day, monsoon, and glacial-transition. SAR Figure 2.3.1-2 portrays the information transfer within the TSPA model over the three modeled climate states. These maps represent the 10th, 30th, 50th, and 90th percentile infiltration conditions. Uncertainty in infiltration is incorporated through the selection of the net infiltration maps corresponding to one of the four infiltration conditions in each TSPA realization. The mean values for each infiltration percentile map presented in Table 2 represent the mean over the infiltration percentile for each of the three 10,000-year climate states used in the TSPA model. SAR Section 2.4.1 describes the implementation and integration of the infiltration model outputs into the TSPA model.

Table 2. Average Precipitation and Net Infiltration Rates over the pre-10,000-year Period

Infiltration Map Percentile[a]	Climate State	Infiltration Model Domain[b]			2002 Repository Footprint[b,c]		
		Precipitation (mm/yr)	Net Infiltration (mm/yr)	Ratio of Net Infiltration to Precipitation (%)	Precipitation (mm/yr)	Net Infiltration (mm/yr)	Ratio of Net Infiltration to Precipitation (%)
10th *p* = 0.6191	Present-Day	144.1	3.9	2.71	150.9	3.9	2.58
	Monsoon	206.5	6.3	3.05	216.2	6.2	2.87
	Glacial-Transition	271.7	13.2	4.86	284.4	8.5	2.99
30th *p* = 0.1568	Present-Day	160.6	7.3	4.55	168.2	6.5	3.86
	Monsoon	150.7	14.4	9.56	157.8	18.9	11.98
	Glacial-Transition	264.8	22.8	8.61	277.3	25.6	9.23
50th *p* = 0.1645	Present-Day	189.3	13	6.87	198.2	10.9	5.76
	Monsoon	240.8	22.9	9.51	252.1	28.8	11.42
	Glacial-Transition	223.1	28.6	12.82	233.6	40.5	17.34
90th *p* = 0.0596	Present-Day	212.7	26.7	12.55	222.7	34.4	16.17
	Monsoon	310.2	52.6	16.96	324.7	74.5	22.94
	Glacial-Transition	286.6	47	16.40	300	68.8	22.93
Unweighted Mean Results[d]							
	Present-Day	173.6	14.30	8.24	181.8	17.6	9.68
	Monsoon	275.2	25.50	9.27	288.1	32.9	11.42
	Glacial-Transition	283.4	30.00	10.59	296.7	38.7	13.04
GLUE-Weighted Mean Results[e]							
	Present-Day	—	7.29	—	—	7.28	—
	Monsoon	—	13.06	—	—	15.98	—
	Glacial-Transition	—	19.25	—	—	20.04	—

NOTE: Precipitation over repository footprint equals precipitation over infiltration domain multiplied by 1.047 (ratio that accounts for the mean elevation difference between the repository footprint cells and the entire infiltration modeling domain cells).

Source: [a]GLUE probability weighting factors for the 10th, 30th, 50th, and 90th percentile infiltration cases: SAR Section 2.3.2.4.1.2.4.5. [b] SAR Tables 2.3.1-2, 2.3.1-3, and 2.3.1-4.
[c]Repository Footprint Results extracted from the Infiltration Model results documented in SAR 2.3.1.3.3.1.2.
[d]SAR Tables 2.3.1-2, 2.3.1-3, and 2.3.1-4. Unweighted Mean values are averaged over all 40 realizations of the infiltration model .
[e]GLUE-weighted results calculated using the probability weighting factors for the 10th, 30th, 50th, and 90th percentile infiltration cases.

1.2 UNSATURATED ZONE FLOW MODEL UPPER BOUNDARY NET INFILTRATION AND PERCOLATION SUMMARY RESULTS

For the pre-10,000-year period, the site-scale unsaturated zone flow model uses the 10th, 30th, 50th, and 90th percentile net infiltration maps for the present and two future climate states as input to produce steady-state percolation flow fields and distribution of percolation fluxes for use in the TSPA (SAR Section 2.3.2.4.1.2.4.2). For the post-10,000-year period, the site-scale unsaturated zone flow model provides four additional steady-state percolation flow fields for which the spatially averaged percolation at the repository horizon represents the distribution of deep percolation rates specified in 10 CFR 63.342(c)(2) (SAR Section 2.3.2.4.1.2.4.2). As described in SAR Section 2.3.2.4.1.2.4.2, a set of maps for the net infiltration boundary condition is developed to spatially distribute water flux while matching the specified average percolation rates. This is done using the infiltration maps for the pre-10,000-year period and scaling the net infiltration rates such that the average net infiltration rate over the 2007 repository footprint matches the target average percolation flux rates in the repository footprint selected to represent the log-uniform distribution. The post-10,000 year percolation results are based upon the proposed log-uniform (13-64 mm/yr) distribution, not the truncated log-normal (10-100 mm/yr) as revised in the final rule. The results presented in this response are consistent with the SAR and TSPA model results and therefore do not include the change in the distribution for the deep percolation rates.

SAR Table 2.3.2-27 summarizes the net infiltration for all climate states averaged over the unsaturated zone flow model domain; these results are included in Table 3 for comparison with the repository footprint average net infiltration results. Table 3 presents results for both the older 2002 repository footprint used to calculate the average infiltration model results presented in Table 2, and the current repository footprint, used in 2007 for the License Application are presented in Table 3 for comparison with SAR Section 2.3.1 and to provide a consistent set of values over the same spatial domain. The infiltration results presented in Table 2 are calculated using a vertical projection of a 2002 version of the repository footprint, consistent with SAR Tables 2.3.1-2, 2.3.1-3, and 2.3.1-4, rather than the 2007 repository footprint used in the TSPA model. Since the 2002 repository footprint was used only for qualitative discussions of the infiltration model results and the difference between the average net infiltrations over the footprints is small (as presented in Table 3); the summary infiltration model results were not updated for the 2007 repository footprint in the supporting documentation or in SAR Section 2.3.1. The downstream models were unaffected since the net infiltration boundary flux was extracted from the net infiltration maps for the entire unsaturated zone model domain.

The unsaturated zone flow model provides percolation flux at the base of the PTn unit to the MSTHM, as well as providing the three-dimensional flow fields used by the unsaturated zone transport model component of the TSPA model (SAR Sections 2.3.5; SNL 2008, Section 6.3.2). The percolation rates over the repository footprint are spatially interpolated from the unsaturated zone model domain to the 3,624 MSTHM subdomain locations (SAR Sections 2.3.3.2.3.5 and 2.3.2). Table 3 provides a summary of the percolation rates over the repository footprint extracted from the unsaturated zone flow model and from the MSTHM. There are only minor differences in these average values as a result of the spatial interpolation between the unsaturated zone flow model domain and the MSTHM subdomain locations.

SAR Figure 2.3.2-1 shows the information flow diagram for development of the site-scale unsaturated zone flow model, and SAR Figure 2.3.2-2 shows the information transfer among the principal model components for the TSPA nominal modeling case. The unsaturated zone flow model provides the unsaturated zone flow fields used in the TSPA model unsaturated zone transport calculations. In addition, for each infiltration boundary condition and climate state, the site-scale unsaturated zone flow model provides the following outputs to the MSTHM (SAR Section 2.4.2.3.2.1): (1) the percolation flux at the base of the PTn unit above each subdomain location, (2) the three-dimensional numerical grid, and (3) associated unsaturated zone hydrologic properties. The percolation values used in the MSTHM are spatially interpolated from the 16 unsaturated zone flow fields and are passed from the MSTHM to the TSPA model to predict seepage into emplacement drifts under ambient and thermally perturbed conditions (SNL 2008, Section 6.3.3.1.2).

Table 3. Unsaturated Zone Flow Model Results

Unsaturated Zone Flow Model Domain			Repository Footprint			
Infiltration Map Percentile[a]	Climate State	Net Infiltration (mm/yr)[b]	Unsaturated Zone Flow Model Upper Boundary Net Infiltration (mm/yr)		Unsaturated Zone Flow Model Percolation at Base of PTn (mm/yr)[e]	MSTHM Percolation at Base of PTn (mm/yr)[f]
			2002[c]	2007[d]		
10th *p* = 0.6191	Present-Day	3.03	3.9	4.0	4.1	4.09
	Monsoon	6.74	6.2	7.7	7.8	7.82
	Glacial-Transition	11.03	8.5	11.8	12.2	12.14
	Post-10,000-year	16.89	—	—	21.29	21.50
30th *p* = 0.1568	Present-Day	7.96	6.5	10.1	10.2	10.23
	Monsoon	12.89	18.9	15.9	16.1	16.11
	Glacial-Transition	20.45	25.6	25.8	26.3	26.28
	Post-10,000-year	28.99	—	—	39.52	40.37
50th *p* = 0.1645	Present-Day	12.28	10.9	14.4	14.6	14.63
	Monsoon	15.37	28.8	19.3	19.5	19.53
	Glacial-Transition	25.99	40.5	35.3	36.2	36.17
	Post-10,000-year	34.67	—	—	51.05	51.78
90th *p* = 0.0596	Present-Day	26.78	34.4	33.7	34.1	34.08
	Monsoon	73.26	74.5	91.4	92.4	92.40
	Glacial-Transition	46.68	68.8	68.6	69.7	69.69
	Post-10,000-year	48.84	—	—	61.03	61.60
Mean Results	Present-Day	6.74	7.28	8.44	8.57	8.57
	Monsoon	13.09	15.98	15.88	16.07	16.09
	Glacial-Transition	17.09	20.04	21.25	21.79	21.74
	Post-10,000-year	23.62	—	—	31.41	31.83

NOTE: Mean results for the pre-10,000 year climates are GLUE weighted. Post-10,000 year Mean Results represent the sample mean of the percolation resulting from approximating the distribution of deep percolation by four discrete values. The GLUE weighting factors are used to select these four discrete values.

Source: [a]GLUE probability weighting factors for the 10th, 30th, 50th, and 90th percentile infiltration realizations SAR Section 2.3.2.4.1.2.4.5.5. [b]Average net infiltration over the unsaturated zone model domain, SAR Tables 2.3.2-27.[c]Infiltration model results over the repository footprint from Table 2 using a 2002 repository footprint, SAR Section 2.3.1.3.3.2. [d]Unsaturated Zone Flow Model Results for the Upper Boundary Net Infiltration over the 2007 Repository Footprint. [e]Unsaturated zone flow model results for the average percolation over the repository footprint and Table H-2 of SNL 2007. Post-10,000-year values from SAR Table 2.3.2-15. [f] Data extracted from the MSTHM input to the TSPA model, SAR Section 2.3.5.4.1.3.

1.3 SEEPAGE SUMMARY RESULTS USED IN THE TSPA MODEL CALCULATIONS

As shown in SAR Figure 2.3.3-1, information needed for the implementation of the drift seepage submodel in the TSPA model is provided by two TSPA model components: (1) the Engineered Barrier System (EBS) thermal-hydrologic environment submodel (SNL 2008, Section 6.3.2), and (2) the seismic damage submodel (SNL 2008, Section 6.6). The EBS thermal-hydrologic environment submodel contains the MSTHM provided percolation flux values interpolated at various locations throughout the repository (SAR Section 2.3.3.2.3.5) from the flux distributions for current and future climate states calculated by the site-scale unsaturated zone flow model (SAR Section 2.3.2). The EBS thermal-hydrologic environment submodel also provides the evolution of drift-wall temperature at each repository location, which is required to evaluate whether thermal seepage is limited by a vaporization barrier (SAR Section 2.3.3.3.4). The TSPA submodel for the seismic damage abstraction provides cumulative rockfall volumes in response to single or multiple seismic events, which describe the degree of drift degradation and its impact on seepage (SAR Section 2.3.3.2.4.2.2).

Table 4 contains average percolation fluxes used in the TSPA model to calculate the drift seepage for each infiltration case at each climate state, including an average percolation rate over the repository footprint as well as for each repository percolation subregion. The flux quantile values for each percolation subregion are also provided in the table. The weighted repository average percolation rate is shown on SAR Figure 2.1-5 and included in Table 4.

The TSPA drift seepage submodel calculates the seepage rate (average seepage per waste package in a seeping environment) as a function of time for each repository subregion for the nominal and seismic ground motion modeling cases (Section 6.3.3, SNL 2008). The probabilistic seepage calculation in the TSPA is a function of the local percolation and the ambient and thermal components of the drift seepage abstraction, as described in SAR Sections 2.3.3.2.4 and 2.3.3.3.4. Tables 5 through 10 contain TSPA model seepage results extracted at 500-, 750-, 10,000-, and 1,000,000-year time steps to illustrate the temporal variation in seepage between the present-day, monsoon, glacial-transition, and post-10,000-year climate states, respectively. Seepage results for the nominal modeling case represents the average seepage rate over the epistemic uncertainties (conditional on one infiltration map) in the absence of disruptive events (e.g., igneous or seismic events). In addition, to demonstrate the impact of drift degradation, seepage results from the seismic ground motion modeling case are presented; these results are averaged over the epistemic uncertainties (conditional on one infiltration map) as well as the aleatory uncertainty in seismic events. Table 5 contains the TSPA nominal scenario modeling case seepage results in terms of flux per waste package for each infiltration case at each climate state, including an average over the repository footprint as well as an average for each repository subregion, including both seeping and non-seeping environments. The average seepage fractions (the fraction of waste packages in a percolation subregion experiencing seepage) are also presented in Table 5. Tables 6 and 7 provide the average seepage per waste package in a seeping environment for commercial spent nuclear fuel (SNF) and codisposal waste packages.

Table 8 contains the TSPA seismic ground motion modeling case seepage results. These seepage rates account for seismic-induced drift collapse, which increases the seepage rates over time until the drift is fully degraded, as demonstrated in SAR Figure 2.1-5. It should be noted in the seismic ground motion case results that the selection of seepage data extracted at 500-, 750-, 10,000-, and 1,000,000-year time steps to demonstrate the temporal variation in seepage for each climate state, maximizes the effects of drift degradation on seepage for the glacial-transition and post-10,000-year climates by extracting the seepage values at the end of these climate states; at the 10,000- and 1,000,000-year time steps respectively. Tables 9 and 10 contain the commercial SNF and codisposal seismic seepage rate per waste package in a seeping environment. The seepage fractions are presented as calculated for the post-10,000-year climate, as used in the 1,000,000 year TSPA model. Since the seepage fractions are calculated at 1,000,000 years, the high fractions in the seismic ground motion modeling case reflect the increase in seepage due to seismic induced drift degradation. These seepage fractions are consistent with SAR Tables 2.1-6 to 2.1-9, which include the TSPA nominal and seismic ground motion modeling case seepage fractions for the glacial-transition climate and the post-10,000-year period. SAR Figure 2.3.3-47 presents the mean seepage rates as a function of time for the four infiltration scenarios consistent with the repository average results presented in Table 5. SAR Figure 2.1-5 plots the mean seepage over the repository, consistent with the weighted mean data presented in Tables 5 and 8 for the nominal and seismic ground motion modeling cases.

The tabulated TSPA model results show that higher infiltration scenarios result in more seepage in both the nominal and seismic ground motion modeling cases, as described in SAR Section 2.3.3.4.2 and shown in SAR Figures 2.3.3-47 to 2.3.3-49. As presented in Table 11, over all waste packages, the repository average amount of seeping water weighted by the relative probability for each infiltration case is approximately 0.01, 0.04, and 0.06 m^3/yr per waste package for the present-day, monsoon, and glacial-transition climate states, respectively. The corresponding ratio of seepage to percolation over the pre-10,000-year time period included on Table 11 is between approximately 4% and 10% for the repository average TSPA seepage over all infiltration maps. These results confirm that over the pre-10,000-year time period, about 90% to 96% of the percolation flux would be diverted around an intact drift, on average. For the post-10,000-year period over all waste packages, the repository average amount of seeping water weighted by the relative probability for each infiltration case is approximately 0.1 and 0.43 m^3/yr per waste package for the nominal and seismic ground motion modeling cases, respectively, at 1,000,000 years. The corresponding ratio of seepage to percolation over the post-10,000 year time period are approximately 11% and 49% for the nominal and seismic ground motion modeling cases respectively. On average, about 89% of the percolation flux would be diverted around a drift in the nominal modeling cases, whereas only 51% of the percolation flux would be diverted around a fully degraded drift at 1,000,000 years in the seismic ground motion modeling case. Drift degradation also results in a significant increase in the fraction of waste packages that encounter seeping conditions from 40% in the nominal case to 69% in the seismic ground motion modeling case based on the comparison of the seepage fraction shown in Tables 5 and 8 (SAR Section 2.4.2.2.1.2.2.1; SNL 2008, Tables 8.3-3[a] and 8.3-5[a]).

Table 4. Average Percolation Flux Used in the TSPA Calculations

Infiltration Map Percentile[a]	Climate State	MSTHM Percolation at Base of PTn Subregion Rates[b,c] (mm/yr)					MSTHM Repository Average Percolation at Base of PTn	
		1 (0.05)	2 (0.25)	3 (0.4)	4 (0.25)	5 (0.05)	(mm/yr)	(m^3/yr per waste package)
10th p = 0.6191	Present-Day	0.49	2.33	4.32	5.68	6.71	4.09	0.115
	Monsoon	1.23	5.38	8.31	10.00	11.72	7.82	0.219
	Glacial-Transition	0.68	3.72	11.06	20.93	30.46	12.14	0.341
	Post-10,000-year	2.56	15.06	23.32	26.94	30.90	21.50	0.603
30th p = 0.1568	Present-Day	1.58	6.50	10.84	13.59	15.81	10.23	0.287
	Monsoon	2.34	10.68	17.03	21.24	24.06	16.11	0.452
	Glacial-Transition	2.51	13.53	27.15	38.29	46.90	26.28	0.737
	Post-10,000-year	2.55	17.46	41.50	61.55	77.82	40.37	1.132
50th p = 0.1645	Present-Day	2.22	9.72	15.55	18.87	22.79	14.63	0.410
	Monsoon	2.29	11.22	20.38	26.62	36.14	19.53	0.548
	Glacial-Transition	2.45	15.71	37.17	55.09	69.65	36.17	1.015
	Post-10,000-year	4.29	29.85	55.67	70.47	84.28	51.78	1.452
90th p = 0.0596	Present-Day	4.942	24.08	36.87	42.53	48.59	34.08	0.956
	Monsoon	12.52	65.45	99.91	115.5	131.51	92.40	2.592
	Glacial-Transition	5.84	40.30	74.93	94.78	113.20	69.69	1.955
	Post-10,000-year	8.81	43.74	66.56	76.91	87.51	61.60	1.728
Mean Results	Present-Day	1.21	5.51	9.13	11.28	13.28	8.57	0.24
	Monsoon	2.25	10.76	17.12	20.79	24.81	16.09	0.45
	Glacial-Transition	1.57	9.41	21.69	33.67	44.41	21.74	0.61
	Post-10,000-year	3.22	19.58	34.07	42.51	50.41	31.83	0.89

NOTE: The percolation flux (m^3/yr) was calculated using the cross-sectional area used in the calculation of seepage in the TSPA model (5.5-m drift diameter × 5.1-m waste package length). Mean results for the pre-10,000 year climates are GLUE weighted. Post-10,000 year Mean Results represent the sample mean of the percolation resulting from approximating the distribution of deep percolation by four discrete values. The GLUE weighting factors are used to select these four discrete values.

Source: [a]GLUE probability weighting factors for the 10th, 30th, 50th, and 90th percentile infiltration realizations: SAR Section 2.3.2.4.1.2.4.5.5.
[b]Data extracted from the MSTHM input to the TSPA model, SAR Section 2.3.5.4.1.3.2.
[c]Percolation subregions and quantile ranges SAR Section 2.4.2.3.2.1.2.

Table 5. Nominal Modeling Case Average Seepage Rate and Fraction Summary

TSPA Average Seepage for the Nominal Modeling Case 1,000,000 Years – Repository Footprint							
Infiltration Map Percentile[a]	**Climate State**	**Average Flux over the Subregion[b,c] (m^3/yr per waste package)**					**Repository Average (m^3/yr per waste package)**
		1 (0.05)	**2 (0.25)**	**3 (0.4)**	**4 (0.25)**	**5 (0.05)**	
10th p = 0.6191	Present-Day	2.66×10^{-5}	4.81×10^{-4}	9.24×10^{-4}	1.20×10^{-3}	2.33×10^{-3}	0.001
	Monsoon	3.20×10^{-4}	3.53×10^{-3}	5.82×10^{-3}	6.40×10^{-3}	1.07×10^{-2}	0.005
	Glacial-Transition	7.97×10^{-5}	1.50×10^{-3}	1.14×10^{-2}	3.15×10^{-2}	6.92×10^{-2}	0.016
	Post-10,000-year	2.04×10^{-3}	2.79×10^{-2}	4.76×10^{-2}	4.97×10^{-2}	7.23×10^{-2}	0.042
	Seepage Fraction	*0.099*	*0.295*	*0.370*	*0.359*	*0.415*	*0.337*
30th p = 0.1568	Present-Day	4.24×10^{-4}	4.90×10^{-3}	8.16×10^{-3}	1.02×10^{-2}	1.68×10^{-2}	0.008
	Monsoon	1.52×10^{-3}	1.63×10^{-2}	2.81×10^{-2}	3.38×10^{-2}	4.75×10^{-2}	0.026
	Glacial-Transition	1.71×10^{-3}	2.51×10^{-2}	7.10×10^{-2}	1.09×10^{-1}	1.68×10^{-1}	0.070
	Post-10,000-year	1.57×10^{-3}	3.91×10^{-2}	1.46×10^{-1}	2.42×10^{-1}	3.84×10^{-1}	0.148
	Seepage Fraction	*0.135*	*0.356*	*0.517*	*0.553*	*0.622*	*0.472*
50th p = 0.1645	Present-Day	8.27×10^{-4}	1.05×10^{-2}	1.64×10^{-2}	1.81×10^{-2}	3.13×10^{-2}	0.015
	Monsoon	1.07×10^{-3}	1.66×10^{-2}	3.89×10^{-2}	4.92×10^{-2}	9.21×10^{-2}	0.037
	Glacial-Transition	1.17×10^{-3}	2.84×10^{-2}	1.07×10^{-1}	1.78×10^{-1}	2.89×10^{-1}	0.109
	Post-10,000-year	3.98×10^{-3}	9.08×10^{-2}	2.14×10^{-1}	2.69×10^{-1}	3.93×10^{-1}	0.195
	Seepage Fraction	*0.160*	*0.416*	*0.538*	*0.545*	*0.600*	*0.493*
90th p = 0.0596	Present-Day	4.71×10^{-3}	5.17×10^{-2}	8.06×10^{-2}	8.08×10^{-2}	1.24×10^{-1}	0.072
	Monsoon	3.11×10^{-2}	2.99×10^{-1}	4.90×10^{-1}	5.19×10^{-1}	7.09×10^{-1}	0.438
	Glacial-Transition	6.60×10^{-3}	1.30×10^{-1}	3.06×10^{-1}	3.77×10^{-1}	5.62×10^{-1}	0.278
	Post-10,000-year	1.61×10^{-2}	1.56×10^{-1}	2.54×10^{-1}	2.64×10^{-1}	3.72×10^{-1}	0.226
	Seepage Fraction	*0.269*	*0.555*	*0.646*	*0.638*	*0.687*	*0.605*
TSPA Mean Results	Present-Day	5.00×10^{-4}	5.88×10^{-3}	9.36×10^{-3}	1.02×10^{-2}	1.66×10^{-2}	0.009
	Monsoon	2.48×10^{-3}	2.54×10^{-2}	4.38×10^{-2}	4.84×10^{-2}	7.16×10^{-2}	0.040
	Glacial-Transition	9.06×10^{-4}	1.73×10^{-2}	5.40×10^{-2}	8.83×10^{-2}	1.50×10^{-1}	0.056
	Post-10,000-year	3.12×10^{-3}	4.76×10^{-2}	1.03×10^{-1}	1.28×10^{-1}	1.91×10^{-1}	0.095
	Seepage Fraction	*0.125*	*0.340*	*0.437*	*0.437*	*0.494*	*0.400*

NOTE: TSPA seepage data extracted at 500-, 750-, 10,000-, and 1,000,000-year time steps for the present-day, monsoon, glacial-transition, and post-10,000-year climate states, respectively. The data was extracted from the TSPA Nominal Modeling Case for 1,000,000 years and is averaged over the epistemic uncertainties.

Source: [a]GLUE probability weighting factors for the 10th, 30th, 50th, and 90th percentile infiltration realizations: SAR Section 2.3.2.4.1.2.4.5.5.
[b]The seepage values were extracted from the Nominal 1,000,000-year modeling case.
[c]Percolation subregions and quantile ranges SAR Section 2.4.2.3.2.1.2

Table 6. Nominal Modeling Case Commercial SNF Waste Package Average Seepage Rates and Fractions in a Seeping Environment

Nominal Seepage - Commercial SNF Waste Packages in Seeping Environment							
Infiltration Map Percentile[a]	**Climate State**	**Average Flux over the Subregion[b,c] (m^3/yr per waste package)**					**Repository Average (m^3/yr per waste package)**
		1 (0.05)	**2 (0.25)**	**3 (0.4)**	**4 (0.25)**	**5 (0.05)**	
10th p = 0.6191	Present-Day	0.0002	0.0013	0.0020	0.0026	0.0050	0.0020
	Monsoon	0.0025	0.0108	0.0139	0.0151	0.0236	0.0134
	Glacial-Transition	0.0006	0.0043	0.0278	0.0820	0.1617	0.0408
	Post-10,000-year	0.0210	0.0956	0.1264	0.1321	0.1710	0.1171
	Seepage Fraction	*0.099*	*0.295*	*0.370*	*0.359*	*0.416*	*0.337*
30th p = 0.1568	Present-Day	0.0023	0.0118	0.0132	0.0146	0.0241	0.0132
	Monsoon	0.0107	0.0425	0.0480	0.0507	0.0692	0.0465
	Glacial-Transition	0.0116	0.0653	0.1241	0.1722	0.2496	0.1221
	Post-10,000-year	0.0096	0.1030	0.2616	0.3976	0.58442	0.2595
	Seepage Fraction	*0.134*	*0.356*	*0.516*	*0.553*	*0.621*	*0.472*
50th p = 0.1645	Present-Day	0.0038	0.0225	0.0264	0.0274	0.0463	0.0255
	Monsoon	0.0052	0.0365	0.0656	0.0784	0.1382	0.0622
	Glacial-Transition	0.0058	0.0618	0.1831	0.3002	0.4553	0.1868
	Post-10,000-year	0.0226	0.2107	0.3784	0.4618	0.6273	0.3520
	Seepage Fraction	*0.161*	*0.416*	*0.538*	*0.545*	*0.601*	*0.494*
90th p = 0.0596	Present-Day	0.0152	0.0858	0.1131	0.1145	0.1666	0.1044
	Monsoon	0.1142	0.5246	0.7362	0.7871	1.0094	0.6786
	Glacial-Transition	0.0224	0.2243	0.4551	0.5689	0.7970	0.4213
	Post-10,000-year	0.0568	0.2690	0.3777	0.3953	0.5225	0.3461
	Seepage Fraction	*0.270*	*0.556*	*0.647*	*0.638*	*0.689*	*0.605*
TSPA Mean Results	Present-Day	0.0020	0.0115	0.0144	0.0152	0.0244	0.0138
	Monsoon	0.0110	0.0508	0.0710	0.0773	0.1086	0.0664
	Glacial-Transition	0.0044	0.0364	0.0939	0.1610	0.2615	0.1002
	Post-10,000-year	0.0216	0.1260	0.2038	0.2433	0.3314	0.1915
	Seepage Fraction	*0.125*	*0.340*	*0.437*	*0.436*	*0.494*	*0.400*

NOTE: TSPA seepage data extracted at 500-, 750-, 10,000-, and 1,000,000-year time steps for the present-day, monsoon, glacial-transition, and post-10,000-year climate states, respectively. The data was extracted from the TSPA Nominal Modeling Case for 1,000,000 years and is averaged over the epistemic uncertainties.

Source: [a]GLUE probability weighting factors for the 10th, 30th, 50th, and 90th percentile infiltration realizations: SAR Section 2.3.2.4.1.2.4.5.5.
[b]The seepage values were extracted from the Nominal 1,000,000-year modeling case.
[c]Percolation subregions and quantile ranges SAR Section 2.4.2.3.2.1.2.

Table 7. Nominal Modeling Case Codisposal Waste Package Average Seepage Rates and Fractions in a Seeping Environment

Nominal Seepage – Codisposal Waste Packages in Seeping Environment							
Infiltration Map Percentile[a]	**Climate State**	**Average Flux over the Subregion[b,c] (m^3/yr per waste package)**					**Repository Average (m^3/yr per waste package)**
		1 (0.05)	**2 (0.25)**	**3 (0.4)**	**4 (0.25)**	**5 (0.05)**	
10th p = 0.6191	Present-Day	0.0002	0.0015	0.0024	0.0033	0.0057	0.0025
	Monsoon	0.0030	0.0109	0.0148	0.0162	0.0243	0.0140
	Glacial-Transition	0.0006	0.0042	0.0280	0.0823	0.1598	0.0408
	Post-10,000-year	0.0221	0.0935	0.1268	0.1325	0.1688	0.1168
	Seepage Fraction	*0.100*	*0.295*	*0.371*	*0.359*	*0.414*	*0.337*
30th p = 0.1568	Present-Day	0.0027	0.0137	0.0155	0.0171	0.0259	0.0153
	Monsoon	0.0102	0.0442	0.0499	0.0527	0.0684	0.0481
	Glacial-Transition	0.0109	0.0663	0.1239	0.1718	0.2424	0.1218
	Post-10,000-year	0.0098	0.1043	0.2619	0.3975	0.5750	0.2594
	Seepage Fraction	*0.137*	*0.357*	*0.519*	*0.554*	*0.624*	*0.473*
50th p = 0.1645	Present-Day	0.0051	0.0241	0.0316	0.0328	0.0512	0.0297
	Monsoon	0.0054	0.0359	0.0664	0.0785	0.1379	0.0623
	Glacial-Transition	0.0061	0.0608	0.1830	0.2940	0.4448	0.1844
	Post-10,000-year	0.0226	0.2084	0.3788	0.4540	0.6116	0.3488
	Seepage Fraction	*0.158*	*0.414*	*0.539*	*0.546*	*0.600*	*0.493*
90th p = 0.0596	Present-Day	0.0156	0.0906	0.1241	0.1224	0.1764	0.1125
	Monsoon	0.1105	0.5293	0.7373	0.7877	1.0042	0.6799
	Glacial-Transition	0.0211	0.2234	0.4535	0.5648	0.7882	0.4189
	Post-10,000-year	0.0537	0.2699	0.3765	0.3918	0.5175	0.3446
	Seepage Fraction	*0.265*	*0.554*	*0.643*	*0.637*	*0.680*	*0.602*
TSPA Mean Results	Present-Day	0.0023	0.0124	0.0165	0.0174	0.0265	0.0155
	Monsoon	0.0110	0.0513	0.0721	0.0784	0.1085	0.0672
	Glacial-Transition	0.0043	0.0363	0.0938	0.1598	0.2570	0.0996
	Post-10,000-year	0.0221	0.1245	0.2041	0.2421	0.3257	0.1907
	Seepage Fraction	*0.125*	*0.339*	*0.438*	*0.436*	*0.493*	*0.400*

NOTE: Climate states: present-day; monsoon, glacial-transition, and post-10,000-year deep percolation rates. TSPA seepage data extracted at 500-, 750-, 10,000-, and 1,000,000-year time steps for the present-day, monsoon, glacial-transition, and post-10,000-year climate states, respectively. The data was extracted from the TSPA Nominal Modeling Case for 1,000,000 years and is averaged over the epistemic uncertainties.

Source: [a]GLUE probability weighting factors for the 10th, 30th, 50th, and 90th percentile infiltration realizations: SAR Section 2.3.2.4.1.2.4.5.5.
[b]The seepage values were extracted from the Nominal 1,000,000-year modeling case.
[c]Percolation subregions and quantile ranges SAR Section 2.4.2.3.2.1.2.

Table 8. Seismic Ground Motion Modeling Case Average Seepage Rates and Fractions Summary

TSPA Average Seepage for the Seismic GM Modeling Case 1,000,000 Years – Repository Footprint							
Infiltration Map Percentile[a]	**Climate State**	**Average Flux over the Subregion[b,c] (m^3/yr per waste package)**					**Repository Average (m^3/yr per waste package)**
		1	**2**	**3**	**4**	**5**	
		0.05	**0.25**	**0.4**	**0.25**	**0.05**	
10th p = 0.6191	Present-Day	4.19×10^{-5}	5.27×10^{-4}	9.87×10^{-4}	1.25×10^{-3}	2.42×10^{-3}	0.001
	Monsoon	3.77×10^{-4}	3.70×10^{-3}	6.02×10^{-3}	6.53×10^{-3}	1.10×10^{-2}	0.006
	Glacial-Transition	5.31×10^{-4}	2.92×10^{-3}	1.52×10^{-2}	3.68×10^{-2}	8.02×10^{-2}	0.020
	Post-10,000-year	3.61×10^{-2}	1.86×10^{-1}	2.74×10^{-1}	2.61×10^{-1}	3.65×10^{-1}	0.241
	Seepage Fraction	*0.441*	*0.608*	*0.667*	*0.640*	*0.695*	*0.636*
30th p = 0.1568	Present-Day	4.53×10^{-4}	4.99×10^{-3}	8.30×10^{-3}	1.03×10^{-2}	1.70×10^{-2}	0.008
	Monsoon	1.57×10^{-3}	1.65×10^{-2}	2.85×10^{-2}	3.42×10^{-2}	4.80×10^{-2}	0.027
	Glacial-Transition	3.66×10^{-3}	3.21×10^{-2}	8.35×10^{-2}	1.23×10^{-1}	1.89×10^{-1}	0.082
	Post-10,000-year	3.38×10^{-2}	2.23×10^{-1}	6.27×10^{-1}	9.40×10^{-1}	1.39	0.612
	Seepage Fraction	*0.488*	*0.682*	*0.789*	*0.804*	*0.844*	*0.753*
50th p = 0.1645	Present-Day	9.34×10^{-4}	1.08×10^{-2}	1.67×10^{-2}	1.83×10^{-2}	3.16×10^{-2}	0.016
	Monsoon	1.19×10^{-3}	1.70×10^{-2}	3.94×10^{-2}	4.95×10^{-2}	9.27×10^{-2}	0.037
	Glacial-Transition	2.63×10^{-3}	3.45×10^{-2}	1.22×10^{-1}	1.97×10^{-1}	3.18×10^{-1}	0.123
	Post-10,000-year	6.06×10^{-2}	4.37×10^{-1}	8.81×10^{-1}	1.06	1.46	0.804
	Seepage Fraction	*0.503*	*0.717*	*0.799*	*0.797*	*0.831*	*0.765*
90th p = 0.0596	Present-Day	5.08×10^{-3}	5.34×10^{-2}	8.32×10^{-2}	8.35×10^{-2}	1.28×10^{-1}	0.074
	Monsoon	3.22×10^{-2}	3.05×10^{-1}	4.99×10^{-1}	5.29×10^{-1}	7.21×10^{-1}	0.446
	Glacial-Transition	1.10×10^{-2}	1.52×10^{-1}	3.44×10^{-1}	4.18×10^{-1}	6.19×10^{-1}	0.312
	Post-10,000-year	1.30×10^{-1}	6.93×10^{-1}	1.07×10^{-1}	1.13	1.46	0.960
	Seepage Fraction	*0.583*	*0.800*	*0.864*	*0.860*	*0.885*	*0.834*
TSPA Mean Results	Present-Day	5.54×10^{-4}	6.07×10^{-3}	9.63×10^{-3}	1.04×10^{-2}	1.70×10^{-2}	0.009
	Monsoon	2.61×10^{-3}	2.60×10^{-2}	4.46×10^{-2}	4.93×10^{-2}	7.27×10^{-2}	0.040
	Glacial-Transition	1.99×10^{-3}	2.16×10^{-2}	6.30×10^{-2}	9.93×10^{-2}	1.68×10^{-1}	0.064
	Post-10,000-year	4.54×10^{-2}	2.63×10^{-1}	4.76×10^{-1}	5.50×10^{-1}	7.69×10^{-1}	0.434
	Seepage Fraction	*0.467*	*0.649*	*0.719*	*0.705*	*0.752*	*0.687*

NOTE: TSPA seepage data extracted at 500-, 750-, 10,000-, and 1,000,000-year time steps for the present-day, monsoon, glacial-transition, and post-10,000-year climate states, respectively. The data was extracted from the TSPA Seismic Ground Motion Modeling Case for 1,000,000 years and is averaged over the epistemic uncertainties.

Source: [a]GLUE probability weighting factors for the 10th, 30th, 50th, and 90th percentile infiltration realizations: SAR Section 2.3.2.4.1.2.4.5.5.
[b] The seepage values were extracted from the Seismic Ground Motion 1,000,000-year modeling case.
[c]Percolation subregions and quantile ranges SAR Section 2.4.2.3.2.1.2.

Table 9. Seismic Ground Motion Modeling Case Commercial SNF Waste Package Average Seepage Rates and Fractions in a Seeping Environment

Seismic Seepage - Commercial SNF Waste Packages in Seeping Environment							
Infiltration Map Percentile[a]	**Climate State**	**Average Flux over the Subregion[b,c] (m^3/yr per waste package)**					**Repository Average (m^3/yr per waste package)**
		1	**2**	**3**	**4**	**5**	
		0.05	**0.25**	**0.4**	**0.25**	**0.05**	
10th p = 0.6191	Present-Day	0.0001	0.0007	0.0012	0.0015	0.0030	0.001
	Monsoon	0.0008	0.0055	0.0079	0.0085	0.0141	0.007
	Glacial-Transition	0.0012	0.0047	0.0213	0.0519	0.1084	0.028
	Post-10,000-year	0.0845	0.3178	0.4195	0.4090	0.5319	0.380
	Fraction	*0.442*	*0.608*	*0.667*	*0.639*	*0.694*	*0.635*
30th p = 0.1568	Present-Day	0.0008	0.0064	0.0091	0.0108	0.0183	0.0089
	Monsoon	0.0030	0.0221	0.0325	0.0373	0.0527	0.0306
	Glacial-Transition	0.0074	0.0438	0.0979	0.1386	0.2114	0.0957
	Post-10,000-year	0.072514	0.32587	0.78036	1.1307	1.6117	0.760
	Fraction	*0.487*	*0.682*	*0.788*	*0.803*	*0.844*	*0.753*
50th p = 0.1645	Present-Day	0.0016	0.0136	0.0184	0.0195	0.0342	0.0174
	Monsoon	0.0022	0.0219	0.0454	0.0557	0.1031	0.0428
	Glacial-Transition	0.0053	0.0450	0.1424	0.2289	0.3636	0.1439
	Post-10,000-year	0.12621	0.6131	1.0961	1.3128	1.7399	1.013
	Fraction	*0.503*	*0.718*	*0.799*	*0.797*	*0.833*	*0.765*
90th p = 0.0596	Present-Day	0.0081	0.0628	0.0899	0.0904	0.1363	0.0815
	Monsoon	0.0533	0.3680	0.5602	0.5932	0.7938	0.5067
	Glacial-Transition	0.0189	0.1845	0.3884	0.4718	0.6853	0.3547
	Post-10,000-year	0.2318	0.8696	1.2261	1.2932	1.6312	1.1243
	Fraction	*0.584*	*0.800*	*0.864*	*0.861*	*0.886*	*0.834*
TSPA Mean Results	Present-Day	0.0009	0.0075	0.0106	0.0112	0.0185	0.0099
	Monsoon	0.0045	0.0325	0.0511	0.0558	0.0815	0.0468
	Glacial-Transition	0.0039	0.0282	0.0751	0.1196	0.2008	0.0772
	Post-10,000-year	0.0983	0.4004	0.6349	0.7228	0.9643	0.5879
	Fraction	*0.467*	*0.649*	*0.719*	*0.704*	*0.752*	*0.687*

NOTE: TSPA seepage data extracted at 500-, 750-, 10,000-, and 1,000,000-year time steps for the present-day, monsoon, glacial-transition, and post-10,000-year climate states, respectively. The data was extracted from the TSPA Seismic Ground Motion Modeling Case for 1,000,000 years and is averaged over the epistemic uncertainties.

Source: [a]GLUE probability weighting factors for the 10th, 30th, 50th, and 90th percentile infiltration realizations: SAR Section 2.3.2.4.1.2.4.5.5.
[b]The seepage values were extracted from the Seismic Ground Motion 1,000,000-year modeling case.
[c]Percolation subregions and quantile ranges SAR Section 2.4.2.3.2.1.2.

Table 10. Seismic Ground Motion Modeling Case Codisposal Waste Package Average Seepage Rates and Fractions in a Seeping Environment

Seismic Seepage – Codisposal Waste Packages in Seeping Environment							
Infiltration Map Percentile[a]	**Climate State**	**Average Flux over the Subregion[b,c] (m^3/yr per waste package)**					**Repository Average (m^3/yr per waste package)**
		1	**2**	**3**	**4**	**5**	
		0.05	**0.25**	**0.4**	**0.25**	**0.05**	
10th p = 0.6191	Present-Day	0.0001	0.0008	0.0015	0.0019	0.0035	0.0015
	Monsoon	0.0009	0.0055	0.0084	0.0091	0.0145	0.0078
	Glacial-Transition	0.0012	0.0047	0.0213	0.0522	0.1069	0.0281
	Post-10,000-year	0.0849	0.3164	0.4199	0.4098	0.5278	0.3802
	Seepage Fraction	*0.440*	*0.608*	*0.667*	*0.641*	*0.697*	*0.636*
30th p = 0.1568	Present-Day	0.0010	0.0073	0.0108	0.0127	0.0200	0.0104
	Monsoon	0.0029	0.0228	0.0340	0.0389	0.0527	0.0318
	Glacial-Transition	0.0073	0.0440	0.0984	0.1383	0.2072	0.0957
	Post-10,000-year	0.0723	0.3288	0.7862	1.1312	1.6058	0.7634
	Seepage Fraction	*0.489*	*0.681*	*0.789*	*0.804*	*0.845*	*0.753*
50th p = 0.1645	Present-Day	0.0020	0.0146	0.0219	0.0235	0.0384	0.0203
	Monsoon	0.0022	0.0214	0.0459	0.0560	0.1033	0.0430
	Glacial-Transition	0.0052	0.0442	0.1421	0.2249	0.3569	0.1422
	Post-10,000-year	0.1262	0.6129	1.0992	1.3027	1.7298	1.0114
	Seepage Fraction	*0.504*	*0.715*	*0.800*	*0.798*	*0.828*	*0.765*
90th p = 0.0596	Present-Day	0.0084	0.0657	0.0974	0.0960	0.1441	0.0870
	Monsoon	0.0523	0.3686	0.5595	0.5942	0.7903	0.5066
	Glacial-Transition	0.0182	0.1826	0.3863	0.4695	0.6805	0.3525
	Post-10,000-year	0.2323	0.8628	1.2257	1.2925	1.6400	1.1227
	Seepage Fraction	*0.582*	*0.800*	*0.863*	*0.859*	*0.881*	*0.833*
TSPA Mean Results	Present-Day	0.0010	0.0080	0.0120	0.0128	0.0202	0.0111
	Monsoon	0.0045	0.0326	0.0516	0.0565	0.0815	0.0472
	Glacial-Transition	0.0038	0.0280	0.0750	0.1189	0.1979	0.0768
	Post-10,000-year	0.0985	0.3995	0.6366	0.7216	0.9597	0.5878
	Seepage Fraction	*0.467*	*0.648*	*0.720*	*0.705*	*0.753*	*0.687*

NOTE: TSPA seepage data extracted at 500-, 750-, 10,000-, and 1,000,000-year time steps for the present-day, monsoon, glacial-transition, and post-10,000-year climate states, respectively. The data was extracted from the TSPA Seismic Ground Motion Modeling Case for 1,000,000 years and is averaged over the epistemic uncertainties.

Source: [a]GLUE probability weighting factors for the 10th, 30th, 50th, and 90th percentile infiltration realizations: SAR Section 2.3.2.4.1.2.4.5.5.
[b]The seepage values were extracted from the Seismic Ground Motion 1,000,000-year modeling case.
[c]Percolation subregions and quantile ranges SAR Section 2.4.2.3.2.1.2.

1.4 SUMMARY

The results presented in Tables 1 to 11 include the TSPA model percolation and seepage output for the nominal and seismic ground motion modeling cases and are consistent with the summary results presented in SAR Section 2.3.3 for the seepage model and SAR Sections 2.1 (Demonstration of Multiple Barriers) and 2.4 (Demonstration of Compliance with Postclosure Public Health and Environmental Standards). In addition, the TSPA model summary data is consistent with the input from the precipitation and infiltration model results, as documented in SAR Section 2.3.1, and with the site-scale unsaturated zone flow model results, as documented in SAR Section 2.3.2.

Table 11. Summary Values Spatially Averaged over the Repository Footprint

Infiltration Percentile[a]	Climate State	Precipitation (mm/yr)	Unsaturated Zone Flow Model Percolation at the base of PTn (mm/yr)	Ratio of Percolation to Precipitation (%)	MSTHM Percolation at base of PTn (m^3/yr per waste package)	Seepage (m^3/yr per waste package)		Ratio of Seepage to Percolation (%)	
						Nominal	Seismic	Nominal	Seismic
10th p = 0.6191	Present-Day	150.9	4.0	2.7	0.115	0.001	0.001	0.8	0.8
	Monsoon	216.2	7.7	3.6	0.219	0.005	0.006	2.4	2.5
	Glacial-Transition	284.4	11.8	4.1	0.341	0.016	0.020	4.8	5.9
	Post-10,000-year	—	—	—	0.603	0.042	0.241	7.0	40.0
30th p = 0.1568	Present-Day	168.2	10.1	6.0	0.287	0.008	0.008	2.8	2.8
	Monsoon	157.8	15.9	10.1	0.452	0.026	0.027	5.8	5.9
	Glacial-Transition	277.3	25.8	9.3	0.737	0.070	0.082	9.5	11.1
	Post-10,000-year	—	—	—	1.132	0.148	0.612	13.1	54.1
50th p = 0.1645	Present-Day	198.2	14.4	7.3	0.410	0.015	0.016	3.7	3.8
	Monsoon	252.1	19.3	7.7	0.548	0.037	0.037	6.7	6.7
	Glacial-Transition	233.6	35.3	15.1	1.015	0.109	0.123	10.7	12.1
	Post-10,000-year	—	—	—	1.452	0.195	0.804	13.4	55.3
90th p = 0.0596	Present-Day	222.7	33.7	15.1	0.956	0.072	0.074	7.5	7.8
	Monsoon	324.7	91.4	28.1	2.592	0.438	0.446	16.9	17.2
	Glacial-Transition	300.0	68.6	22.9	1.955	0.278	0.312	14.2	15.9
	Post-10,000-year	—	—	—	1.728	0.226	0.960	13.1	55.6
Weighted Mean Results	Present-Day	—	8.44	**TSPA Mean Results**	0.24	0.01	0.01	4.0	4.0
	Monsoon	—	15.88		0.45	0.04	0.04	9.0	9.0
	Glacial-Transition	—	21.25		0.61	0.06	0.06	10.0	10.0
	Post-10,000-year	—	—		0.89	0.1	0.43	11.0	49.0

Source: [a]GLUE probability weighting factors for the 10th, 30th, 50th, and 90th percentile infiltration realizations SAR Section 2.3.2.4.1.2.4.5.5.

2. COMMITMENTS TO NRC

None.

3. DESCRIPTION OF PROPOSED LA CHANGE

None.

4. REFERENCES

SNL (Sandia National Laboratories) 2007. *UZ Flow Models and Submodels*. MDL-NBS-HS-000006 REV 03 AD 01. Las Vegas, Nevada: Sandia National Laboratories. ACC: DOC.20080108.0003; DOC.20080114.0001; LLR.20080414.0007; LLR.20080414.0033; LLR.20080522.0086.

SNL 2008. *Total System Performance Assessment Model /Analysis for the License Application*. MDL-WIS-PA-000005 REV 00 AD 01. Las Vegas, Nevada: Sandia National Laboratories. ACC: DOC.20080312.0001; LLR.20080414.0037; LLR.20080507.0002; LLR.20080522.0113; DOC.20080724.0005.

RAI Volume 3, Chapter 2.2.1.3.6, First Set, Number 6:

Demonstrate that seepage and radionuclide releases are not underestimated by the performance assessment representation of spatial variability in percolation flux. This information is needed to evaluate compliance with 10 CFR 63.114(a), (b), (c), and (e).

Basis: SAR Section 2.3.3.2 describes the ambient seepage model as parameterized by local percolation flux and two hydraulic properties. The local percolation flux used in the seepage model is the product of a percolation flux at the base of the PTn (derived from the site scale flow model) and a sampled flow focusing factor. Site scale flow fields describe percolation fluxes uniformly distributed within a 100 m [330 ft] grid cell at the temporal scale of a climate state, and the seepage model considers steady fluxes at the scale of a few drift diameters (SNL, 2007, Abstraction of Drift Seepage, Section 6.6.2.5.1). Based on this description, the flow focusing factor logically can be considered to represent all seepage affecting variability at spatial scales intermediate between the site scale model grid cell and the drift scale. As described in SAR Section 2.3.3.2 and by SNL (2007), the flow focusing factors are derived from a two dimensional steady state model that considers the region between the base of the PTn and the repository horizon.

Given that the flow focusing factor distribution is based on a model analysis without field observations of flow, the representation of flow focusing factors might not account for all aspects of spatial variability. For example, in some areas, variability could be even smaller than represented in the model, or could be much larger. It is not clear from the SAR and supporting documentation what effect spatial variability at the drift scale has on performance, or if conditions may exist where spatial variability does not affect performance.

Spatial variability may be under represented, when it is not clear that a two dimensional model, which represents flow features as infinite sheets in the third dimension, is representative of a three dimensional model that has flows with a finite extent. Accordingly, high fluxes may be concentrated in a smaller area when a third dimension is considered, implying a larger variability than considered in the flow focusing factor.

Also, spatial variability may be under represented, even if the two dimensional model appropriately characterizes flow in the TSw, when variability in flow at the base of the PTn is not fully considered. The model uses top boundary conditions that are either uniform or have regularly spaced sources. SNL (2007, Figure 6.6 13) suggests that fluxes calculated by the two dimensional model remain coherent at scales on the order of 10 to 20 m [33 to 66 ft], which can be interpreted as implying that flow variability at the base of the PTn at spatial scales as small as 10 m [33 ft] may increase flow variability at the drift scale. Several mechanisms may result in flow variability at this scale, such as (i) localized infiltration, (ii) local heterogeneity in the PTn, and (iii) episodic flow focusing into widely

scattered discrete fast pathways due to temporary perching above the heavily altered low permeability zone at the TCw/PTn transition.

1. RESPONSE

1.1 INTRODUCTION

The RAI and its basis statement raise two questions:

1. The method used to derive the probability distribution of flow-focusing factors may lead to under- or overestimation of percolation-flux variability. Specifically: (a) the two-dimensionality of the high-resolution model used to derive the flow-focusing factor distribution may underestimate flow-focusing effects; and (b) potential variability in the percolation flux at the base of the Paintbrush nonwelded hydrogeological (PTn) unit is not accounted for and thus, may lead to underestimation of percolation-flux variability.

2. The effect of drift-scale spatial variability in percolation flux on radionuclide release is not clear from the SAR and supporting documentation.

This response demonstrates that spatial variability in percolation flux is appropriately represented by the flow-focusing distribution used for the total system performance assessment (TSPA) model, and accordingly, that seepage is not underestimated. Radionuclide releases are not sensitive to spatial variability of seepage because an averaging approach is used in the TSPA model, as discussed in the response to RAI 3.2.2.1.3.6-004.

1.2 VARIABILITY IN PERCOLATION FLUX: GENERAL CONCEPT

Spatial variability in percolation flux is accounted for on three separate scales as follows (SAR Section 2.3.3.2.3.5):

- Variability in percolation flux on the mountain scale is captured by the unsaturated zone site-scale model (SAR 2.3.2.4.2.2; SNL 2007a), which accounts for spatial and temporal variability in infiltration rate, as well as large-scale heterogeneity, specifically the lateral diversion of water at tilted layers and its potential redirection into faults.

- Variability in percolation flux at scales between the site-scale model grid cell and the size of a waste emplacement drift is captured by flow-focusing factors, which are multiplied with the percolation flux at the base of the PTn unit to arrive at local, drift-scale percolation fluxes, which provide the upper boundary condition for the seepage model (SAR Section 2.3.2.2.2.3; SNL 2007b, Section 6.4.2.1).

- Variability in percolation flux on the drift scale is captured by a three-dimensional high-resolution ($0.1 \times 0.3 \times 0.1$ m) numerical model of seepage that uses a stochastic continuum representation of fracture permeability (SAR Section 2.3.3.2.3.2; SNL 2007b, Section 6.4.2.1).

1.3 DERIVATION OF FLOW-FOCUSING FACTOR DISTRIBUTION

1.3.1 Three-Dimensional Effects on Flow-Focusing Factor Distribution

The effect of flow dimensionality (two- vs. three-dimensional) on the flow-focusing factor distribution was studied by Bodvarsson et al. (2003). The model domain between the PTn and the repository horizon was discretized in a three-dimensional uniform grid with a resolution of $0.5 \times 0.5 \times 0.75$ m, resulting in 2,000,000 gridblocks. Different infiltration distributions at the top boundary were specified, and the resulting flow distribution across the bottom boundary was analyzed and compared to the flow-focusing factor distributions obtained with the two-dimensional model. The differences between the two-dimensional and three-dimensional flow-focusing models can be summarized as follows:

(1) The two- and three-dimensional models show differences in the frequencies of low and intermediate fluxes, but are statistically equivalent for high normalized fluxes.

(2) Compared to the three-dimensional flow-focusing model, the two-dimensional model predicts higher frequencies for intermediate flow-focusing factors (in the range between flow-focusing factors of 1 and 3), and lower frequencies for flow-focusing factors below one (Bodvarsson et al. 2003, Figure 11). This behavior (i.e., reduced frequencies below a flow-focusing factor of one, which is compensated by increased frequencies above that threshold) is expected from the averaging that occurs when combining a flux distribution in the third dimension into a single value to arrive at a two-dimensional representation of the system.

(3) Flow-focusing factors from both models are relatively insensitive to the average percolation flux, with larger total fluxes reducing flow redistribution. Flow focusing is only expected to change with average percolation flux if saturation is varied significantly, leading to corresponding nonlinear effects in relative permeability and capillarity that induce a different flow pattern. Because of the high absolute permeability of the fracture network, saturation changes and the related nonlinear effects are minor, leading to the relative insensitivity of the flow-focusing factor distribution with respect to percolation flux.

(4) The three-dimensional model requires somewhat longer travel distances to stabilize flow focusing (Bodvarsson et al. 2003, Figure 12); the three-dimensional flow paths are more tortuous.

Points (1) and (2) above indicate that the two-dimensional model used to derive the flow-focusing factor distribution for TSPA leads to more (not less) flow focusing than the three-dimensional model (i.e., higher likelihood that the TSPA model will sample values for the flow-focusing factor greater than one).

1.3.2 Impact of PTn Variability on Flow-Focusing Factor Distribution

The flow-focusing factor distribution is insensitive to the spatial distribution of water release at the base of the PTn. This has been demonstrated by comparing three different release patterns at the top of the model (uniform, locally concentrated, and nonuniform, according to available hydraulic conductivity) (BSC 2004, Section 6.8, Figure 6-26; Bodvarsson et al. 2003, Figure 7). Uniformly or nonuniformly distributed flow in the PTn is mainly redistributed at the contact between the PTn and the Topopah Spring welded hydrogeological unit (TSw), at other interfaces between subunits of the TSw, and within the TSw units. The flow patterns are determined by the fracture heterogeneity of the TSw rather than flow variability in the PTn (BSC 2004, p. 6-36).

Figure 6-26 of *Seepage Model for PA Including Drift Collapse* (BSC 2004) demonstrates that potential non-uniformity of percolation flux arriving at the base of the PTn has an insignificant impact on the flow distribution at the repository horizon.

1.3.3 Additional Evidence Supporting Flow-Focusing Factor Distribution

The two-dimensional flow-focusing model has a fine horizontal resolution of 0.25 m (BSC 2004, Section 6.8.1), which is much smaller than the horizontal extent of the drift-scale seepage model to which the flow-focusing factors are applied. This higher resolution leads to stronger flow focusing (i.e., a wider distribution with higher frequencies for flow-focusing factors other than one), as demonstrated in a grid-resolution analysis (SNL 2007b, Figure 6.6-16). The flow-focusing factor distribution used in the TSPA model thus likely overestimates rather than underestimates the variability in percolation flux arriving at the repository horizon. Note that a flatter flow focusing factor distribution (i.e., greater variability in local percolation fluxes) implies increased flow focusing, with relatively few areas encountering higher percolation fluxes, and relatively many areas encountering lower percolation fluxes.

The concept of flow focusing is corroborated by data collected at Yucca Mountain (SNL 2007b, Section 6.6.5.2.3). While it is difficult to quantitatively validate flow focusing for the specific range of scales represented by flow-focusing factors (from 100 m to 5 m, for the site-scale and drift-scale models, respectively), the distribution of calcite in fractures and lithophysal cavities, and the relative uniformity of water potentials in the TSw, indicate that there are many small flow paths instead of a few large flow channels. These observations are thus consistent with the model-derived flow-focusing factor distribution (BSC 2004, Section 7.4).

Tokunaga et al. (2005) performed flow-focusing experiments using packings of unsaturated rocks, demonstrating that a well-constrained distribution of fluxes develops despite differences in rock type and packing. Their experimentally determined flow-focusing distribution (Tokunaga et al. 2005, Figure 4) is very similar, in both range and shape, to the model-derived distribution used in the TSPA model.

In summary, laboratory and field observations, as well as alternative conceptual models, confirm the reasonableness of the flow-focusing factor distribution used in the TSPA model.

1.4 SENSITIVITY OF SEEPAGE AND REPOSITORY PERFORMANCE

1.4.1 Sensitivity of Seepage to Spatial Variability in Percolation

Probabilistic seepage calculations have been performed using alternative flow-focusing distributions that represent more or less variability (SNL 2007b, Section 6.8.2). Four cases with different flow-focusing distributions were analyzed, ranging from no flow focusing to very strong flow focusing (up to a factor of 33). The results are discussed in *Abstraction of Drift Seepage* (SNL 2007b, Section 6.8.2, Case 6). As expected, stronger flow focusing leads to fewer seeps with higher seepage rates. However, the impact of these counteracting effects is limited. For example, in the extreme case (Case 6c), the seepage fraction decreased by 10% (from 24% to 14% for the glacial transition climate), and the mean seepage rate (over all waste packages) increased by 89 kg/yr per waste package (from 38 to 127 kg/yr per waste package). This extreme case is used for exploratory purposes only and is based on a bounding analysis using estimates of the spacing between active fractures in a previous version of the unsaturated zone flow model. It is considered unrealistic because the spacing between active fractures is partly incorporated into smaller scale variability than is represented by flow focusing. As applied in the TSPA, the focusing results obtained for different flux values are statistically similar (SNL 2007b, Section 6.6.5.2.1).

1.4.2 Sensitivity of Repository Performance to Spatial Variability in Seepage

Drift seepage rates are expected to vary spatially over the length of the emplacement drifts. This means that emplacement drifts can exhibit seeping and nonseeping environments (SNL 2008, Section 6.3.3.1.1). In the TSPA model, this spatial variability is represented by partitioning the waste packages into the seeping and non-seeping environments by means of the seepage fraction. The seepage fraction is the ratio of the number of waste packages experiencing seepage to the total number of waste packages in a percolation subregion; separate values are computed for codisposal and commercial spent nuclear fuel (SNF) waste packages.

The two modeling cases in the TSPA that contribute the most (roughly 98%) to the total mean annual dose within 1,000,000 years after closure are the igneous intrusion and seismic ground motion modeling cases (SAR Figure 2.4-18). In the igneous intrusion modeling case, after an intrusion occurs, the TSPA model does not use the seepage or flow-focusing abstractions; instead, percolation flux is spatially averaged within each of the five percolation subregions and the average flux is applied to all waste packages (i.e., the seepage fraction is one). In the seismic ground motion modeling case, seepage is computed at each waste package location within a percolation subregion. The seepage rate at each location is compared to a threshold seepage rate of 0.1 kg/yr per waste package (SNL 2008, Section 6.3.3.1.3). Waste package locations with less than this threshold rate are counted as non-seeping locations and a rate of 0 kg/yr is applied. The average seepage rate is computed for locations with seepage, and this spatially-averaged seepage flux is applied at all seeping locations. The response to RAI 3.2.2.1.3.6-004 provides justification for the use of spatially averaged percolation and seepage rates, rather than spatially-variable rates. Specifically, the response to RAI 3.2.2.1.3.6-004 shows that the use of spatially-averaged seepage rates produce equivalent mass releases from the Engineered Barrier

System (EBS) in each percolation subregion as would be obtained from the use of spatially-variable seepage rates.

The lack of sensitivity of repository performance to uncertainty in seepage fraction is demonstrated by Figure 1. Figure 1a shows the relationship between seepage fraction for codisposal waste packages in percolation subregion 3 and expected annual dose at 10,000 years for the seismic ground motion modeling case. As discussed in SAR Section 2.4.2.2.1.1.2, total mean dose to the reasonably maximally exposed individual (RMEI) for 10,000 years after permanent closure is dominated by contributions from the seismic ground motion modeling case, and this dose results from seismic damage to codisposal waste packages. For this demonstration, seepage fractions from percolation subregion 3 are selected, because this subregion comprises 40% of the waste packages in the repository. The variability in both seepage fraction and expected annual dose on Figure 1a results from epistemic uncertainty, because the expected annual dose has been integrated over aleatory uncertainty in seismic events. The lack of any correlation between seepage fraction and expected annual dose demonstrates that the mean annual dose for 10,000 years after permanent closure is not sensitive to the spatial variability in seepage represented by the seepage fraction. Rather, the uncertainty in the expected annual dose is dominated by epistemic uncertainty in the residual stress threshold for Alloy 22 (SAR Section 2.4.2.3.3.6), with minor sensitivities to other uncertain inputs (SAR Figure 2.4-149). Examination of other percolation subregions would reach a similar conclusion because the uncertainty in expected annual dose is not strongly influenced by uncertainty in quantities that vary between the percolation subregions (i.e, seepage fraction). Moreover, the results shown in Figure 1a cover most of the range of seepage fraction (nearly 0 to greater than 0.8) that is observed in the other percolation subregions.

Figure 1b shows the relationship between seepage fraction for commercial SNF waste packages in percolation subregion 3 and expected annual dose at 1,000,000 years for the seismic ground motion modeling case (which includes the effects of nominal processes). As discussed in SAR Section 2.4.2.2.1.1.2, total mean dose to the RMEI at 1,000,000 years after permanent closure results is comprised of roughly equal contributions from the seismic ground motion modeling case (which uses the seepage abstraction) and the igneous intrusion modeling case (which does not use the seepage abstraction). Moreover, in the seismic ground motion modeling case, the expected annual dose after about 500,000 years after permanent closure is dominated by releases from commercial SNF waste packages, which in turn results primarily from waste package failures associated with nominal processes. The lack of any correlation between seepage fraction and expected annual dose demonstrates that the mean annual dose at 1,000,000 years after permanent closure is not sensitive to the spatial variability in seepage represented by the seepage fraction. Rather, the uncertainty in the expected annual dose is dominated by epistemic uncertainty in the temperature dependence coefficient associated with the general corrosion rate for Alloy 22 (SAR Section 2.4.2.3.3.6), with minor sensitivities to other uncertain inputs (SAR Figure 2.4-151).

In summary, the EBS flow and transport models are not sensitive to spatial variability in percolation (and seepage) flux. Considering a single percolation subregion, spatially-averaged seepage rates yield equivalent mass releases as would be obtained from the use of spatially-variable seepage rates. Repository performance (i.e., expected annual dose) is not

sensitive to uncertainty in the fraction of waste packages which experience seepage (i.e., seepage fraction).

1.5 SUMMARY AND CONCLUSIONS

This response provides information that demonstrates that:

- The two-dimensional model used to derive the flow-focusing factor distribution for the TSPA model leads to more (not less) flow focusing than the three-dimensional model.

- Regardless of the mechanisms leading to potential variability (at scales smaller than the grid resolution of the UZ flow model) in percolation flux arriving at the base of the PTn, such flow variability in the PTn has an insignificant impact on the flow distribution at the repository horizon.

- The range and shape of the flow-focusing factor distribution are reasonable and supported by laboratory and field observations as well as alternative conceptual models (BSC 2004, Section 7.4).

- Sensitivity studies demonstrate the relative insensitivity of (1) seepage rates to uncertainty in percolation flux distribution, and (2) repository performance to uncertainty in seepage fraction.

- Repository performance is not sensitive to spatial variability in seepage.

- Also, the TSPA representation of spatial variability for the percolation flux does not underestimate the seepage rates. This representation does not underestimate radionuclide releases.

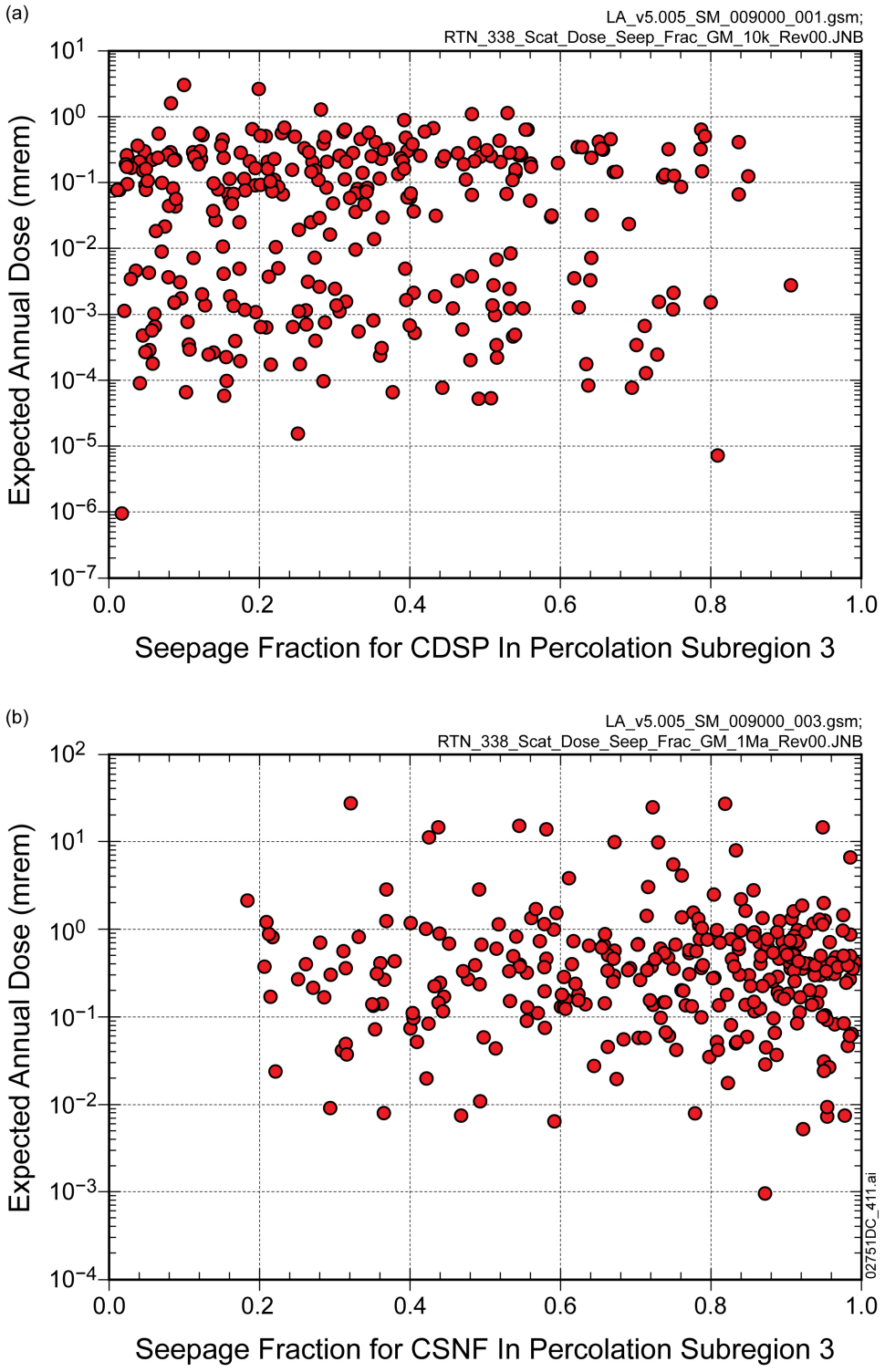

Figure 1. Correlation between Seepage Fraction and Expected Annual Dose at (a) 10,000 Years and (b) 1,000,000 Years for the Seismic Ground Motion Modeling Case

2. COMMITMENTS TO NRC

None.

3. DESCRIPTION OF PROPOSED LA CHANGE

None.

4. REFERENCES

Bodvarsson, G.S.; Wu, Y.S.; and Zhang. K. 2003. "Development of Discrete Flow Paths in Unsaturated Fractures at Yucca Mountain." *Journal of Contaminant Hydrology*, 62-63, 23-42. New York, New York: Elsevier.

BSC (Bechtel SAIC Company) 2004. *Seepage Model for PA Including Drift Collapse*. MDL-NBS-HS-000002 REV 03. Las Vegas, Nevada: Bechtel SAIC Company. ACC: DOC.20040922.0008; DOC.20051205.0001.

SNL (Sandia National Laboratories) 2007a. *UZ Flow Models and Submodels.* MDL-NBS-HS-000006 REV 03 AD 01. Las Vegas, Nevada: Sandia National Laboratories. ACC: DOC.20080108.0003; DOC.20080114.0001; LLR.20080414.0007; LLR.20080414.0033; LLR.20080522.0086.

SNL 2007b. *Abstraction of Drift Seepag*e. MDL-NBS-HS-000019 REV 01 AD 01. Las Vegas, Nevada: Sandia National Laboratories. ACC: DOC.20070807.0001; DOC.20080813.0004.

SNL 2008. *Total System Performance Assessment Model /Analysis for the License Application*. MDL-WIS-PA-000005 REV 00 AD 01. Las Vegas, Nevada: Sandia National Laboratories. ACC: DOC.20080312.0001; LLR.20080414.0037; LLR.20080507.0002; LLR.20080522.0113; DOC.20080724.0005; DOC.20090106.0001[a].

Tokunaga, T.K.; Olson, K.R.; and Wan, J. 2005. "Infiltration Flux Distributions in Unsaturated Rock Deposits and Their Potential Implications for Fractured Rock Formations." *Geophysical Research Letters*, 32, (L05405), 1-4. Washington, D.C.: American Geophysical Union.

NOTE: [a]Provided as an enclosure to letter from Williams to Sulima dtd 02/17/2009. "Yucca Mountain – Request for Additional Information Re: License Application (Safety Analysis Report Section 2.1), Safety Evaluation Report Volume 3 – Postclosure Chapters 2.2.1.1 and 2.2.1.3.7 – Submittal of Department of Energy Reference Citations."

RAI Volume 3, Chapter 2.2.1.3.6, First Set, Number 7:

> Describe the seepage, release, and transport sensitivity arising from the use of the GLUE procedure in performance assessment, including changes in estimated uncertainty. This information is needed to evaluate compliance with 10 CFR 63.114(a), (b), and (c).
>
> Basis: The GLUE procedure results in a set of weights applied to the infiltration scenarios (SAR Section 2.3.2.4.1.2.4.5.5). These weights yield lower expected mean annual infiltration than the original weights provided in SNL (2008). The SAR and supporting documents do not clearly describe how performance changes when the infiltration scenario weights are modified using the GLUE procedure. Therefore, it is not possible to evaluate the effects of the GLUE-derived weights on seepage, release, and transport.

1. RESPONSE

As discussed at the clarification call with NRC on April 28, 2009, the response provides an analysis comparing mean doses and seepage rates from the total system performance assessment (TSPA) for the license application base case using the generalized likelihood uncertainty estimation (GLUE) weighting procedure, with an analysis without GLUE weighting, referred to here as "unweighted" values. The analysis compares seepage and percolation rates for the GLUE-weighted and unweighted cases, mean annual dose to the reasonably maximally exposed individual (RMEI) for the seismic ground motion and igneous intrusion modeling cases, and total mean annual dose to the RMEI for the 10,000-year time frame. The analysis demonstrates that use of the GLUE weighting procedure has only a minor effect on demonstration of compliance with the individual protection standard (10 CFR 63.311). As explained in SAR Section 2.3.2.4.1.2.4.5, the license application base case applies GLUE weighting to calibrate unsaturated zone flow model results to measurements of temperature and chloride in the unsaturated zone. The unweighted case is considered only to demonstrate the potential sensitivity of license application results to the application of GLUE weighting.

1.1 COMPARISON OF WEIGHTED AND UNWEIGHTED INFILTRATION SCENARIOS

The input parameter, *INFIL* (TSPA name: Infiltration_Scenario_a; SNL 2008, Table K3-1), is used to select one of four time-dependent sequences of unsaturated zone flow fields within the TSPA model. *INFIL* is a pointer variable with values between 1 and 4 to specify which of the four unsaturated zone flow field sequences is used in each realization of the TSPA calculation. The four unsaturated zone flow field sequences are referred to as the 10th, 30th, 50th, or 90th percentile infiltration maps, which identify the infiltration cases used as upper boundary conditions in the unsaturated zone flow model.

In the base case, the probabilities for selecting values of 1, 2, 3, or 4 for the parameter *INFIL* are 0.6191, 0.1568, 0.1645, and 0.0596, respectively (SAR Table 2.3.2-27). These probabilities result from GLUE weighting of the net infiltration maps using measurements of chloride and temperature within the unsaturated zone.

In the unweighted case, the probabilities of selecting values 1, 2, 3, or 4 for the parameter *INFIL* are 0.2, 0.2, 0.3, and 0.3, respectively; these probabilities result from considering only the prior uncertainty in the net infiltration maps (SNL 2007, Section 6.8). The unweighted distribution favors the higher infiltration cases, and thus increases the likelihood of larger volumes of water flowing through the system. The expected value of the mean annual infiltration over the repository footprint can be calculated as the sum of the product of the mean annual net infiltration averaged over the repository footprint and the weighting factor for each map. This expected value increased for the unweighted analysis by 104% as compared to the GLUE-weighted results (from 8.44 to 17.25 mm/yr) for present-day, by 139% (from 15.88 to 37.93 mm/yr) for monsoon, and by 82% (from 21.25 to 38.69 mm/yr) for glacial-transition climates (see Table 1 of response to RAI 3.2.2.1.3.6-005). Table 1 compares the two distributions for values of *INFIL*.

Table 1. GLUE-weighted and Unweighted Distributions for *INFIL*

	GLUE Weighted[a]	Unweighted
INFIL = 1	0.6191	0.2
INFIL = 2	0.1568	0.2
INFIL = 3	0.1645	0.3
INFIL = 4	0.0596	0.3

Source: [a] GLUE weighting factors for the 10th, 30th, 50th, and 90th percentile infiltration cases: SAR Section 2.3.2.4.1.2.4.5.5.

1.2 EFFECT OF UNWEIGHTED INFIL VALUES ON PERCOLATION AND SEEPAGE RATES

The unweighted case results in higher likelihood of larger values of *INFIL* (Table 1), which corresponds to greater mean annual net infiltration, and consequently higher likelihood of greater average percolation flux. Figure 1 compares the distributions for the repository average percolation rate per waste package during the glacial-transition climate for the GLUE-weighted and unweighted analyses. Each distribution shown on Figure 1 consists of four discrete values because these results have been averaged spatially within each percolation subregion and over the five percolation subregions. The uncertainty in these results arises only from the selection of the infiltration case. Higher percolation rates are more likely in the unweighted analysis, which leads to an increase in the mean repository average percolation per waste package during the glacial-transition climate by a factor of about 80%, from 0.61 to 1.1 m^3/yr. For all climate states, Table 2 shows the increase in mean percolation flux at the base of the Paintbrush nonwelded (PTn) unit over the repository footprint resulting from the use of unweighted distribution for *INFIL*. Note that the average infiltration fluxes (Section 1.1) and percolation fluxes (Table 2) over the repository footprint are not necessarily equal because of the following three factors:

(1) the horizontal extent of the unsaturated zone flow model domain is larger than the repository footprint; (2) the infiltration rate is spatially variable; and (3) lateral flow can occur. Therefore, infiltration variations at locations adjacent to the repository footprint, combined with lateral flow, can lead to differences between the average percolation and infiltration fluxes over the repository footprint.

Table 2. Mean Percolation Flux (mm/yr) over Repository Footprint at the Base of the PTn for Each Climate State

Climate State	Mean Percolation Rate (mm/yr)		Increase (%)
	Base Case[a]	Unweighted Case	
Present-Day	8.6	17.5	104
Monsoon	16.1	38.4	139
Glacial-Transition	21.8	39.5	81

Source: [a] SNL 2007, Table H-2.

Percolation rates are inputs to the seepage abstraction, which computes the quantity of percolation entering the repository drift as seepage. Figure 2 compares the cumulative distributions for spatially-averaged seepage rates in the five percolation subregions for the GLUE-weighted analysis and the unweighted analyses. Uncertainty in seepage rates arises from epistemic uncertainty in parameters that affect seepage rates. The spatially-averaged seepage rates shown in Figure 2 are the annual volumes of water seeping onto the drip shield over a single commercial spent nuclear fuel (SNF) waste package in the glacial-transition climate state. Comparison of GLUE-weighted and unweighted seepage rates would be similar for codisposal waste packages and for all climate states. In all percolation subregions, higher seepage rates are more likely for the unweighted analysis. Figure 3 compares the cumulative distributions for the seepage fraction in the five percolation subregions. The seepage fraction is the fraction of the waste packages in a percolation subregion that are in a seeping environment; uncertainty in seepage fraction also arises from epistemic uncertainty in parameters that affect seepage rates. Figure 3 shows a greater likelihood of higher seepage fraction in all five percolation subregions for the unweighted analysis.

Figure 4 compares the distribution of repository average seepage rates for the glacial-transition climate state, calculated as the product of the seepage rate per waste package, seepage fraction for each percolation subregion, and the corresponding fraction of the repository in each percolation subregion (0.05, 0.25, 0.4, 0.25, and 0.05). Consistent with Figure 2, higher repository average seepage rates are more likely in the unweighted analysis, where the mean repository average seepage rate per waste package increases by about a factor of 2.5, from 0.056 to 0.14 m^3/yr.

1.3 RESULTS FOR THE SEISMIC GROUND MOTION MODELING CASE

The mean annual dose from the seismic ground motion modeling case is the largest contributor to the total mean annual dose at 10,000 years, comprising about 70% of the total (SAR Figure 2.4-18(a)). Figure 5 compares the distribution of expected annual dose from seismic ground motion for (a) the base-case TSPA model results, using the distribution for *INFIL* that

results from GLUE weighting of infiltration maps by considering chloride and temperature data from the unsaturated zone, and (b) the analysis using the unweighted distribution for *INFIL*. Figure 5 shows that the range of uncertainty in expected annual dose is not significantly affected by GLUE weighting applied to the parameter *INFIL*. Sensitivity analyses reported in *Total System Performance Assessment Model/Analysis for the License Application* (SNL 2008, Section K.7.7.1[a]) demonstrate that the most significant uncertain input parameter that contributes to uncertainty in expected annual dose is the residual stress threshold for Alloy 22 (*SCCTHRP*), which accounts for 88% of the uncertainty in the expected annual dose at 10,000 years (SNL 2008, Figure K7.7.1-2[a](a)). Uncertainty in the parameter *INFIL* has a relatively minor effect on uncertainty in expected annual dose from seismic ground motion, accounting for less than 1% of the uncertainty in the expected annual dose (SNL 2008, Figure K7.7.1-2[a](a)).

Figure 6 shows the effect of GLUE weighting on the magnitude of the mean annual dose for the seismic ground motion modeling case during the first 10,000 years after closure. Using the unweighted distribution somewhat increases mean annual dose for all times, with the largest increase occurring before 3,000 years when the mean annual dose is small relative to its maximum value over 10,000 years. The increase in mean annual dose at early times results from the higher likelihood of larger volumes of water flowing through the system, which in turn results in more rapid transport of radionuclides through the Lower Natural Barrier. The maximum of the mean annual dose from seismic ground motion (occurring at 10,000 years) increases only by approximately 9%, from 0.170 to 0.185 mrem. The increase in the maximum of the mean annual dose is small because radionuclide transport from the waste packages is limited by diffusion through stress-corrosion cracks in the waste package outer barrier (SNL 2008, Section 8.1.1.5[a]). In these circumstances, seepage water does not advect through the waste packages; rather, radionuclide transport occurs by diffusion through adsorbed water inside the waste package and through tight, tortuous cracks in the waste package outer barrier.

Figure 7 compares the contribution of each radionuclide to mean annual dose for the base case and for the unweighted analysis. Increasing the volume of water flow through the unsaturated zone can lead to earlier occurrence of seepage and higher relative humidity in the drift, which can result in earlier releases of ^{99}Tc (a highly soluble, nonsorbing radionuclide) from the Engineered Barrier System (EBS) (SNL 2008, Figure K7.3-9). Increased water flow can also accelerate the rate of transport of ^{99}Tc through the Lower Natural Barrier (SNL 2008, Figures K7.4-5 and K7.5-5). Thus, increasing water flow through the unsaturated zone affects the contribution of ^{99}Tc to the mean annual dose, by increasing concentrations of ^{99}Tc in the saturated zone. However, the dose from ^{99}Tc is primarily limited by its initial mass in the waste, the rate of release from the waste form, and the rate of diffusion through the waste package (SNL 2008, Section K7.3). Thus, increasing the volume of water flow through the unsaturated zone results in only a moderate increase (from 0.103 to 0.108 mrem) in the mean annual dose from ^{99}Tc (Figure 7). Because ^{99}Tc is the dominant radionuclide contributing to mean annual dose from seismic ground motion within 10,000 years (Figure 7), using the GLUE-weighted or unweighted distribution for the *INFIL* parameter does not significantly affect the maximum of the mean annual dose from the seismic ground motion modeling case.

In contrast, radionuclides with solubility limits and which may also sorb to ferric corrosion products, such as ^{239}Pu, are transported in negligible quantities (SNL 2008, Figure K7.3-7), primarily due to the limited volume of water present inside the waste package. Increased water flow through the unsaturated zone may result in greater mass transport, by reducing the concentration of these radionuclides in the invert and thus enhancing diffusion from the waste package; concentrations of radionuclides in the saturated zone may also increase. Increased water flow represented by the unweighted analysis increases the contribution to mean annual dose from solubility-limited radionuclides such as ^{239}Pu. However, the contribution from these radionuclides remains far below contributions from highly soluble elements such as technetium.

1.4 RESULTS FOR THE IGNEOUS INTRUSION MODELING CASE

The seepage model is not used to estimate the rate of water flow into the repository drifts after an igneous intrusion occurs. Rather, seepage into a percolation subregion is set equal to the spatially-averaged percolation flux for that subregion at the base of the PTn. The effect of using unweighted *INFIL* values on spatially-averaged percolation flux is shown on Figure 1. The mean annual dose from the igneous intrusion modeling case is the second largest contributor to the total mean annual dose at 10,000 years, comprising approximately 27% of the total (SAR Figure 2.4-18(a)). Figure 8 compares the distribution of expected annual dose for the igneous intrusion modeling case for (a) the base-case TSPA model results, using the distribution for *INFIL* resulting from GLUE weighting, and (b) the analysis using the unweighted distribution for *INFIL*. Figure 8 also shows that the range of uncertainty in expected annual dose is not significantly affected by the use of weighted or unweighted distributions for the parameter *INFIL*. Sensitivity analyses reported in *Total System Performance Assessment Model/Analysis for the License Application* (SNL 2008, Section K.6.7.1[a]) demonstrate that uncertainty in the expected annual dose arises primarily from uncertainty in the frequency of occurrence of igneous events (*IGRATE*), accounting for 76% of the uncertainty in the expected annual dose at 10,000 years (SNL 2008, Figure K6.7.1-2[a](a)). Uncertainty in the parameter *INFIL* has a relatively minor effect on uncertainty in expected annual dose from igneous intrusion, accounting for about 2% of the uncertainty in expected annual dose (SNL 2008, Figure K6.7.1-2[a](a)).

Figure 9 shows the effect of GLUE weighting on the magnitude of the mean annual dose from igneous intrusion. Use of the unweighted distribution increases mean annual dose for all times. At 10,000 years, mean annual dose from igneous intrusion increases by approximately 81%, from 0.0661 mrem to 0.119 mrem, similar to the increase in mean percolation rates (Table 2), which in turn results in higher likelihood of increased transport of radionuclides. Figure 10 compares the contribution of each radionuclide to mean annual dose for both cases. In the base case, at 10,000 years, ^{239}Pu is the largest contributor to mean annual dose resulting from igneous intrusion, with ^{99}Tc making a significant but somewhat smaller contribution. Increased water flow resulting from the use of the unweighted distribution increases the contribution to mean annual dose from solubility-limited elements such as plutonium and neptunium. Increased water flow somewhat accelerates the movement of highly soluble elements such as technetium and iodine, but does not significantly affect the contribution from highly soluble elements to mean annual dose.

Regression analyses for the igneous intrusion modeling case indicate a fairly strong increasing relationship between uncertainty in net infiltration (*INFIL*) and the mass of plutonium that is transported from the waste through the EBS and unsaturated zone (SNL 2008, Figures K6.3.1-1, K6.3.1-7, K6.3.2-1, K6.3.2-4, K6.4.1-1, K6.4.1-4, and K6.4.1-10), as well as a moderately strong increasing relationship between uncertainty in net infiltration (*INFIL*) and the mass of plutonium that is transported through the saturated zone (SNL 2008, Figures K6.5.1-1 and K6.5.1-10). The reduction in importance of uncertainty in net infiltration to transport of plutonium in the saturated zone results from the relatively stronger contribution to uncertainty in transport from uncertain parameters affecting saturated zone transport, such as groundwater specific discharge (*SZGWSPDM*).

1.5 EFFECT ON TOTAL MEAN ANNUAL DOSE

The mean annual doses from the modeling cases are summed to obtain the total mean annual dose to the RMEI. The maximum of the total mean annual dose is compared with the limit specified for the individual protection standard at 10 CFR 63.3119(a)(1). Use of unweighted rather than GLUE-weighted infiltration cases increases the mean annual dose from each modeling case. Adding the mean annual doses from each modeling case results in a maximum total mean annual dose at 10,000 years of 0.31 mrem/yr for the unweighted case, compared to 0.24 mrem/yr in the base-case TSPA model (SNL 2008, Section 8.2[a]). However, in either the unweighted or the base case, the maximum of the total mean annual dose (0.31 and 0.24 mrem/yr, respectively) is a small fraction (2.1% and 1.6%) of the limit (15 mrem/yr) specified by the individual protection standard. Thus, using either unweighted or GLUE-weighted values for the *INFIL* parameter does not significantly affect the total mean annual dose relative to the individual protection standard.

1.6 SUMMARY

Results of this analysis demonstrate that use of GLUE weighting has little effect on the demonstration of compliance with the individual protection standard. Use of unweighted rather than GLUE-weighted infiltration cases moderately increases the total mean annual dose to the RMEI within 10,000 years. However, the increase is small relative to the difference between the total mean annual dose and the individual protection standard. The maximum of the total mean annual dose within 10,000 years occurs at 10,000 years; the dominant contribution to total mean annual dose at 10,000 years is from ^{99}Tc released from the waste following seismic events that damage waste packages. Because the contribution to mean annual dose from ^{99}Tc is primarily limited by diffusion of ^{99}Tc from the waste package, increasing water flow through the unsaturated zone results in only a moderate increase in dose from ^{99}Tc. Moreover, the uncertainty in total expected annual dose before 10,000 years predominately results from uncertainty in the occurrence of seismic damage and igneous events (SNL 2008, Figure 8.1-2[a](a)), rather than from the uncertainty associated with infiltration, percolation, or seepage. Thus, the use of the GLUE-weighted distribution for the *INFIL* parameter does not significantly affect the conclusions of the performance assessment.

2. COMMITMENTS TO NRC

None.

3. DESCRIPTION OF PROPOSED LA CHANGE

None.

4. REFERENCES

SNL (Sandia National Laboratories) 2007. *UZ Flow Models and Submodels.* MDL-NBS-HS-000006 REV 03 AD 01. Las Vegas, Nevada: Sandia National Laboratories. ACC: DOC.20080108.0003; DOC.20080114.0001; LLR.20080414.0007; LLR.20080414.0033; LLR.20080522.0086.

SNL 2008. *Total System Performance Assessment Model/Analysis for the License Application*. MDL-WIS-PA-000005 REV 00 AD 01. Las Vegas, Nevada: Sandia National Laboratories. ACC: DOC.20080312.0001; LLR.20080414.0037; LLR.20080507.0002; LLR.20080522.0113; DOC.20080724.0005; DOC.20090106.0001[a].

NOTE: [a]Provided as an enclosure to letter from Williams to Sulima dtd 02/17/2009. "Yucca Mountain – Request for Additional Information Re: License Application (Safety Analysis Report Section 2.1), Safety Evaluation Report Volume 3 – Postclosure Chapters 2.2.1.1 and 2.2.1.3.7 – Submittal of Department of Energy Reference Citations."

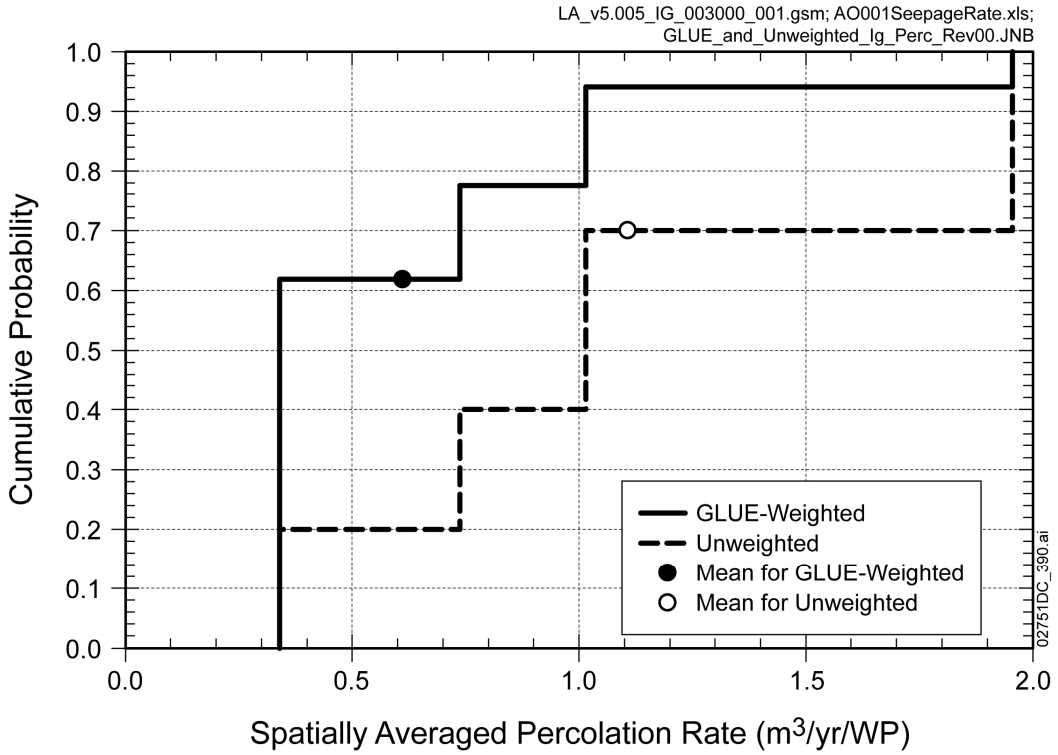

Figure 1. Comparison of the Cumulative Distribution Functions of Spatially-Averaged Percolation Rate per Commercial SNF Waste Package during the Glacial-Transition Climate for the GLUE-weighted and Unweighted Analyses

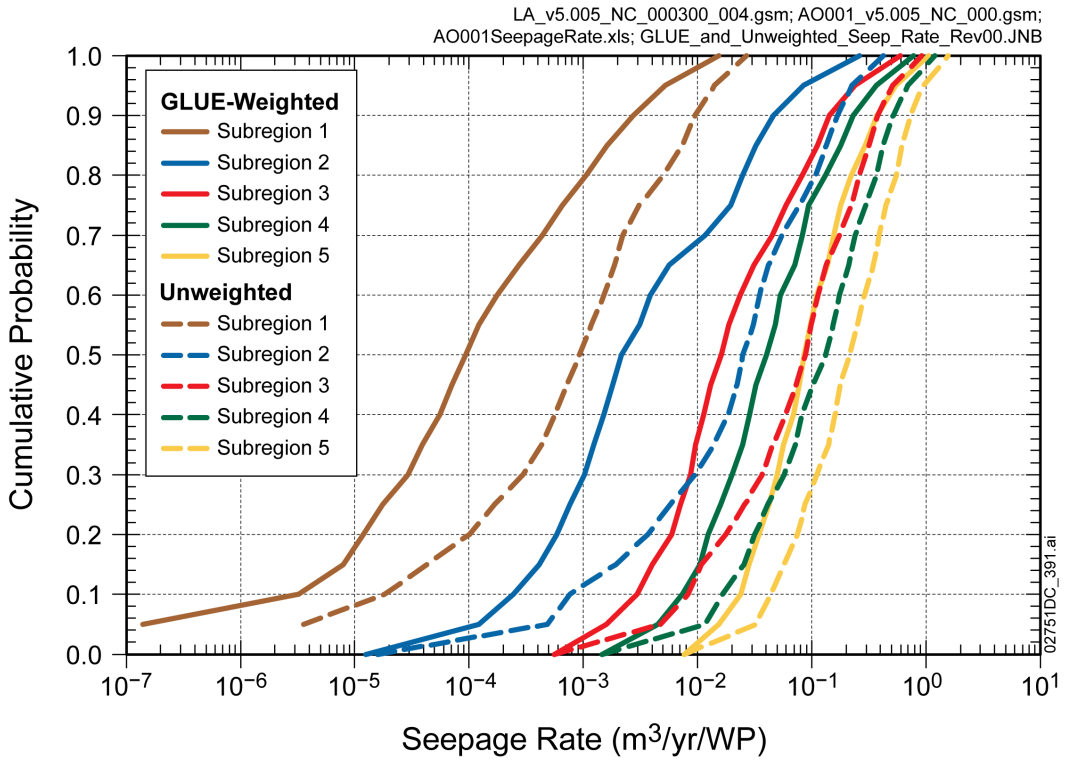

Figure 2. Comparison of the Cumulative Distribution Functions of the Average Seepage Rate per Commercial SNF Waste Package in the Five Percolation Subregions during the Glacial-Transition Climate for the GLUE-weighted and Unweighted Analyses

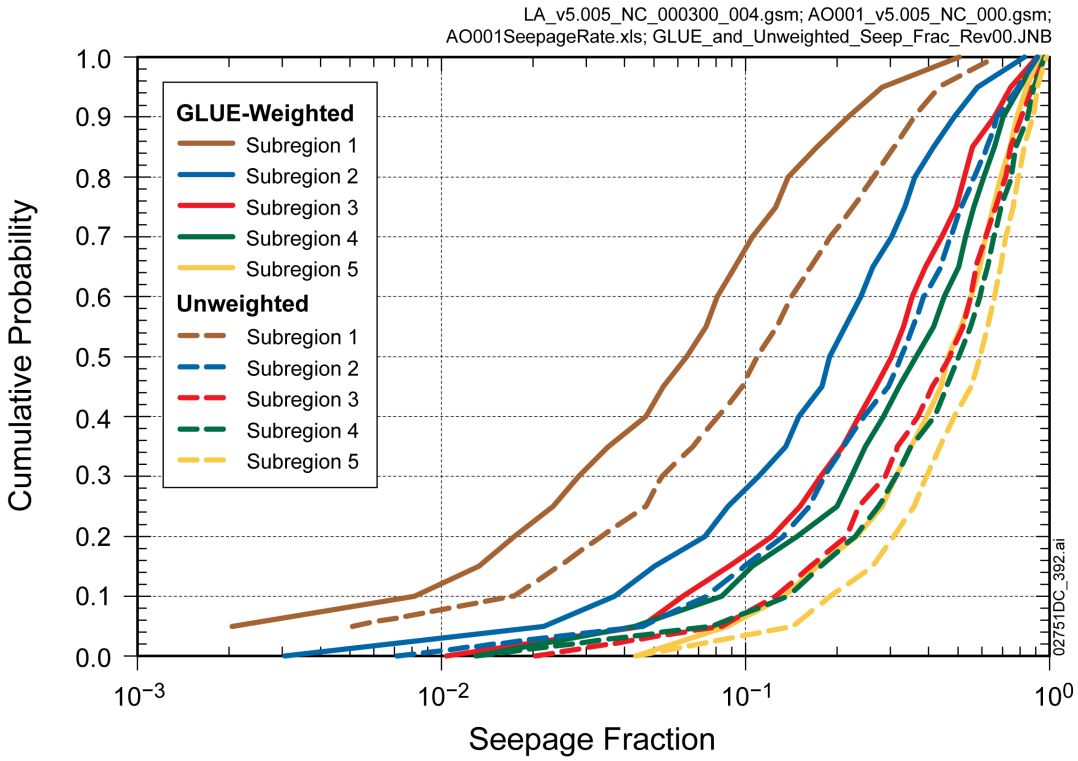

Figure 3. Comparison of the Cumulative Distribution Functions of the Seepage Fraction for Commercial SNF Waste Packages in the Five Percolation Subregions for the GLUE-weighted and Unweighted Analyses

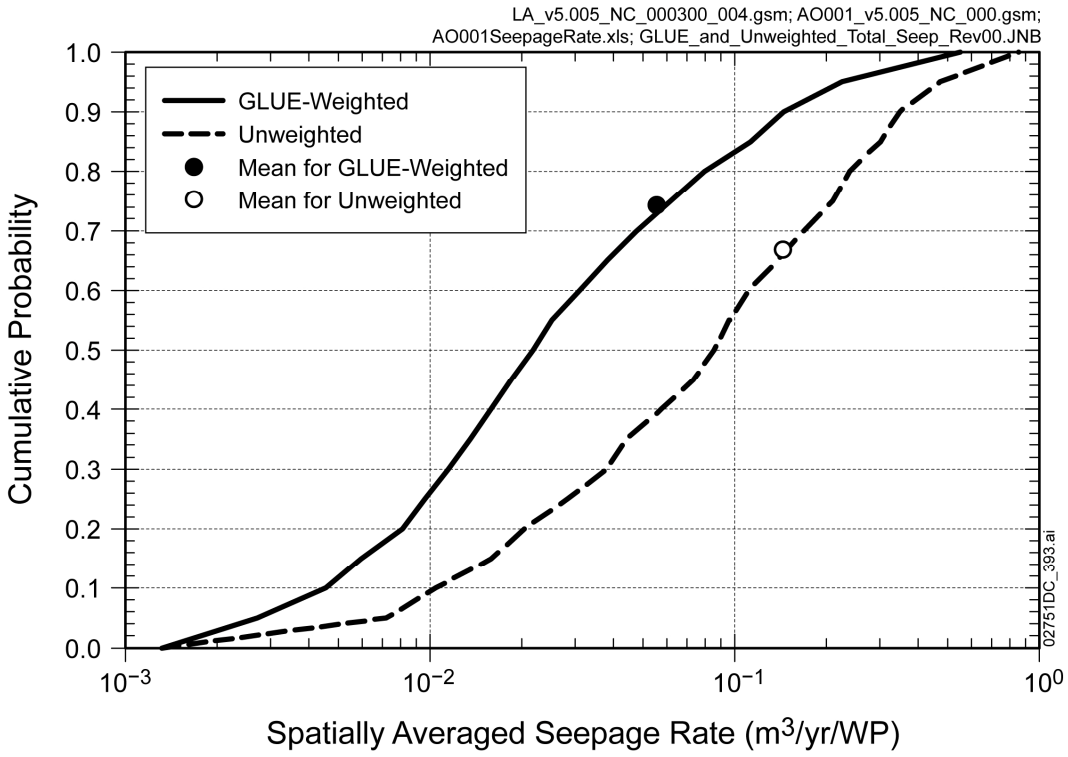

Figure 4. Comparison of the Cumulative Distribution Functions of the Repository Average Seepage Rate per Commercial SNF Waste Package during the Glacial-Transition Climate for the GLUE-weighted and Unweighted Analyses

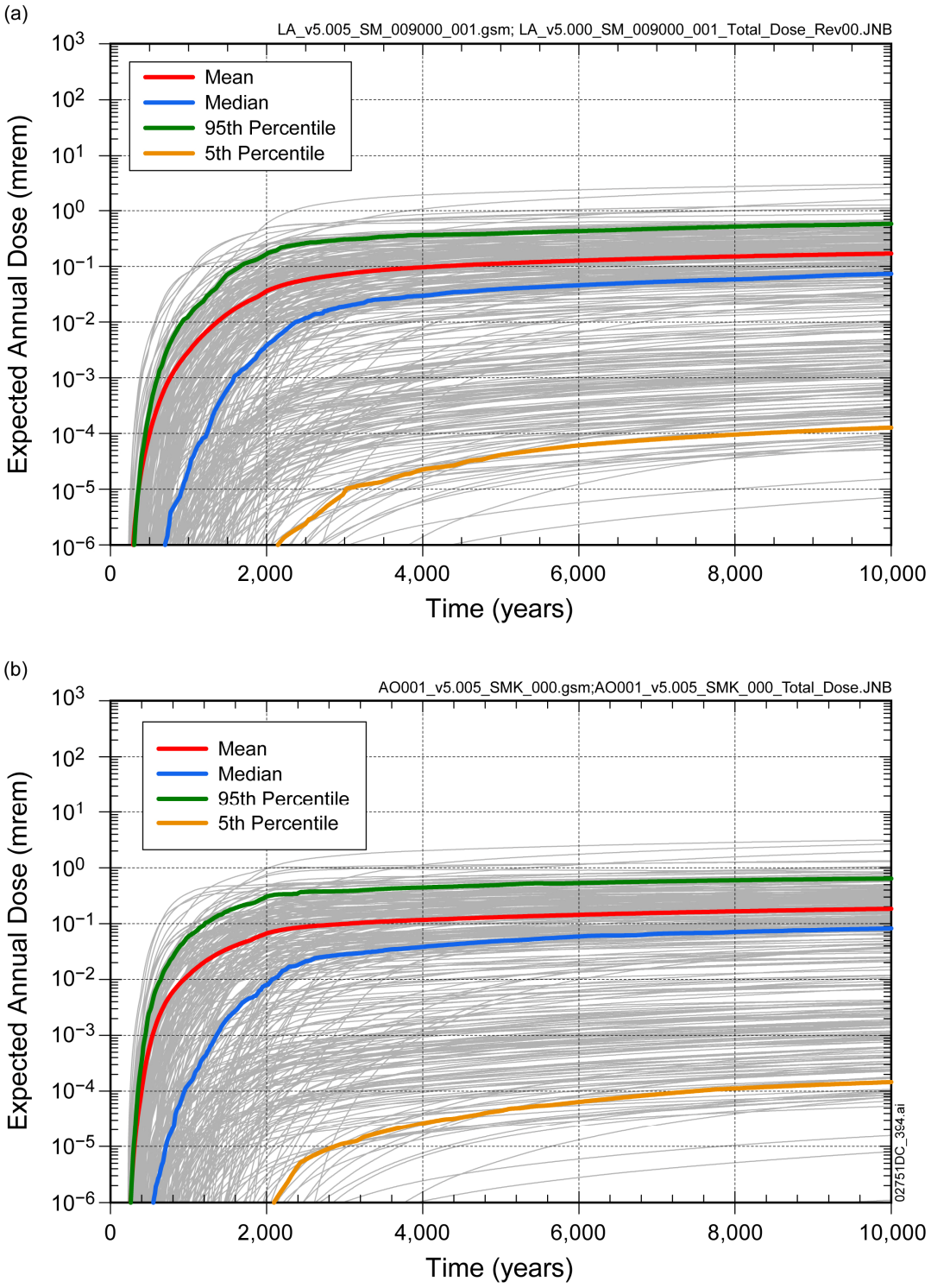

NOTE: Plot (a) is the same as Figure 8.2-11[a] in SNL 2008.

Figure 5. Expected Annual Dose from Seismic Ground Motion for 10,000 Years for (a) GLUE-weighted and (b) Unweighted Distribution for the *INFIL* Parameter

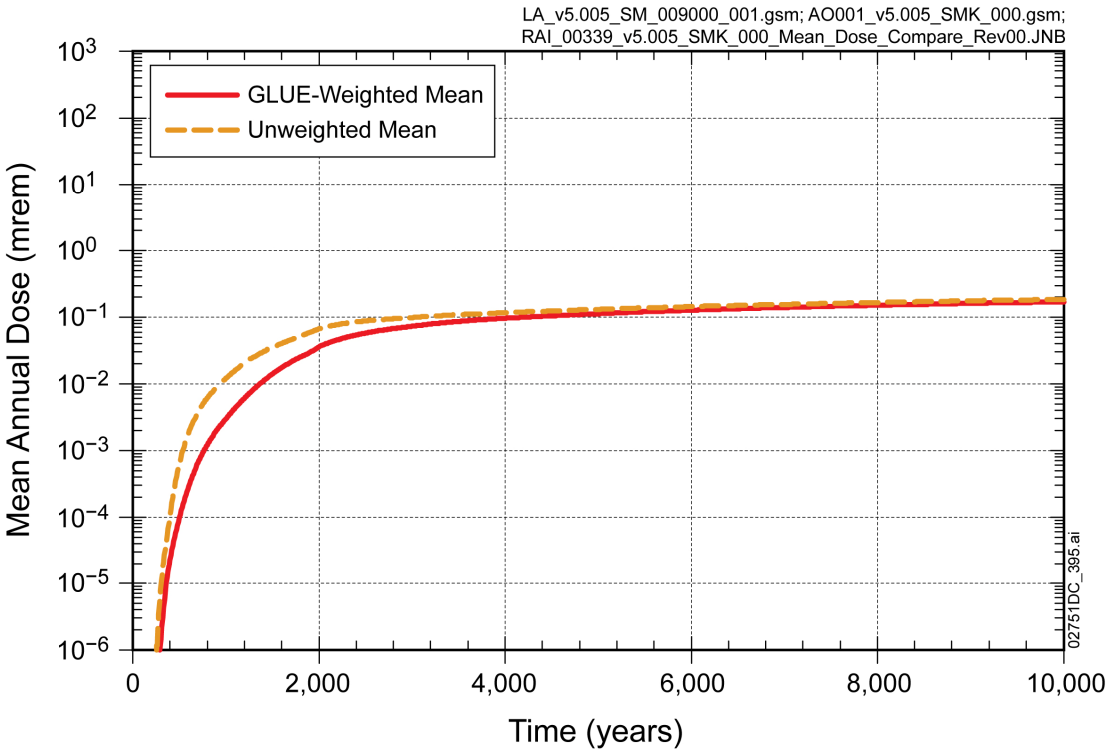

Figure 6. Comparison of Mean Annual Dose from the Seismic Ground Motion Modeling Case for GLUE-weighted and Unweighted Distribution for the *INFIL* Parameter

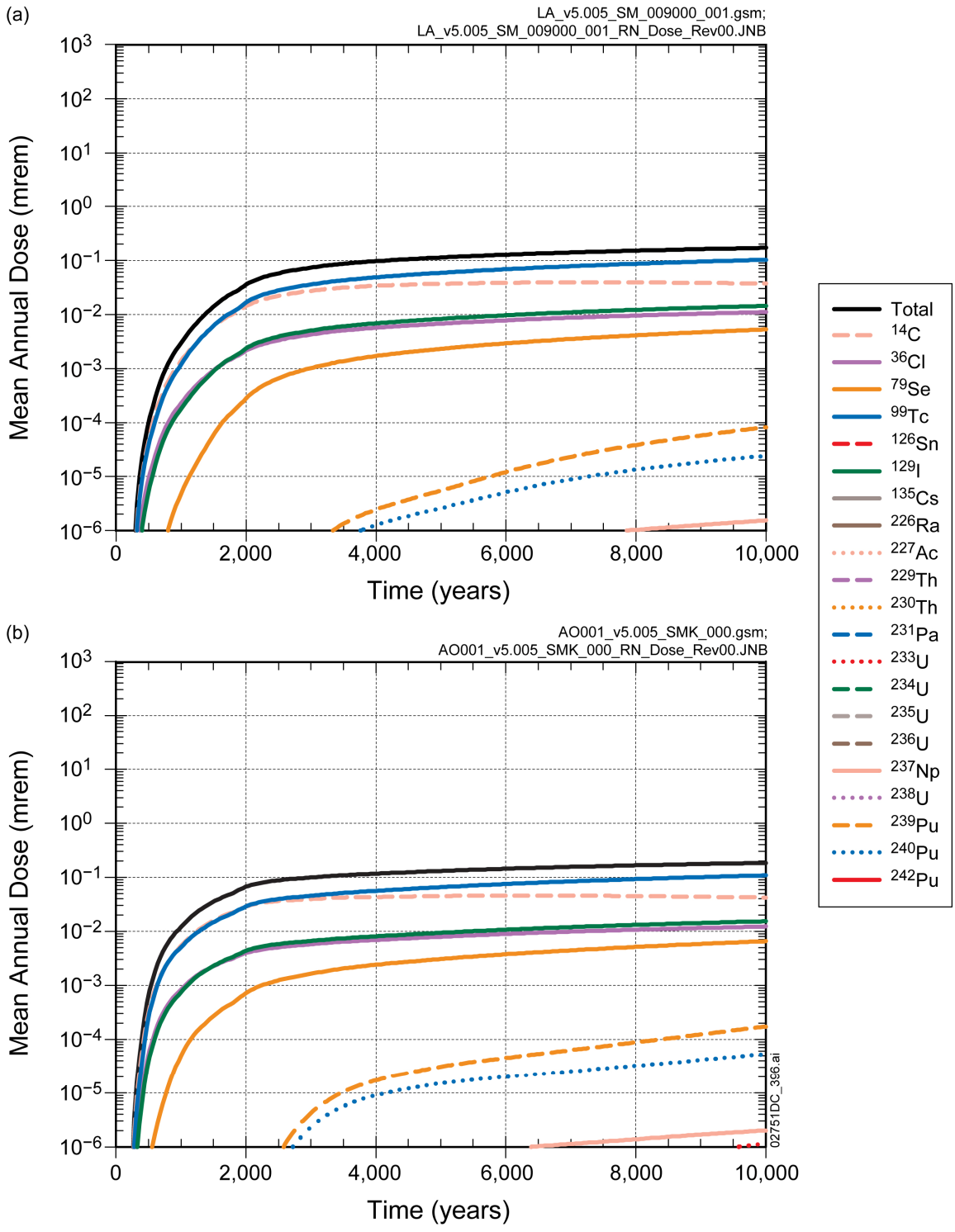

NOTE: Plot (a) is the same as Figure 8.2-12[a] in SNL 2008.

Figure 7. Contribution of Individual Radionuclides to Mean Annual Dose from Seismic Ground Motion for 10,000 Years for (a) GLUE-weighted and (b) Unweighted Distribution for the *INFIL* Parameter

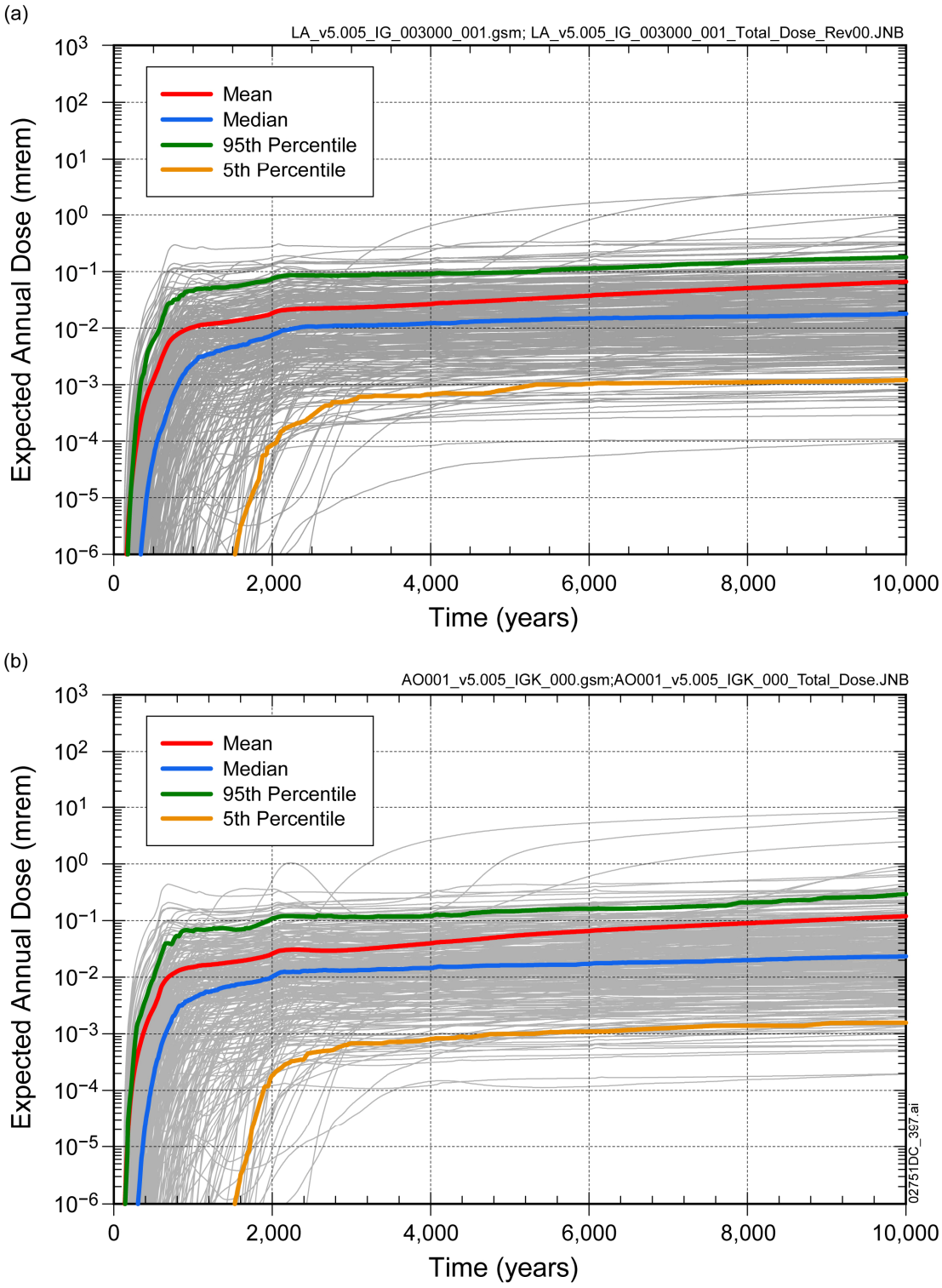

NOTE: Plot (a) is the same as Figure 8.2-7[a] in SNL 2008.

Figure 8. Expected Annual Dose from Igneous Intrusion for 10,000 Years for (a) GLUE-weighted and (b) Unweighted Distribution for the *INFIL* Parameter

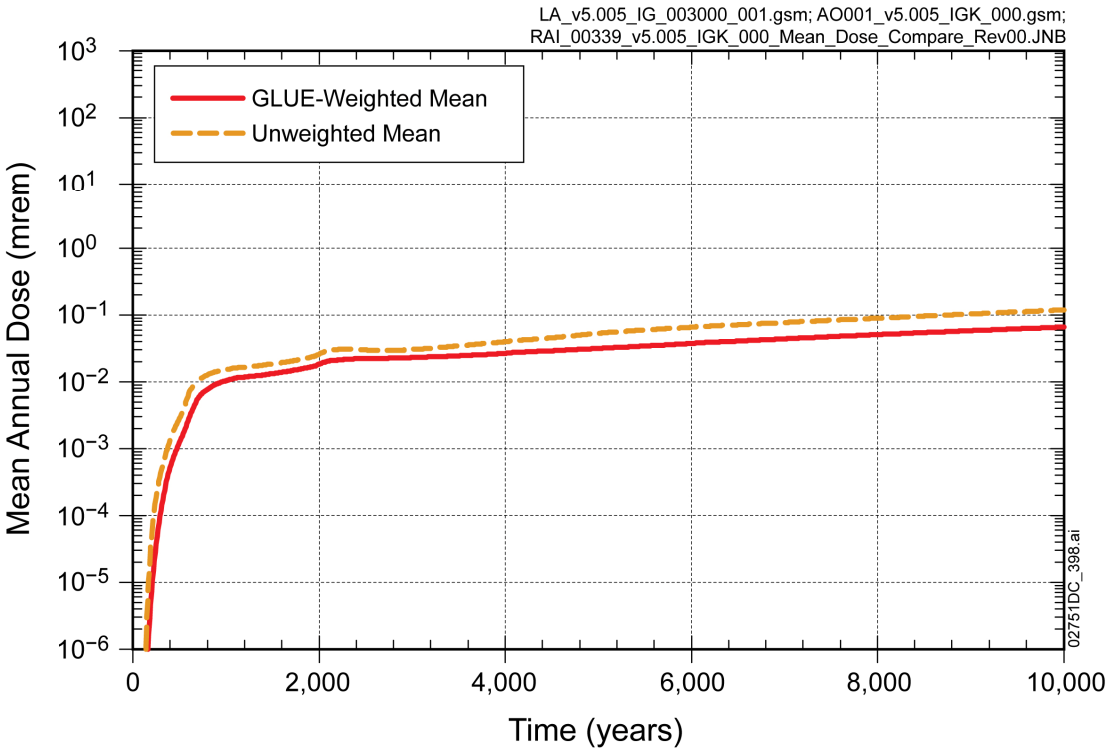

Figure 9. Comparison of Mean Annual Dose from the Igneous Intrusion Modeling Case for GLUE-weighted and Unweighted Distribution for the *INFIL* Parameter

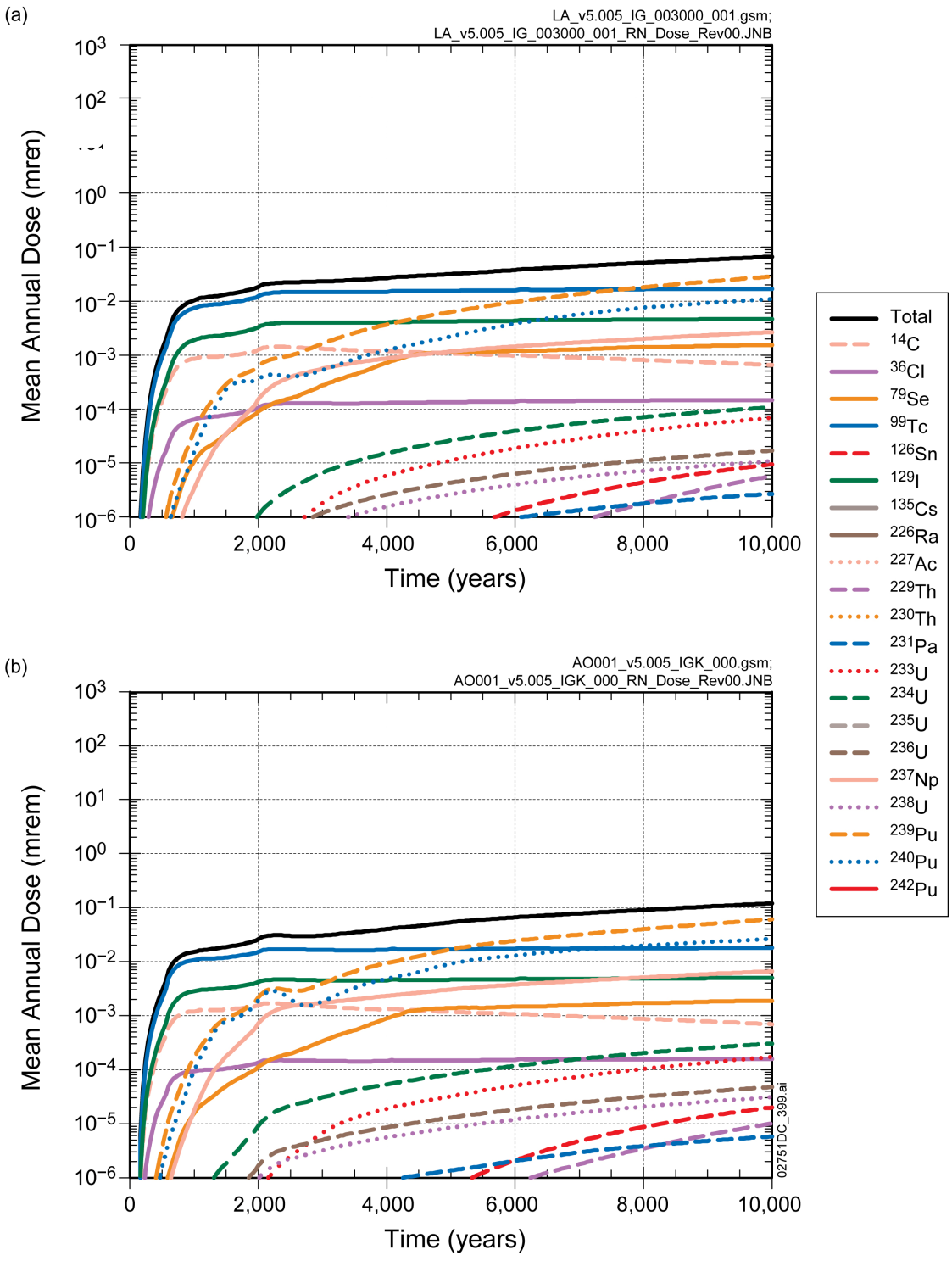

NOTE: Plot (a) is the same as Figure 8.2-8[a] in SNL 2008.

Figure 10. Contribution of Individual Radionuclides to Mean Annual Dose from Igneous Intrusion for 10,000 Years for (a) GLUE-weighted and (b) Unweighted Distribution for the *INFIL* Parameter

RAI Volume 3, Chapter 2.2.1.3.6, First Set, Number 8:

Explain (i) the procedure for selecting thermal observations used in the GLUE procedure and (ii) the procedure for verifying temperature boundary conditions. Explain why the Sass et al. (1988) borehole temperature profiles and thermal conductivity measurements are not used in the GLUE procedure. This information is needed to evaluate compliance with 10 CFR 63.114(a), (b), and (c).

Basis: The temperature observations used for the thermal model in the GLUE analysis (SAR Section 2.3.2.4.1.2.4.5.3) were drawn from long term monitoring at six boreholes and from observations by Sass, et al. (1988). NRC staff analysis suggests three factors in the DOE modeling of temperature data may lead to underestimates of percolation: (i) the water table temperature appears to be incorrectly interpolated, (ii) the top temperature boundary condition may be cooler than is consistent with borehole observations in some boreholes, and (iii) the thermal conductivity values below the TSw appear to be underestimated in several layers based on numerous observations by Sass et al. (1988). For example, temperature profiles in borehole SD-12 may be affected by underestimated thermal conductivity values in the Tptpv3, Tptpv1, Tpbt1, Tcpuv, Tcpuc, Tcplc, and Tcplv GFM2000 layers; these GFM2000 layers are included in the tsw38, ch1, and pp1 through pp4 unsaturated zone model layers. Further, the temperature boreholes used in the analysis are located in areas expected to have low infiltration, and the Sass et al. (1988) temperature profiles (which includes locations where infiltration is expected to be relatively large) were not considered in the GLUE procedure although apparently qualified by SNL (2007, Appendix I). Specific issues include:

- Water table temperatures shown in SAR figures 2.3.2-13 through 2.3.2-16 differ by between 1 and 2 °C from the temperatures that would be obtained by linear interpolation between the nearest boreholes with water table temperatures reported by Sass et al. (1988);

- Modeled temperatures are systematically cooler than the topmost observed temperature by approximately 0.5 °C in NRG-7 and UZ #5, approximately the difference between the modeled 10th and 50th percentile temperature profiles at the elevation of the lowest observed temperature; and

- Thermal conductivity parameter values used for model layers below the TSw are assigned estimates based on samples from other horizons. Thermal conductivity measurements by Sass et al. (1988) have larger values than those assigned in the model for layers below the TSw. Using smaller thermal conductivities low in a profile results in lower estimates of percolation.

1. RESPONSE

The thermal data and the water table and ground surface temperature boundary conditions used in the generalized likelihood uncertainty estimate (GLUE) and associated unsaturated zone thermal model were selected based on data accuracy and adequacy. The Sass et al. (1988) open borehole temperature profiles were not appropriate for use in the GLUE analysis because of insufficient data accuracy, but were sufficiently accurate for quantifying water table temperature used as a boundary condition in the unsaturated zone thermal model. The Sass et al. (1988) thermal conductivity measurements were not appropriate for use in the unsaturated zone thermal model because of inadequate characterization of thermal conductivity as a function of saturation. Small variations between surface temperatures, used as a boundary condition for the unsaturated zone thermal model, relative to shorter-term measurements at boreholes USW-NRG-7a and UE-25 UZ#5, are shown to be appropriate considering longer-term surface temperature data. Sections 1.1 and 1.2 provide information supporting the selection of temperature and thermal conductivity data, while Sections 1.3 and 1.4 provide information supporting the selection of water table and ground surface temperature boundary conditions.

1.1 TEMPERATURE DATA SELECTION

In situ temperature measurements in boreholes at Yucca Mountain were acquired principally through two field investigations. The first was conducted from 1980 to 1984 and is reported by Sass et al. (1988). Temperature profiles were measured in 35 boreholes within the central block of Yucca Mountain and in the surrounding area (Sass et al. 1988) as part of a regional heat flow study. This data set includes temperature measurements above and below the water table in many of the boreholes. The second field investigation was conducted from 1994 to 1998. Temperature was monitored at stations located in six boreholes, within the unsaturated zone only (SAR Sections 2.3.2.3.2.3 and 2.3.2.4.1.2.4.5.3). No measurements at or below the water table were taken from these six boreholes.

1.1.1 First Field Investigation for Temperature in the Unsaturated Zone

For the first investigation, measurements were conducted in open boreholes using thermistors that were lowered into water-filled or air-filled tubing which had been installed in the boreholes. As described by Sass et al. (1988, pp. 83 to 85), the most serious problem encountered with this method was disturbance caused by convective air movement within the borehole. A 1°C variation in temperature is large relative to some of the changes in temperature profiles as a result of changes in infiltration rate. The air movement was caused by thermal instabilities and diurnal barometric pressure variations. Maximum temperature variations caused by the air movement were estimated by Sass et al. (1988, p. 84) to be on the order of 1°C or more. Only a few of the boreholes have repeated temperature measurements which can be used to evaluate the stability of the temperature measurements. Figures 1 and 2 show temperature profiles for two boreholes with repeated measurements (USW G-1 and USW G-2). The variations in unsaturated zone temperature at different times, as shown in these figures, are consistent with the effect of convective air movement in open boreholes. These profiles also show better temperature stability lower in the borehole than near the surface.

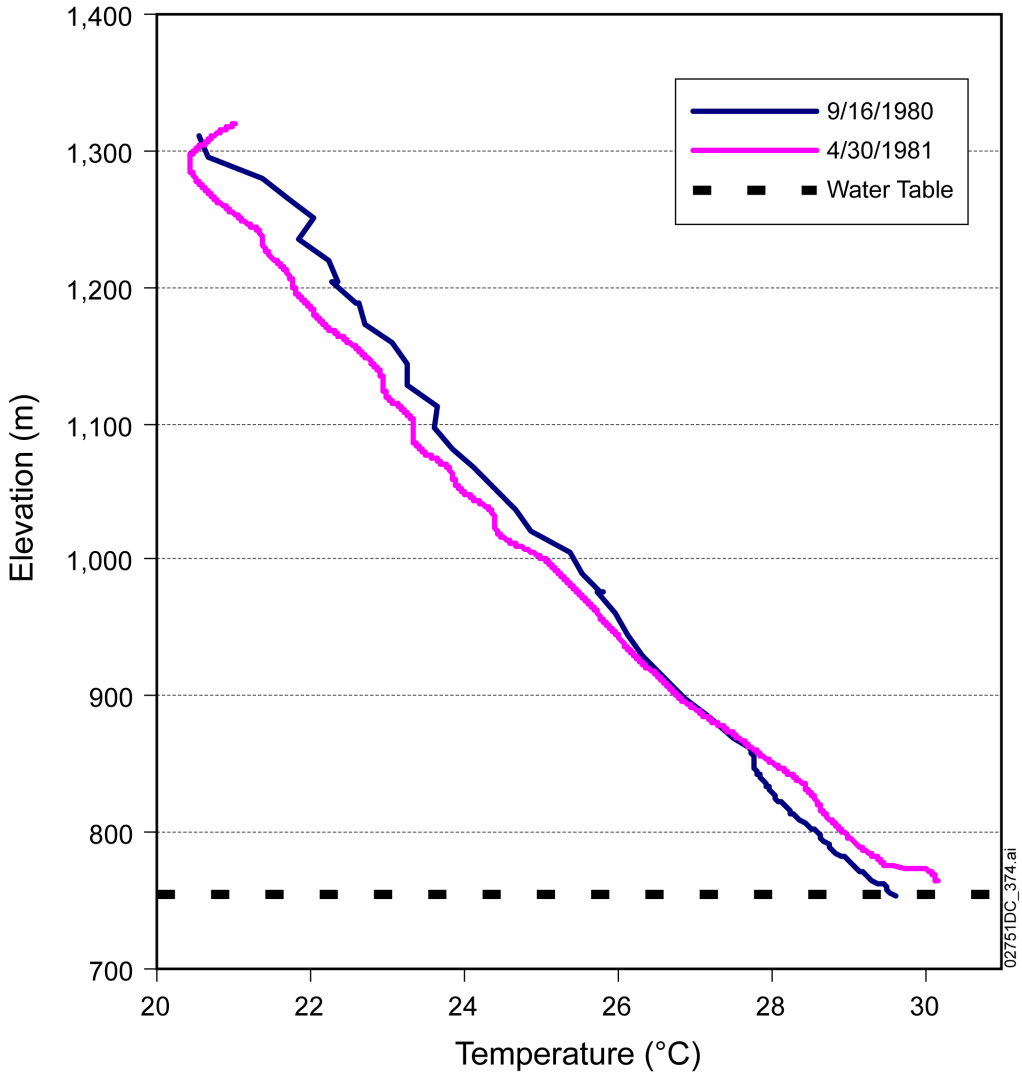

Figure 1. Temperature Profile at USW G-1

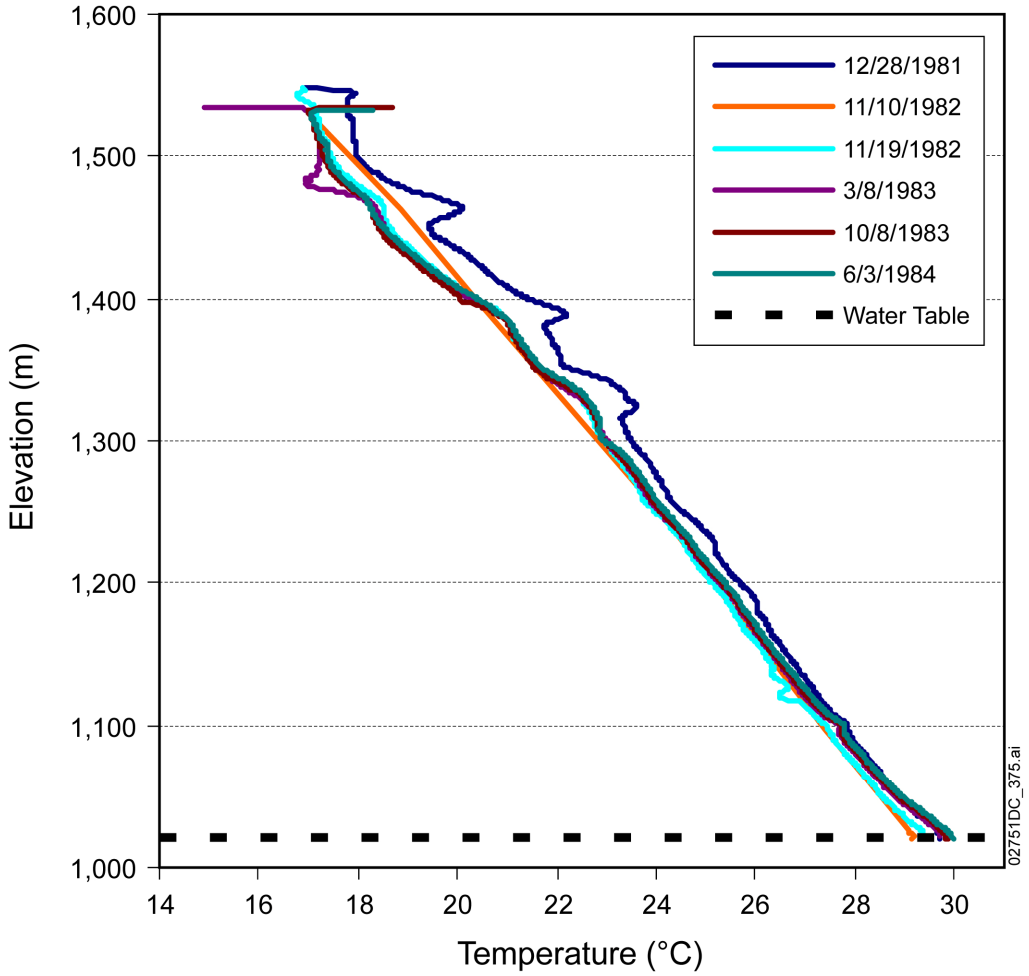

Figure 2. Temperature Profile at USW G-2

1.1.2 Second Field Investigation for Temperature in the Unsaturated Zone

The second field investigation used a different instrumentation approach (SAR Section 2.3.2.3.2.3). For these measurements, temperature sensors were installed in stemmed boreholes. At each instrument station, the borehole was packed with polyethylene beads and then capped with silica sand. Intervals between the instrument stations were filled with an expansive calcium-sulfate grout. This method isolated the stations from the atmosphere and eliminated strong convective air movement within the borehole. Repeated measurements were made from 1995 to 1998 at all stations, and examples are presented below for boreholes USW SD-12 and UE-25 UZ#5 (Figures 3 and 4). In addition to the temperature measurements, the aggregated values used in the GLUE analysis are also shown on Figures 3 and 4. Temperature measurements from the second field investigation have superior temperature stability relative to those acquired from open (unstemmed) boreholes in the first field investigation. A 1°C variation in temperature is large relative to some of the changes in temperature profiles as a result of changes in infiltration rate.

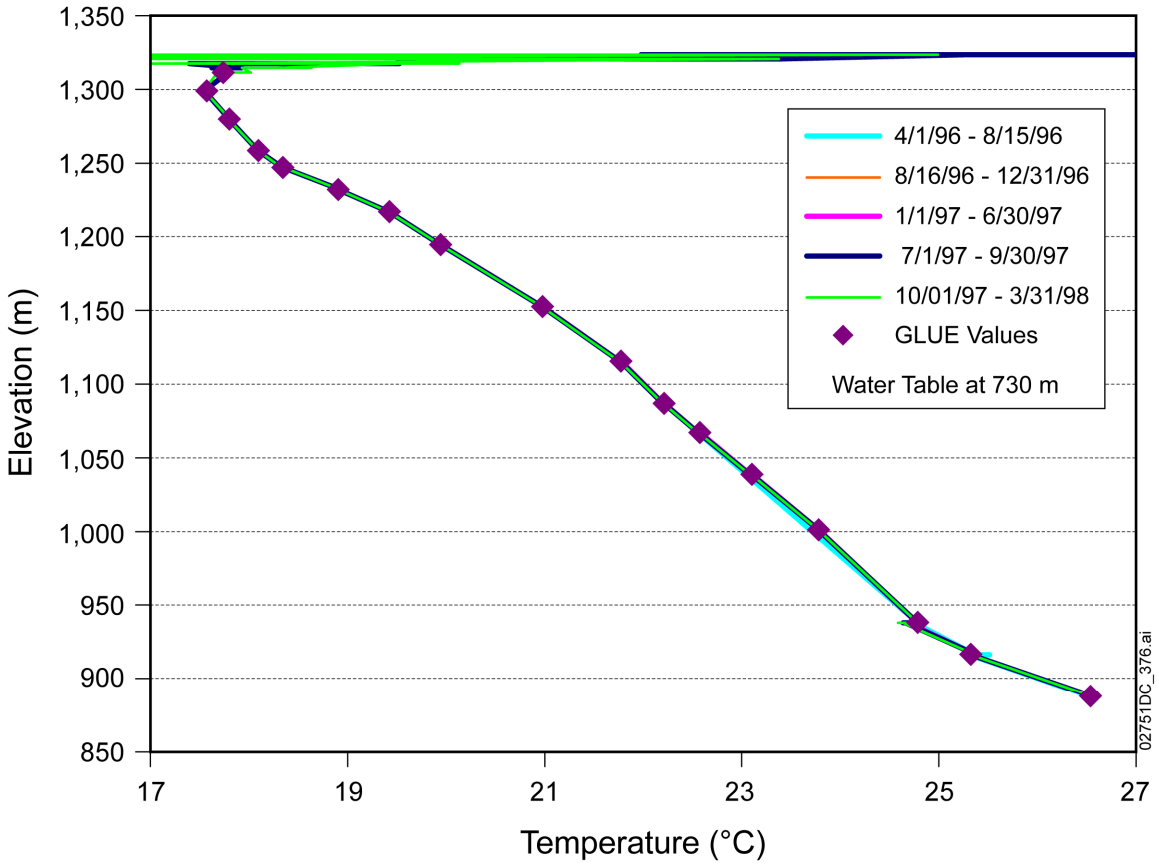

Figure 3. Temperature Profile at USW SD-12

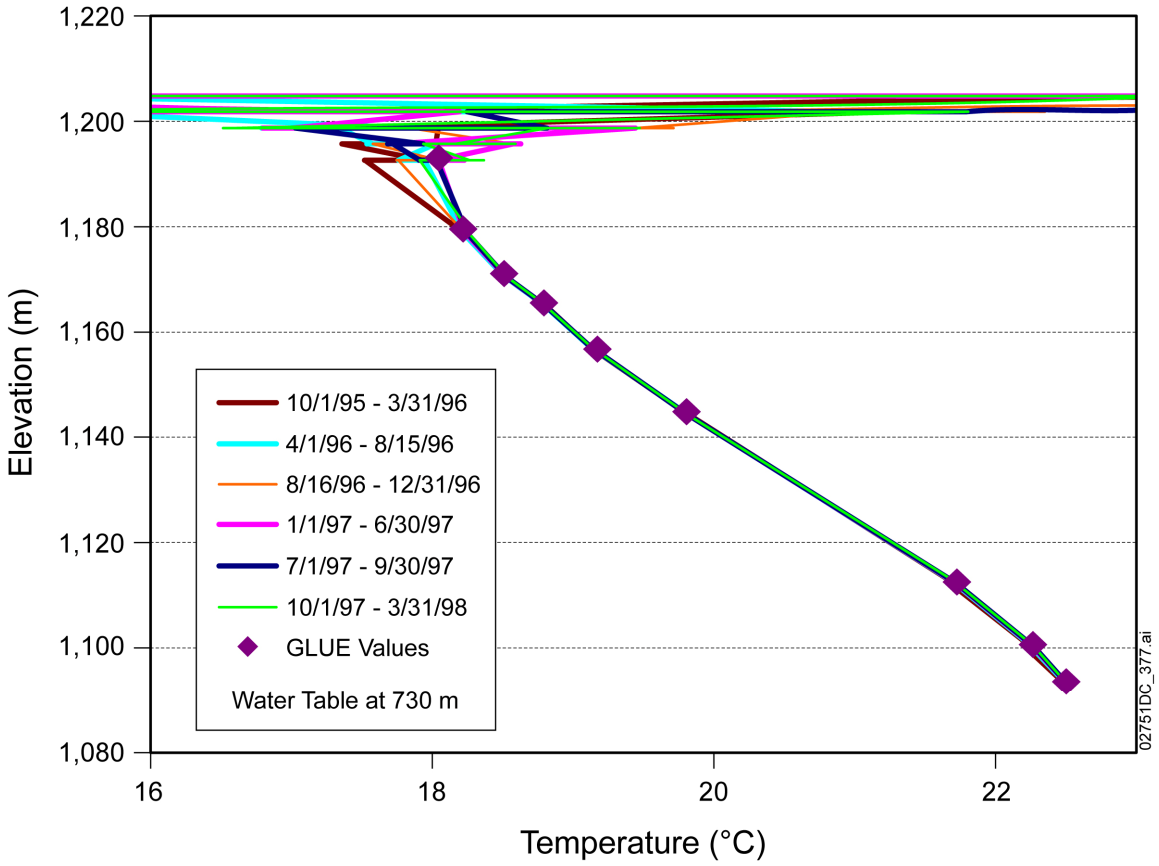

Figure 4. Temperature Profile at UE-25 UZ#5

Note that these profiles exhibit periodic temperature fluctuation near the ground surface. This is caused by penetration of surface temperature variations into the unsaturated zone. These variations are substantially damped out at depths greater than about 20 meters.

Of the six boreholes instrumented in the second field investigation, five were used for the analysis of infiltration uncertainty in the GLUE analysis. Boreholes UZ#4 and UZ#5 are so close to each other that they fall into the same unsaturated zone model grid column (SNL 2007, Section 6.3.4). Temperatures in UE-25 UZ#4 are affected by a thick layer of alluvium on the order of 10 m (SAR Section 2.3.2.4.1.2.4.5.3), which is not included in the unsaturated zone model. This affects the near-surface temperatures, while deeper temperatures are similar to UZ#5. Therefore, UE-25 UZ#4 was not used for the calibrations.

1.1.3 Use of the First Field Investigation Data to Establish Water Table Temperatures

The data from the first field investigation were only qualified for use in the thermal analysis as the lower temperature boundary condition. There are two reasons for limiting the use of these data for this purpose. First, water table temperature measurements from the first field investigation are the best available. Second, the temperature measurements from the second field investigation lie mostly in the upper half of the unsaturated zone. With the exception of USW SD-12, these measurements are at least 300 to 400 m above the water table. For USW SD-12, the

lowest temperature measurements are about 150 m above the water table. Because these measurements are relatively remote from the water table, there is reduced sensitivity to uncertainty in water table temperature for thermal-hydrologic analysis. This reduced sensitivity allows for the use of the less stable temperature measurements from the first field investigation for water table temperatures.

1.1.4 Summary of the Rationale for Temperature Data Selection

Temperature profiles from the second field investigation are used in the GLUE analysis, rather than profiles from the first field investigation, because of the greater stability and reduced measurement uncertainty. However, the temperature measurements from the second field investigation do not provide temperatures at or near the water table that are needed for the water table boundary condition. The first field investigation provides the best available temperature measurements at or near the water table. There is less sensitivity in the GLUE analysis to water table temperature than to the unsaturated zone temperature profiles. Accordingly, temperature measurements from the first field investigation were qualified for use in developing the water table temperature boundary condition used by the unsaturated zone thermal analysis.

1.2 PARAMETERIZATION OF THERMAL CONDUCTIVITY

Rock thermal conductivity was measured as part of the first field investigation of *in situ* temperature and regional heat flow described in Section 1.1 (Sass et al. 1988). A second set of measurements was conducted and these are the values used for thermal analyses documented in *UZ Flow Models and Submodels* (SNL 2007, Section 6.3.4). The Sass et al. (1988) thermal conductivity data were found to be unsuitable because of limitations in the sampling and measurements.

1.2.1 Thermal Conductivity Data from Sass et al. 1988

Thermal conductivity measurements are briefly described by Sass et al. (1988, Appendix 3). Measurements were conducted on core samples from boreholes USW G-1, USW G-2, USW G-3/GU-3, and USW G-4. A total of 191 measurements are reported, but 57 of these are from rock units that are stratigraphically below those included in the unsaturated zone model.

Notably, the core samples were drilled with polymer drilling fluids and then preserved in aluminum foil and wax. Thermal conductivities were measured using the needle probe method at the preserved, but unknown, saturation conditions. The use of a polymer drilling mud during coring operations for these boreholes means that permeable core samples were likely invaded by the drilling mud; low permeability samples would be less affected. However, the general trends for water saturation in the unsaturated zone lead to relatively low *in situ* saturation in more permeable rock and relatively high saturation in less permeable rock. Because the unsaturated zone model layers are tilted relative to the horizontal, a model unit that appears in the unsaturated zone at one location may be in the saturated zone at another location. In the Sass et al. (1988, Appendix 3) data set, 77 of the 134 samples applicable to unsaturated zone model units were taken from boreholes where these units are below the water table. The net effect of these conditions is that the thermal conductivity measurements reported by Sass et al. (1988,

Appendix 3) were probably made at high liquid saturation of an unknown mixture of water and drilling mud.

1.2.2 Baseline Thermal Conductivity Data from Sandia National Laboratories Measurements

The baseline thermal conductivities were measured on cores from boreholes USW SD-7, USW SD-9, USW SD-12, UE-25 NRG#4, UE-25 NRG#5, USW NRG-6, and USW NRG-7a. The measurements were taken on samples with known water saturation using the guarded heat flow meter method. This measurement program provided wet and dry thermal conductivity values, which are needed for thermal models of variably saturated rock. Comparisons of the baseline thermal conductivity data with the Sass et al. (1988) data are presented in Sections 1.2.3 and 1.2.4 for completeness but are of limited value because of the limitations of the Sass et al. (1988) data as described in Section 1.2.1.

1.2.3 Comparison of Thermal Conductivity Values

Table 1 presents a comparison of thermal conductivity values from Sass et al. (1988, Appendix 3) and the baseline "wet" values by unsaturated zone model layer, in Watts/meter-Kelvin (W/m-K).

Table 1. Unsaturated Zone Thermal Conductivity Comparsion

Unsaturated Zone Model Layer	Baseline Wet Thermal Conductivity (W/m-K)	Sass et al. 1988 Thermal Conductivity (W/m-K)	Percent Difference (%)
tcw11	1.80	1.96	8
tcw12	1.80	2.05	13
tcw13*	0.79	1.42	78
ptn21**	1.07	0.79	−26
ptn22**	1.07	0.79	−26
ptn23**	1.07	0.79	−26
ptn24	1.07	0.79	−26
ptn25	1.07	1.19	12
ptn26	0.96	0.97	1
tsw31	0.79	1.33	67
tsw32	1.80	1.55	−14
tsw33	1.91	2.04	7
tsw34	2.13	2.19	3
tsw35	2.07	2.02	−2
tsw36	2.20	2.33	6
tsw37***	2.20	2.33	6
tsw38	0.79	1.26	59

Table 1. Unsaturated Zone Thermal Conductivity Comparsion (Continued)

Unsaturated Zone Model Layer	Baseline Wet Thermal Conductivity (W/m-K)	Sass et al. 1988 Thermal Conductivity (W/m-K)	Percent Difference (%)
tsw39	0.79	1.08	36
ch1	1.07	1.06	−1
ch2-5	1.27	1.14	−10
ch6	1.27	1.37	8
pp4	1.11	1.28	15
pp3	1.11	2.01	81
pp2	1.34	1.72	28
pp1	1.13	1.34	18
bf3	1.33	1.80	35
bf2	1.14	1.40	23
tr3	1.23	1.86	52
tr2	1.08	1.65	54

* Sass et al. (1988) value estimated as average of values from tcw12 and ptn24.

** Sass et al. (1988) value estimated as equal to value for ptn24.

*** Sass et al. (1988) value estimated as equal to value for tsw36.

Although there is a definite trend to higher values in the Sass et al. (1988) data for the Prow Pass, Bullfrog, and Tram units (pp4 through tr2), exposure of the Bullfrog and Tram units in the unsaturated zone is relatively limited, and these units are below the water table at all of the temperature boreholes used for the GLUE analysis. The water table at UE-25 UZ#5 lies in the ch4 unit, the water table at boreholes USW NRG-6 and USW NRG-7a is in the ch5 unit, and the water table at boreholes USW SD-12 and USW UZ-7a is in the pp1 unit. Significantly larger pp3 unit thermal conductivity measurements for the Sass et al. (1988) data are a result of two measurements having values of 1.5 and 2.5 W/m-K. Given these large variations from two measurements, the uncertainty in the mean value for the pp3 is also large. Larger discrepancies are also found in the tcw13, tsw31, tsw38, and tsw39 units, but these are generally thin units. On the other hand, measurements in the main part of the Calico Hills hydrogeologic unit (ch2 through ch5 units) by Sass et al. (1988) provide an average value that is in reasonable agreement with the baseline value.

1.2.4 Comparison of Temperature Predictions Using Baseline and Sass et al. (1988) Thermal Conductivities

An analytical temperature model (Bodvarsson et al. 2003) is used to evaluate sensitivity to the variations in thermal conductivity. The analytical model is for a multilayer, one-dimensional, single continuum that is characterized by layer-wise variations in thermal convective diffusivity, defined as the rock thermal conductivity divided by the product of the density and specific heat for water. Temperature calculations are performed for the stratigraphy at borehole USW SD-12.

Thermal conductivity as a function of water saturation is defined using the baseline wet and dry thermal conductivities as follows:

$$\lambda(S) = \lambda_{dry} + (\lambda_{wet} - \lambda_{dry})\sqrt{S} \quad \text{(Eq. 1)}$$

where $\lambda(S)$ is the thermal conductivity at saturation S, and λ_{wet} and λ_{dry} are the wet and dry thermal conductivities.

The thermal conductivities reported by Sass et al. (1988) were used as alternative wet thermal conductivities, $\lambda_{alt\,wet}$. Thermal conductivities at intermediate saturations, λ_{alt}, were computed using the following equation:

$$\lambda_{alt}(S) = \frac{\lambda_{alt\,wet}}{\lambda_{wet}}\lambda(S) \quad \text{(Eq. 2)}$$

The water saturations at USW SD-12 were taken from the three-dimensional version of the unsaturated zone flow model, used in the GLUE analysis. The infiltration rates for the 10th, 30th, 50th, and 90th percentile present-day infiltration maps are taken from Table 6-3 of *Calibrated Unsaturated Zone Properties* (SNL 2007).

The calculation results are shown in Figures 5(a) to 5(d) for each infiltration scenario.

The results show that the variations in temperature caused by the alternative thermal conductivity values are generally smaller than the variations in temperature caused by the infiltration scenarios (Figures 7 through 11). Therefore, uncertainties in thermal conductivity represented by differences between the baseline and the alternative thermal conductivity values have a relatively small effect on temperature predictions. Note that boreholes with narrow variations in computed temperatures for the different infiltration scenarios (UE-25 UZ#5, USW NRG-6, and USW NRG-7a) have water table elevations in the ch4 or ch5 units and, therefore, are insensitive to the larger variations in thermal conductivities in the pp3 and pp2 units.

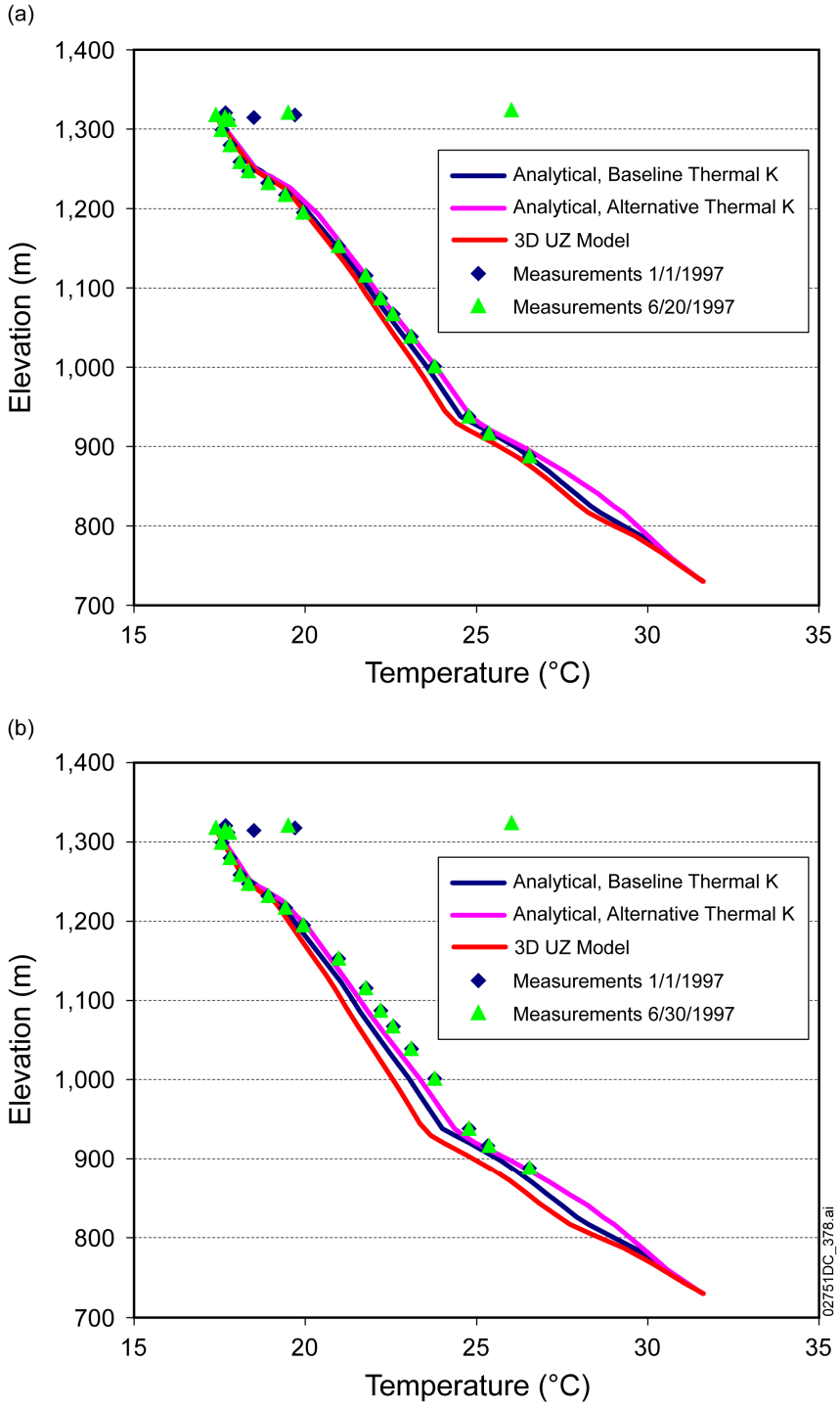

NOTE: 3D = three-dimensional; UZ = unsaturated zone.

Figure 5. Temperature Model Results at USW SD-12 Using the One-Dimensional Analytical Model with Baseline and Alternative Thermal Conductivities and the Three-Dimensional Numerical Model Using the Baseline Thermal Conductivities: (a) 10th Percentile Infiltration Scenario, and (b) 30th Percentile Infiltration Scenario

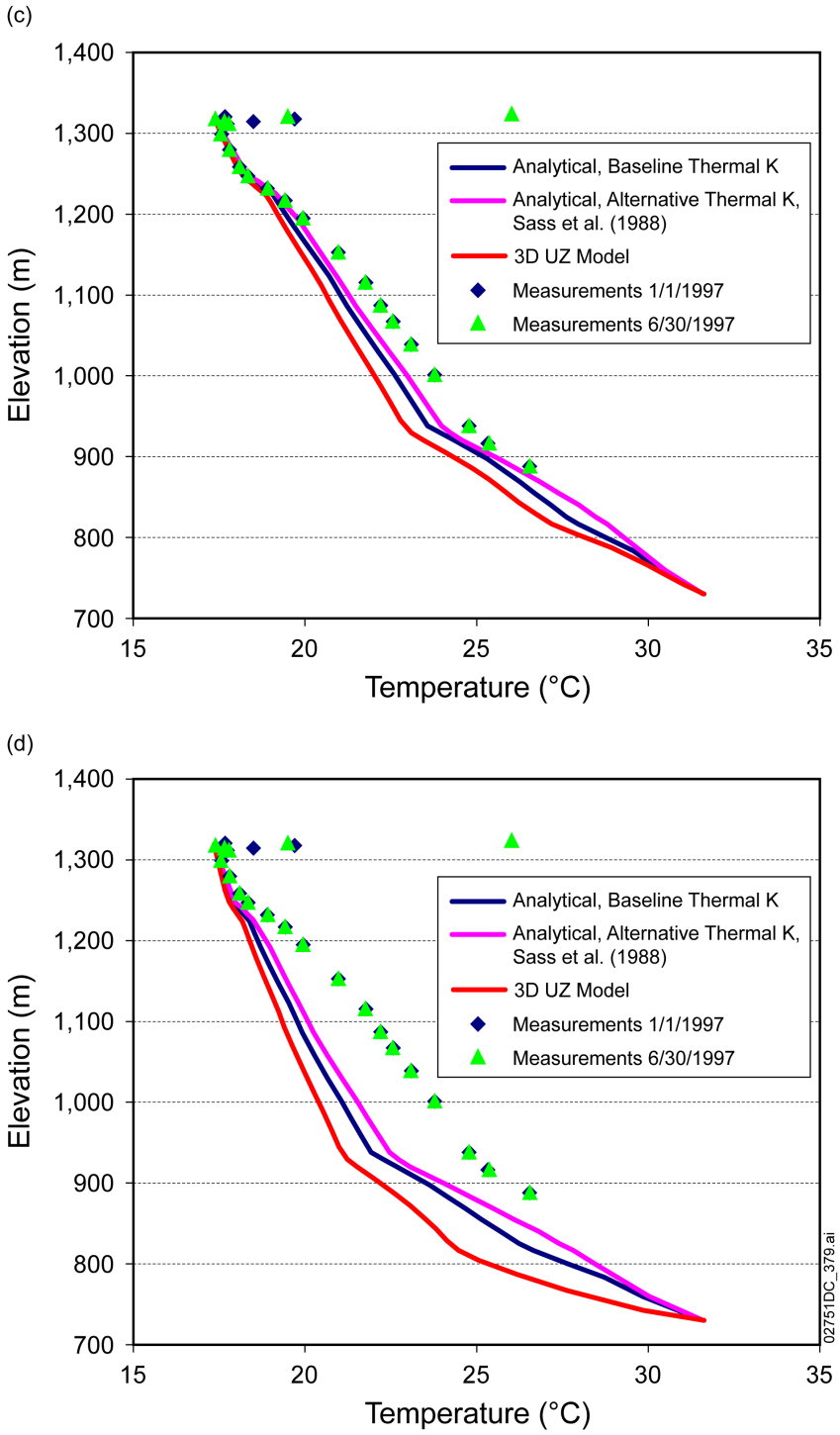

NOTE: 3D = three-dimensional; UZ = unsaturated zone.

Figure 5. Temperature Model Results at USW SD-12 Using the One-Dimensional Analytical Model with Baseline and Alternative Thermal Conductivities and the Three-Dimensional Numerical Model Using the Baseline Thermal Conductivities: (c) 50th Percentile Infiltration Scenario, and (d) 90th Percentile Infiltration Scenario (continued)

1.3 WATER TABLE TEMPERATURES

Water table temperatures are needed as a boundary condition for the unsaturated zone thermal model used for the GLUE analysis of infiltration weighting factors (SNL 2007, Section 6.3.2). In the original development of the water table temperature map, water table temperatures over the ambient thermal model domain were first interpolated from the measured values of temperature in numerous boreholes. For cases where the borehole temperature measurements did not extend down to 730 m, temperatures at this elevation were estimated by linear extrapolation. Water table temperatures were then calibrated such that the predicted temperatures provided a best fit to the qualified temperature measurements in the boreholes with qualified temperature data (NRG-6, NRG-7a, SD-12 UZ#4, UZ#5, and UZ-7a). This calibration step was performed using a present-day mean infiltration map from the infiltration model (INFIL) as discussed in *UZ Flow Models and Submodels* (SNL 2007, ERD 04). This water table temperature map is called the baseline calibrated case. The thermal model analysis for the unsaturated zone was then used in combination with an analysis of pore-water chloride to determine weighting factors for infiltration uncertainty scenarios used in the total system performance assessment for license application (TSPA-LA) (SNL 2007, Section 6.8). However, the ambient thermal model is used as an independent method to assess infiltration rates. Therefore, the water table temperature boundary condition used for these thermal analyses should be developed from water table measurements only, without any calibration that relies on infiltration rates.

For a sensitivity study documented in *UZ Flow Models and Submodels* (SNL 2007), water table temperatures are interpolated directly from the water table measurements without calibration to model results. The revised water table temperature map, called the uncalibrated sensitivity case, is then used as a boundary condition for the ambient thermal model. The revised temperature results are used to compute revised infiltration weighting factors, which are compared to the infiltration weighting factors used for the TSPA-LA (SNL 2007, Section 6.8).

1.3.1 Revised Water Table Temperature Map

The water table temperatures used in the ambient thermal model have been analyzed using the temperature data from 34 of the boreholes included in the data from Sass et al. (1988) and temperature profiles from six boreholes from the second investigation discussed above (SAR Section 2.3.2.3.2.3). Thus, temperature data were compiled for 40 borehole locations, while water table elevation data were available for 85 borehole locations. Water table elevation and temperature data exist for 28 of these boreholes, with temperature data above and below the water table in 26 out of the 28. At one borehole (UE-25 WT #18), the temperature measurements came to within 17 feet of the water table. For this borehole, the water table temperature is extrapolated and included in the set of measured water table temperatures. This gives a total of 27 water table temperature measurements.

The temperature data are given as a function of borehole depth. Therefore, water table elevations were converted to depth at each borehole using the ground elevation. The temperature data from approximately 600 feet below the surface to the water table were plotted as a function of depth for each borehole and a curve fit through these data was computed. The functional form of the curve fit was a second order polynomial. The curve fit was then used to estimate the water table

temperature for the borehole using the depth to the water table. This gave the basic water table temperature data at the measurement boreholes to be used for establishing temperatures at the lower boundary of the ambient temperature numerical model.

Water table temperatures were interpolated over the domain of the ambient thermal model at the nodal points of the bottom boundary of the numerical grid. This interpolation was performed using the geostatistical kriging methodology. The revised water table temperature map is shown in Figure 6. The temperature boreholes in this figure are the boreholes used for temperature profiles in the GLUE analyses. The water table temperature boreholes are a subset of the boreholes documented by Sass et al. (1988) used for estimating water table temperatures for the unsaturated zone thermal model. The remaining boreholes used for estimating water table temperatures lie outside the domain of the unsaturated zone thermal model. The changes in water table temperature boundary conditions for the baseline calibrated case and uncalibrated sensitivity case are shown in Table 2. Temperatures at the water table for these boreholes averaged 0.7°C higher for the sensitivity case than the baseline case.

Table 2. Water Table Temperatures Used for Thermal Boreholes

Borehole	Baseline Calibrated Water Table Temperature (°C)	Uncalibrated Sensitivity Analysis Water Table Temperature (°C)
USW NRG-6	31.8	30.6
USW NRG-7A	30.8	31.0
UE-25 UZ#5	30.0	31.2
USW SD-12	30.3	31.6
UE-25 UZ-7A	29.3	31.4

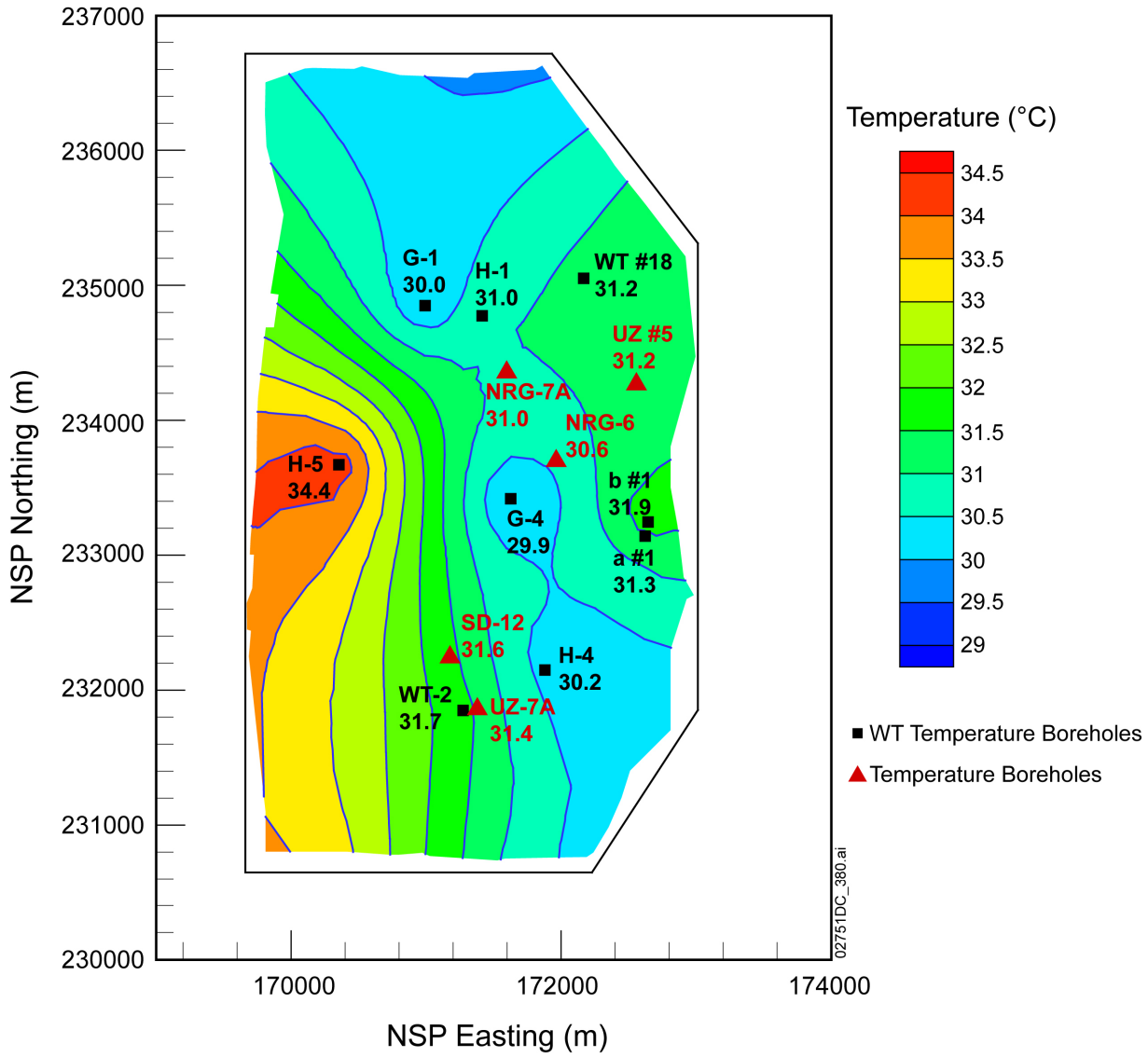

Figure 6. Water Table Temperature Contour Plot

1.3.2 Evaluation of Impacts from Revised Water Table Temperature Map

Using the interpolated, uncalibrated temperatures at the water table described in Section 1.3.1, the analyses of temperature in the unsaturated zone as described in *UZ Flow Models and Submodels* (SNL 2007, Section 6.3) were repeated. The temperature profiles from these analyses are shown as Figures 7 to 11. These figures were compared with Figures 6.3-2 to 6.3-6 of *UZ Flow Models and Submodels* (SNL 2007), which were generated using the baseline water table temperature map.

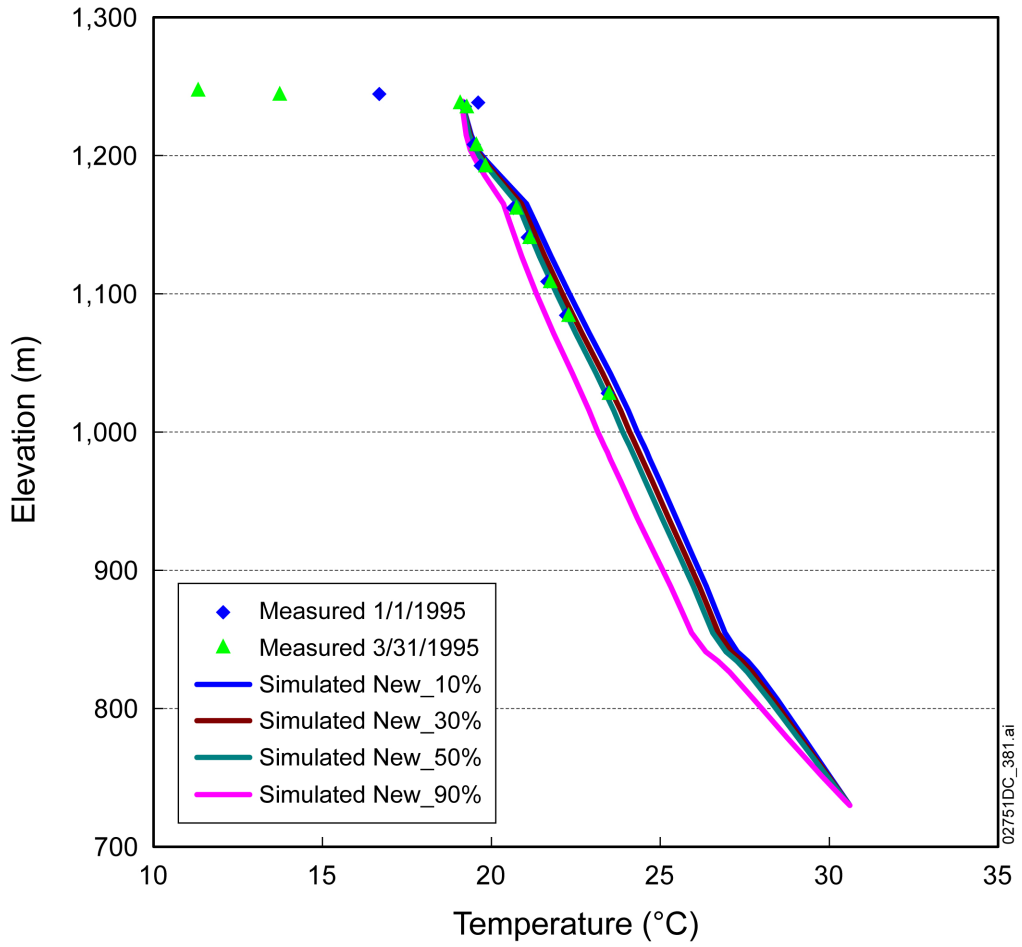

Figure 7. Comparisons between Measured and Modeled Ambient Temperature Profiles in Borehole NRG-6 for the Four Infiltration Maps of 10th, 30th, 50th, and 90th Percentile Present-Day Infiltration Rate

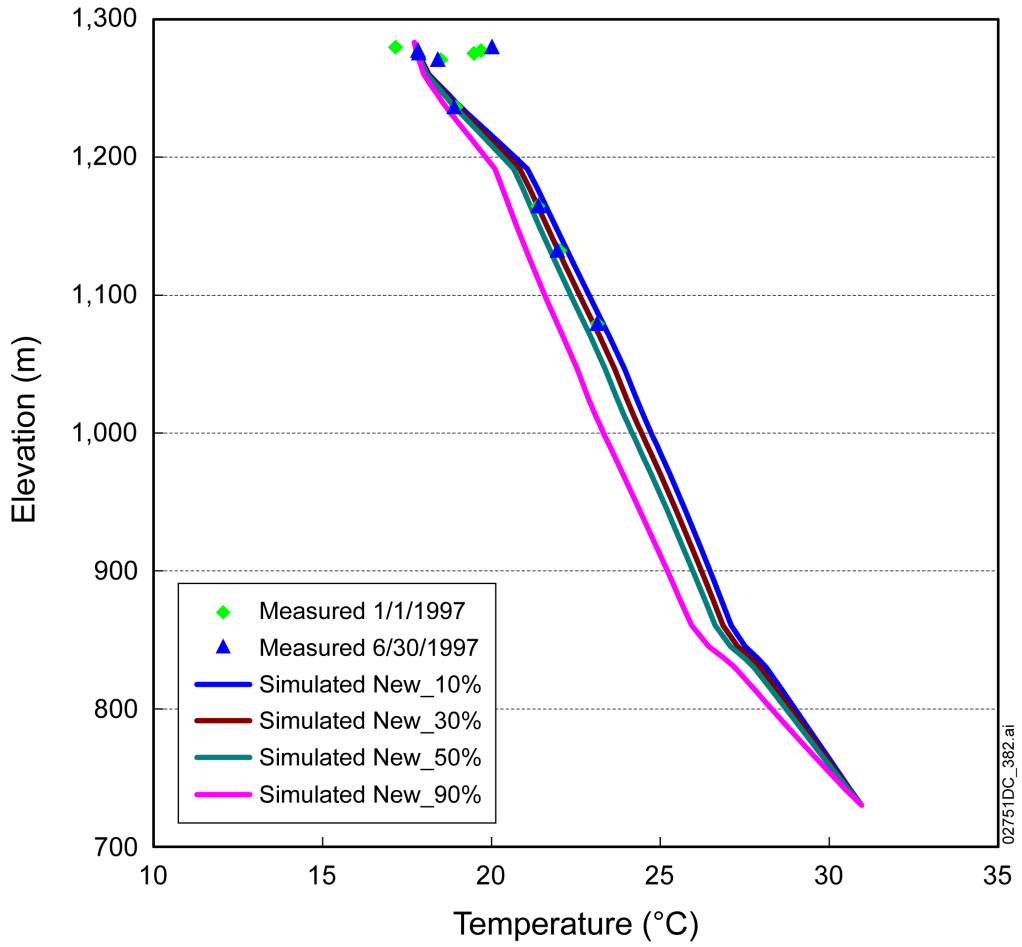

Figure 8. Comparisons between Measured and Modeled Ambient Temperature Profiles in Borehole NRG-7A for the Four Infiltration Maps of 10th, 30th, 50th, and 90th Percentile Present-Day Infiltration Rate

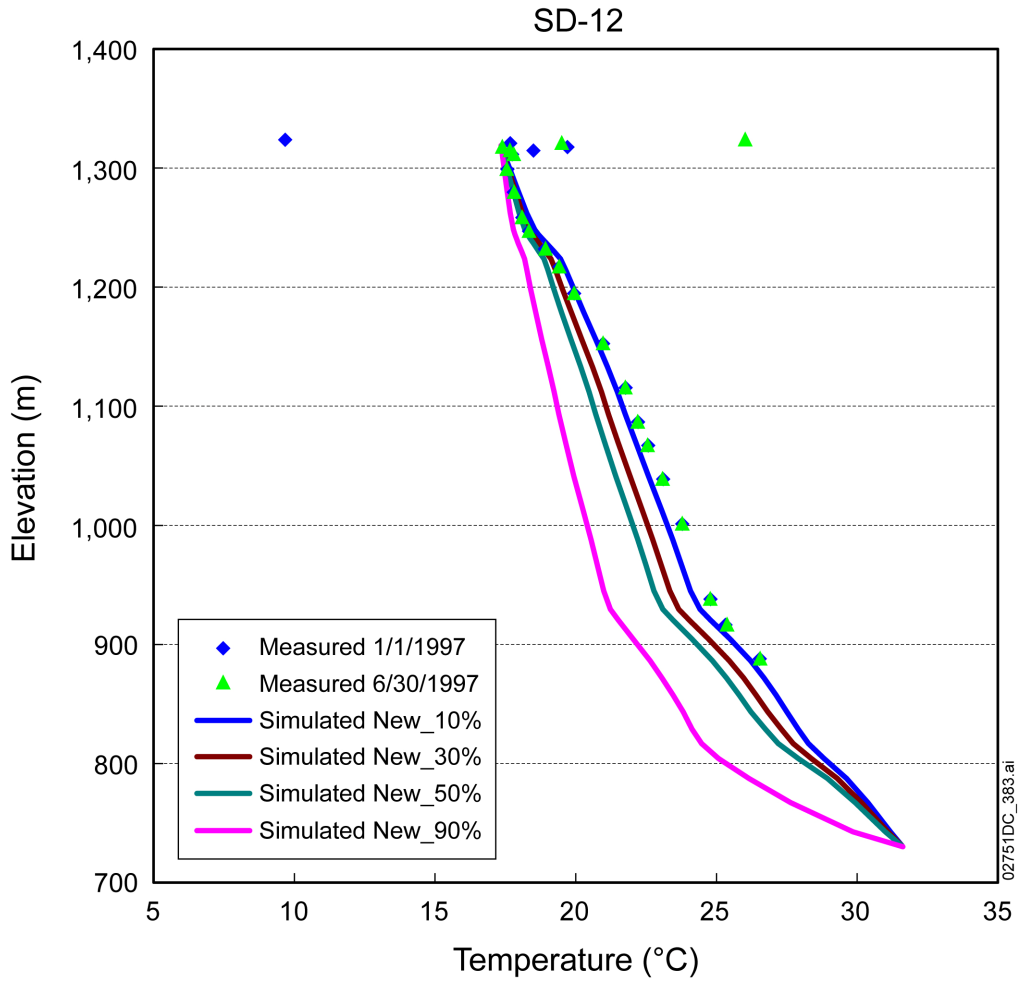

Figure 9. Comparisons between Measured and Modeled Ambient Temperature Profiles in Borehole SD-12 for the Four Infiltration Maps of 10th, 30th, 50th, and 90th Percentile Present-Day Infiltration Rate

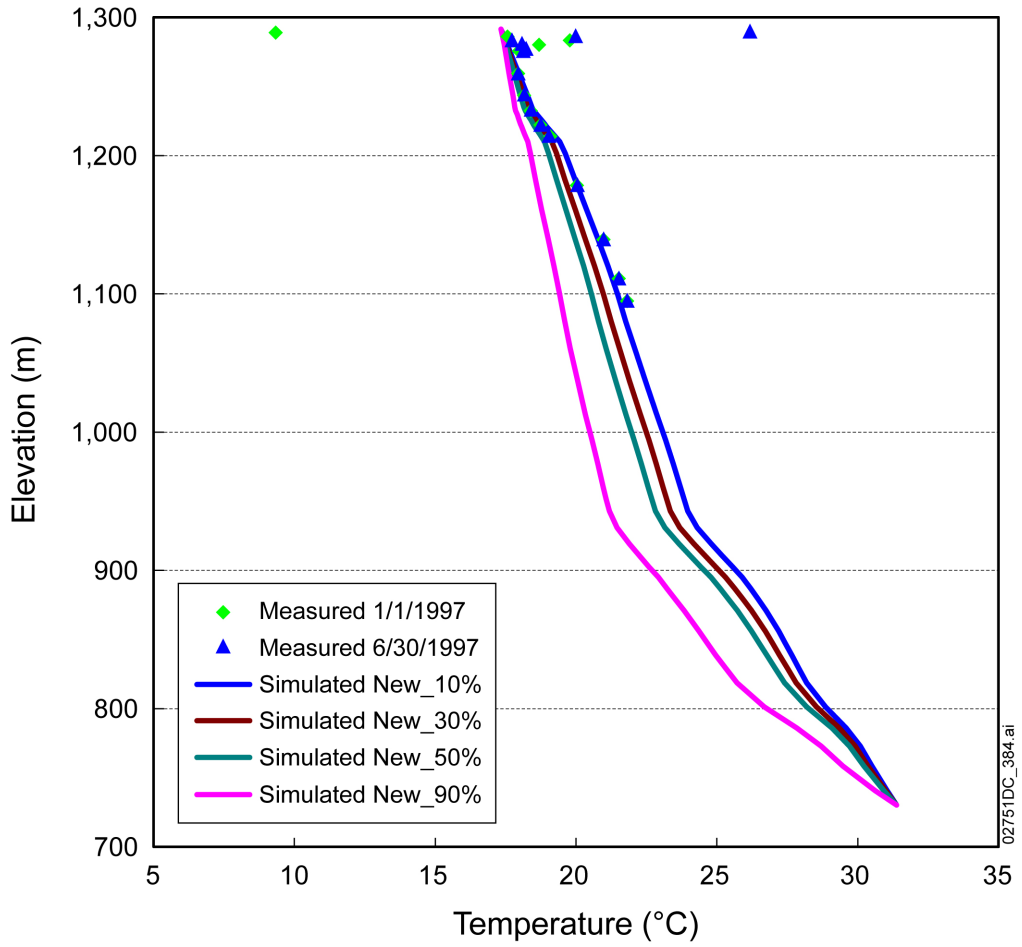

Figure 10. Comparisons between Measured and Modeled Ambient Temperature Profiles in Borehole UZ-7A for the Four Infiltration Maps of 10th, 30th, 50th, and 90th Percentile Present-Day Infiltration Rate

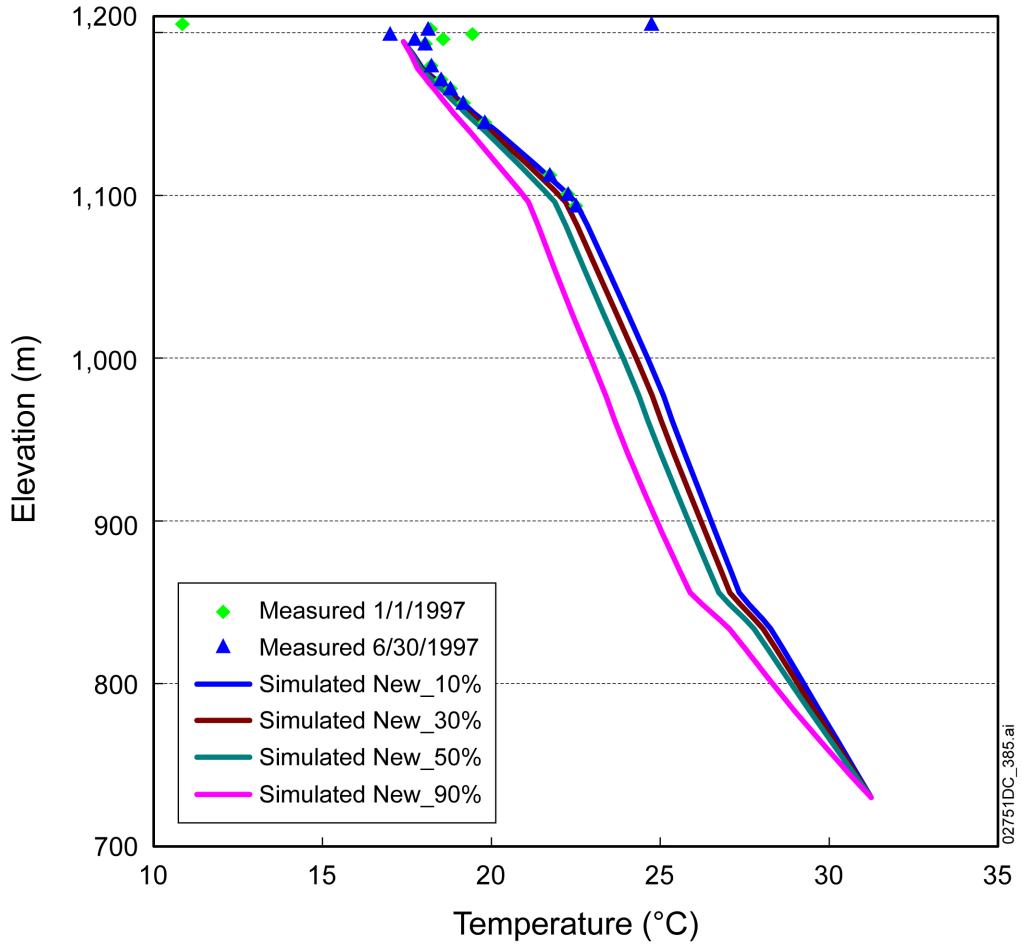

Figure 11. Comparisons between Measured and Modeled Ambient Temperature Profiles in Borehole UZ#5 for the Four Infiltration Maps of 10th, 30th, 50th, and 90th Percentile Present-Day Infiltration Rate

The revised model temperature profile estimates were then used to derive new weights for the 10th, 30th, 50th, and 90th percentile infiltration maps using the GLUE method as described in *UZ Flow Models and Submodels* (SNL 2007). The revised weights, based on temperature alone, are shown in Table 3. The designations S1, s2_a1_n=1, etc., are the different likelihood functions as described in *UZ Flow Models and Submodels* (SNL 2007, Section 6.8). As can be seen from Table 3, the changes to weights based on the revised water table temperature map are small relative to the uncertainty associated with the likelihood functions.

Table 3. Weighting Factors Considering Temperature Only

Infiltration Map	10%	30%	50%	90%
S1	100%	0%	0%	0%
s2_a1_n=1	25%	22%	49%	5%
s2_a1_n=0.5	24%	23%	41%	13%
s2_a2_n=1	23%	19%	53%	5%
s2_a2_n=0.5	23%	21%	43%	13%
s3_a1	82%	16%	2%	0%
s3_a2	87%	10%	3%	0%
s4_sum	22%	21%	31%	26%
Average	48%	17%	28%	8%
Previous average*	50%	15%	21%	14%

* Previous average from SNL 2007, Table 6.8-5.

NOTE: The sum of percentages over the 10% through 90% cases does not necessarily add to 100 because of rounding-off.

1.4 ASSIGNMENT OF SURFACE TEMPERATURES FOR GLUE ANALYSIS

Surface temperatures were computed for the thermal model boundary condition at the ground surface using a measured temperature reference value at USW NRG-6 and a standard lapse rate for temperature change with elevation. The standard lapse rate was verified for local conditions using surface temperatures at boreholes USW NRG-6 and UE-25 NRG-7a (SNL 2007, Section 6.3.2). Although this method is a standard approximation for estimating air temperature variations as a function of elevation, it does not precisely predict the average temperatures measured at other boreholes, where such measured data are available.

For boreholes with temperature measurements, surface temperatures at the boreholes can also be estimated from measured temperatures. For USW NRG-7a and UE-25 UZ#5, temperatures were measured at depths of about 3 m (10 ft) and deeper. This is also the closest temperature measurement to the ground surface that does not have significant diurnal variations. The data from these boreholes were taken over three complete years from 1995 to 1997 for USW NRG-7a and for two complete years from 1996 to 1997 for UE-25 UZ#5. The data show that average surface temperatures at these two boreholes are between 0.5°C to 1°C cooler than the model boundary conditions.

1.4.1 Surface Temperature Variations and Longer-Term Average Temperature

The thermal model used for evaluation of temperature profiles and infiltration rates in the GLUE method is based on the steady-state approximation, including a steady-state surface temperature. Thermal equilibrium for the full thickness of the unsaturated zone has been estimated to require on the order of 10,000 years (SAR Section 2.3.2.4.1.2.4.5.2; SNL 2007, Section 6.3.2). For the temperature profiles used to constrain the GLUE analysis, including profiles from the upper part of the unsaturated zone, the equilibration time is on the order of hundreds to thousands of years.

Surface temperature variations at USW NRG-7a are shown in Figure 12. This figure shows the strong seasonal temperature variations but also shows 1°C to 2°C year-to-year variations. Figure 13 shows yearly average temperature variations at the Site 2 meteorological station at Yucca Mountain and at Amargosa Farms. While UE-25 NRG-7a has about a three-year record, the Site 2 meteorological station has a record of about 10 years and Amargosa Farms has a record of about 25 years. The Site 2 meteorological station data suggest that the 1995 to 1997 period was 1°C warmer than the two-year period prior to 1995, and about 0.3°C warmer than the five-year period following 1997. The Amargosa Farms temperature record shows similar trends, indicating that the average temperature over the 1995 to 1997 time period is about 0.54°C above the 16-year average temperature prior to 1995, and 0.43°C above the seven-year average temperature following 1997.

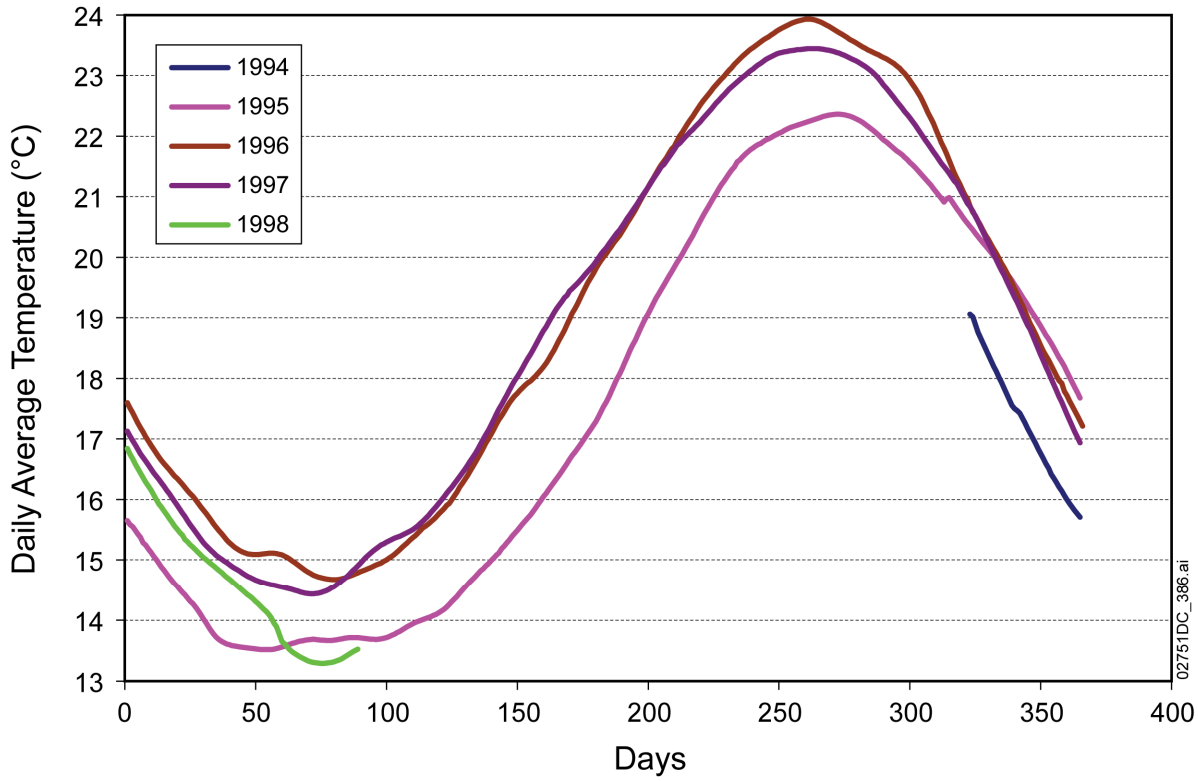

Figure 12. Surface Temperatures at USW NRG-7a

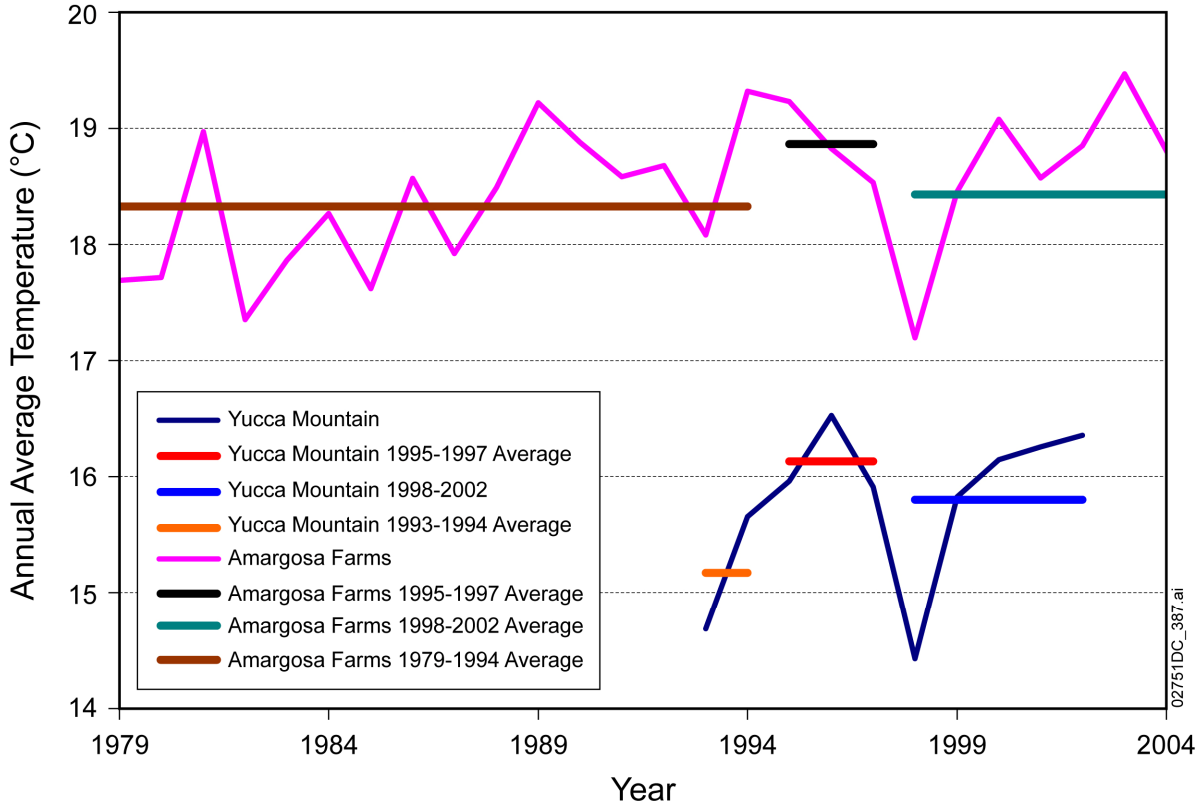

Figure 13. Average Annual Temperatures at the Site 2 Meteorological Station and Amargosa Farms

A nearly continuous daily temperature record has been taken for the last 60 years at Nellis Air Force Base. The yearly average temperatures based on this record are shown in Figure 14. From these data, the average temperature over 46 years prior to 1995 is 1.4°C cooler than the 1995 to 1997 average and 0.4°C cooler than the 11 years following 1997. Therefore, both local and regional temperature records indicate that the 1995 to 1997 time period was anomalously warm, by about 0.5°C to more than 1°C relative to average temperatures prior to this period, as recorded at different stations for various time periods. Therefore, the surface temperatures used for thermal modeling of subsurface temperatures at boreholes UE-25 NRG-7a and UE-25 UZ#5 cannot be considered underestimates. The potential bias in surface temperatures at other boreholes as a result of higher temperatures during 1995 to 1997 is conservative because it leads to higher weights in the GLUE analysis for higher infiltration scenarios.

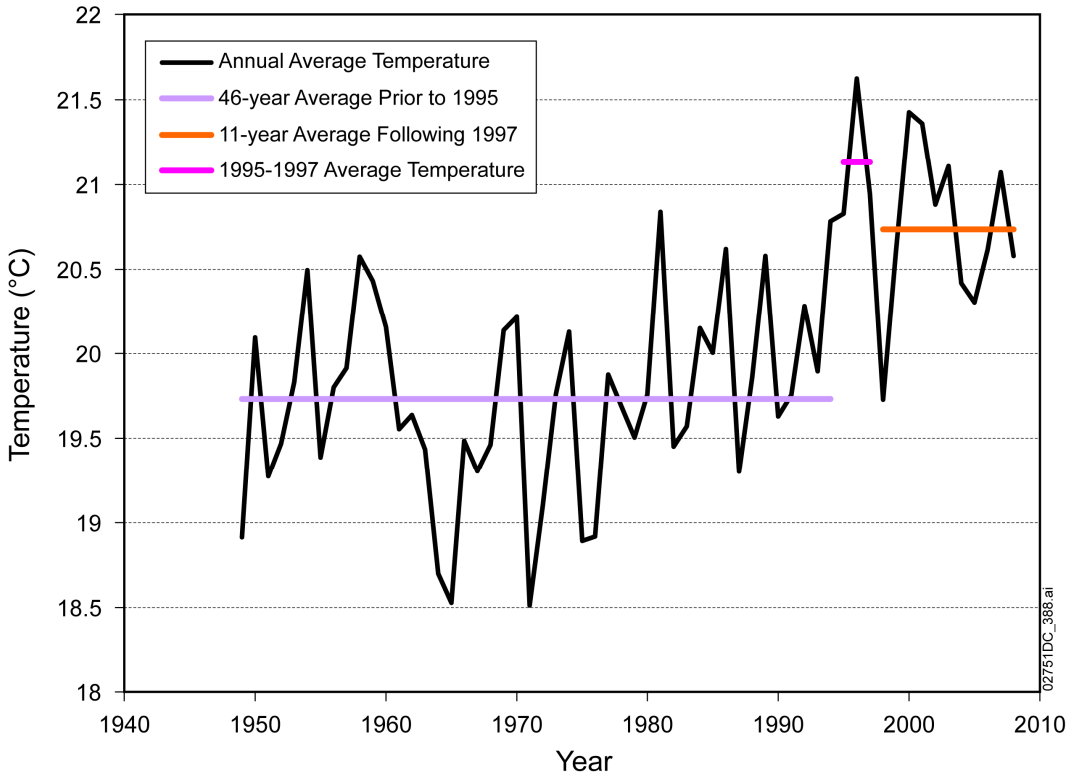

Figure 14. Yearly Average Temperatures at Nellis Air Force Base

1.5 SUMMARY

The Sass et al. (1988) data set for borehole temperatures shows that temperature measurements were subject to time-dependent variations on the order of 1°C over the entire borehole profile. This temperature variation was documented by Sass et al. (1988) to be a result of air convection in the open borehole environment used in the measurements. The second set of borehole temperature measurements was acquired using an instrumentation method that substantially reduced borehole air convection. These measurements show less than 0.1°C variation below depths greater than 80 feet for repeat measurements at different times. The second set of borehole temperature measurements provides the stability needed for the GLUE analysis because of the small temperature variations between the model predictions for different infiltration scenarios, as shown in Figures 7 to 11. Therefore, it was appropriate not to use the Sass et al. (1988) temperature measurements as primary borehole temperature data for the GLUE analysis.

Because the more stable temperature measurements were not taken at or near the water table, the best available data for constructing a water table boundary condition for the unsaturated zone thermal model are those from Sass et al. (1988). These data were qualified for this use, although, as noted, they were not qualified for use in analysis of borehole temperature profiles. The GLUE analysis shows little sensitivity to changes in water table temperature on the order of 1°C. Therefore, the Sass et al. (1988) data are suitable for use in representing water table temperature as a boundary condition for the unsaturated zone thermal model.

Thermal conductivity data reported by Sass et al. (1988) have been compared with thermal conductivity data used for the baseline analysis. This comparison shows that differences between the data sets are only significant in thin units with few measurements or in units that are below the water table for the thermal boreholes used in the GLUE analysis. A sensitivity analysis conducted with baseline thermal conductivity values, and those from Sass et al. (1988), shows only minor differences in predicted temperatures.

An alternative water table temperature map was developed based on direct interpolation of the Sass et al. (1988) water table temperature measurements. Differences in water table temperatures on the order of 1°C were identified. An analysis of the effects of these differences in the water table temperature boundary condition for the unsaturated zone thermal model and the associated GLUE analysis for weighting factors showed little sensitivity to the changes.

Long-term average surface temperatures at boreholes USW NRG-7a and UE-25 UZ#5 were found to be about 0.5°C to 1°C cooler than the values used in the unsaturated thermal model, which were based on observations conducted at these boreholes over a two- to three-year measurement period from 1995 to 1997. The longer-term temperature records at Yucca Mountain and at regional meteorological stations indicate that the 1995 to 1997 period was anomalously warm by 0.5°C to more than 1°C relative to average temperatures for periods of various length prior to 1995. Therefore, the surface temperatures used for modeling steady-state temperature profiles at boreholes USW NRG-7a and UE-25 UZ#5 are not underestimated for the purpose of modeling temperature profiles in the unsaturated zone.

These results demonstrate that percolation flux is not underestimated because (i) the GLUE weighting factors are not sensitive to differences between the baseline water table temperature map and an alternative water table temperature map based on direct interpolation; (ii) the top temperature boundary condition is not underestimated relative to long-term average conditions; and (iii) temperature profiles are not sensitive to differences between the baseline thermal conductivities and those measured by Sass et al. (1988).

2. COMMITMENTS TO NRC

None.

3. DESCRIPTION OF PROPOSED LA CHANGE

None.

4. REFERENCES

Bodvarsson, G.S.; Kwicklis, E.; Shan, C.; and Wu, Y.S. 2003. "Estimation of Percolation Flux from Borehole Temperature Data at Yucca Mountain, Nevada." *Journal of Contaminant Hydrology*, *62-63*, 3-22. New York, New York: Elsevier.

Sass, J.H.; Lachenbruch, A.H.; Dudley, W.W., Jr.; Priest, S.S.; and Munroe, R.J. 1988. *Temperature, Thermal Conductivity, and Heat Flow Near Yucca Mountain, Nevada: Some Tectonic and Hydrologic Implications.* Open-File Report 87-649. Denver, Colorado: U.S. Geological Survey.

SNL (Sandia National Laboratories) 2007. *UZ Flow Models and Submodels.* MDL-NBS-HS-000006 REV 03 AD 01. Las Vegas, Nevada: Sandia National Laboratories. ACC: DOC.20080108.0003; DOC.20080114.0001; LLR.20080414.0007; LLR.20080414.0033; LLR.20080522.0086; DOC.20090330.0026.

RAI Volume 3, Chapter 2.2.1.3.6, First Set, Number 3:

Explain how the DOE abstraction estimate for thermal seepage temperature threshold (SAR Sections 2.3.3.3 and 2.3.3.4) is consistent with observations from heater tests. Explain why the DOE thermal seepage abstraction would not underestimate water seeping into the drift when considering: (i) observations in heater tests related to temperature fluctuations recorded by sensors in both grouted and open boreholes, and (ii) the uncertainty of boiling temperature of water inferred from the possibly high total dissolved solids associated with water that corroded test apparatus. Aspects of this request related to open boreholes should reflect the DOE response to Scenario Chapter Set 5, RAI #4 concerning FEPs 1.1.01.01.0B and 2.1.06.04.0A. This information is needed to verify compliance with 10 CFR 63.114(a), (c), (e), and (g).

Basis: The DOE abstraction for thermal seepage is that seepage into the drift is set to zero if the drift wall temperature is calculated to be above 100°C (SAR Section 2.3.3.4). This temperature, being several degrees above boiling, reportedly accounts for modeling uncertainties and the possibility of a heat pipe occurring near the drift wall (SAR Section 2.3.3.3.4).

Analysis of several heater tests suggests that observations of temperature fluctuations could be explained by liquid water preferentially breaching the dryout zone (Green, et al., 2008) at temperatures above 100°C. Large temperature fluctuations at temperatures above boiling could be indicative of pulses of water preferentially flowing in the dryout zone. These observations occurred in both grouted and ungrouted boreholes. Observations in grouted boreholes would appear to reflect pulses of water flowing in fractures. Observations in ungrounted boreholes (e.g., MPBX boreholes in the Drift Scale Heater Test) would appear to reflect heat pipes inside an open borehole.

In addition, there are post-test observations consistent with water having entered the heated opening and corroding test components; however, the temperature at which this occurred has not been determined (Green, et al., 2008). Because the chemistry of the liquid entering the drift is unknown, though apparently corrosive, the boiling temperature of the liquid would be uncertain. The 100°C thermal seepage threshold does not account for the uncertainty related to refluxing water redissolving evaporites (SAR Section 2.3.3.3.4).

1. RESPONSE

The abstraction approach for thermal seepage using a temperature threshold (SAR Sections 2.3.3.3 and 2.3.3.4) is consistent with observations from heater tests. The thermal seepage abstraction does not underestimate water seeping into the drift when considering: (1) observations in heater tests related to temperature fluctuations recorded by sensors in grouted and open boreholes, and (2) the uncertainty of the boiling temperature of water inferred from the possibly high total dissolved solids associated with water that corroded test apparatus. The thermal reflux in heterogeneous rock for Yucca Mountain will differ from that seen in the Large Block Test. Similarly, test results seen in the Drift Scale Test will not be seen in repository drifts due to the relatively short time period during which conditions that would allow thermal reflux in open boreholes could exist. The open boreholes will not cause seepage enhancement. Also, due to the dilute nature of pore-water, total dissolved solids (TDS) will not impact the boiling temperature of water. Finally, representation of the drip shield function, supported by features, events and processes (FEP) screening analyses and the total system performance assessment for the License Application (TSPA-LA), shows that seepage caused by thermal reflux during the thermal period, if it were to occur, is not significant to repository performance. Aspects of this request related to thermal reflux in open boreholes are consistent with the response to RAI 3.2.2.1.2.1, Set 5, Number 3, not Number 4, as discussed in the clarification call with the NRC. That RAI (Number 3) concerns FEPs 1.1.01.01.0B and 2.1.06.04.0A.

1.1 THERMAL REFLUX IN THE FRACTURED ROCK MASS

Of all the heater tests reviewed by Green et al. (2008), only the Large Block Test (LBT) has observations of temperature fluctuations in sensors embedded in grouted boreholes, suggesting the possibility of thermal reflux within the heterogeneous fractured rock mass. These fluctuations occurred in two distinct events starting around 2,500 and 4,500 hours, respectively. This response therefore focuses on these LBT observations. The LBT was operated under conditions favorable for thermal reflux to occur, which are very different from the future conditions expected at Yucca Mountain. The predictive models used for thermal seepage evaluation explicitly allow for the possibility of thermal reflux into an above-boiling rock domain, and these predictive models are able to simulate the temperature fluctuations observed in the LBT.

1.1.1 Large Block Test Conditions

The LBT was conducted above ground in an outcrop of the middle nonlithophysal unit of the Topopah Spring tuff in the Fran Ridge area of Yucca Mountain (Wilder et al. 1997; Lin et al. 2001). The test block (3 × 3 × 4.5 m) was excavated mechanically, with only the bottom remaining attached to the underlying rock. The four sides were kept open but covered with heavy insulation materials. The top surface was not insulated; a heat exchanger was installed to keep the temperature of the top surface at a constant 60°C. Aspects of the LBT important to this discussion include:

- The block was heated by mechanical heaters placed into five horizontal boreholes distributed evenly over the heater plane, which was situated 1.75 m above the base of the block. The heat output was strong enough to create above-boiling conditions in the

entire mid-section of the test block. This means that condensate (or any other source of water) accumulating in the upper portion of the block could not easily divert around the heaters and drain off. In other words, a pool of condensate could accumulate above the heater horizon, generating strong heat pipe conditions and providing a significant source of water for thermal reflux. This test condition was different from the future conditions in the repository, where a large portion of rock between adjacent tunnels will remain below boiling at all times, thus allowing for condensate drainage around the superheated fractured rock (e.g., BSC 2005 Section 6.2).

- The test block contained numerous fractures, with a set of near-vertical fractures spanning the entire height of the block. The thermal-hydrological behavior of the LBT was affected by the presence of these distinct fractures (Mukhopadhyay and Tsang 2002 Sections 1 and 5), which provided a direct downward conduit for any water introduced—or condensate generated—at the top of the block.

- The two distinct events with temperature fluctuations in two vertical boreholes were discussed by Mukhopadhyay and Tsang (2002). Both events were caused by a strong disturbance of the thermal-hydrological situation above the heater plane. The first event was related to a malfunction of the heat exchanger at the top of the test block, which induced more intense condensation and thus more thermal reflux. The second event was induced by strong rainfall, which provided a source of cooler water infiltrating into the test block and draining towards the heaters. In the future repository, where external thermal-hydrological disturbances can be ruled out, the magnitude and evolution of thermal reflux near emplacement drifts is directly linked to the magnitude and evolution of thermal perturbation (Birkholzer and Zhang 2006). It follows that the condensation-driven downward flux at Yucca Mountain will be at its maximum when the temperature in the rock is highest and the dryout zone is largest (i.e., refluxing water may locally breach the dryout zone but will not be able to penetrate far down and reach the drifts). This temporal correlation between flux intensity and extent of the boiling zone is important to preventing thermal seepage (Birkholzer et al. 2003).

In summary, the thermal-hydrological behavior of the LBT is not representative of the future conditions expected at Yucca Mountain, in particular with respect to the two prominent thermal events with temperature fluctuations observed in grouted boreholes. These two events were triggered by external perturbations generating sudden changes in the amount of liquid present above the heater plane, in one case from more effective condensation, in the second case from rainfall infiltrating into the test block. Discrete fractures then provided a direct and effective pathway from the source of the water at the top of the block to the heater plane. Since the entire heater plane of the test block was at a temperature above boiling, the refluxing water could not divert around the heated area. As a result, some of the water locally breached the dryout zone, boiled off, vapor moved away from the heater, condensed, and, with this cycle repeating, generated heat pipe signals and temperature fluctuations in grouted boreholes. No such fluctuations were observed in any other heater test conducted at Yucca Mountain, and in particular, not in the Drift Scale Test (DST), which most closely resembles the thermal setup and

conditions in the future repository. Also there was no indication of water actually seeping into the heater holes of the LBT.

1.1.2 Conceptual Model for Thermal Seepage

The predictive model used for thermal seepage evaluation explicitly allows for the possibility of thermal reflux and preferential breaching in an above-boiling rock domain (SAR Section 2.3.3.3.3.1; BSC 2005 Section 6.2.1.1.2; Birkholzer and Zhang 2006; included FEP 2.2.10.10.0A). The model represents the small-scale heterogeneity in the permeability of the fractured rock mass to allow for the presence of high-permeability features and preferential flow processes. The active fracture concept is utilized in conjunction with a dual continuum approach to account for the fact that unsaturated flow is restricted to a small number of (active) fractures, and that flow within a fracture is likely to occur in individual fingers rather than the entire fracture plane (SAR Section 2.3.3.3.3.1). Furthermore, to account for the limited exchange of heat between the rock matrix (where most of the energy is conducted) and the fractures (where most of the liquid reflux occurs), due to flow channeling and/or fingering, the interface area available for heat flow between the matrix and the liquid flow in fractures was reduced significantly compared to the full geometric area (SAR Section 2.3.3.3.3.1; BSC 2005, Section 6.2.1.1.2). These conceptual model choices—small-scale heterogeneity, active fracture model, and reduced interface area for heat transfer—all promote preferential flow in the fractures and allow for penetration of liquid flow into the superheated rock zone. The abstraction of thermal seepage utilizes these modeling results to develop a thermal seepage abstraction methodology (SNL 2007a, Section 6.5.2). However, according to the predictions for the future conditions at Yucca Mountain, the penetration of liquid flow into the superheated rock zone is not significant during the time that the crown temperature is above boiling, because: (a) much of the mobilized condensate is diverted around the dryout zone, and (b) the vaporization barrier is most effective when the thermal perturbation (i.e., the amount of thermal reflux) is strongest.

A simulation model using a conceptual approach (see Birkholzer and Zhang 2006) similar to the thermal seepage model for the Yucca Mountain conditions (i.e., using model choices such as dual continuum approach, active fracture model, and reduced interface area for heat transfer) was applied to a laboratory heater experiment conducted by the Center for Nuclear Waste Regulatory Analyses at the Southwest Research Institute in San Antonio (Green and Prikryl 1998; Green and Prikryl 1999; Green et al. 2003). This experiment was conducted using artificial water release at the top of the experimental apparatus, thereby testing the potential for thermal reflux and breaching of the dryout zone. Test results indicated that water rapidly flowing in vertical fractures penetrated the above-boiling rock region and seeped into a horizontal cavity that contained an electrical heater. The model was able to reproduce the experimental observation of thermal seepage; the simulations suggest that a strong heat pipe with significant thermal reflux formed near the heater borehole, with temperature in the fractures at or near boiling, despite the matrix temperatures being much higher (Birkholzer and Zhang 2006). While the thermal seepage observations in the heater experiment are not representative of the conditions expected at Yucca Mountain, the good agreement between simulation and data provides confidence in the conceptual model.

1.1.3 Modeling of the Large Block Test

Mukhopadhyay and Tsang (2002) developed a simulation model for thermal-hydrological processes in the LBT and used this model to investigate the temperature fluctuations observed during the rain event around 4,500 hours of heating. They demonstrated that the anomalous temperature data can be reproduced by the model when the heterogeneity of the fractured rock mass is accounted for. This model confirms that the irregular temperature patterns observed in the grouted vertical boreholes occur because of large amounts of rainwater reaching the heat source through highly permeable inclined fractures. In other words, it was demonstrated in Mukhopadhay and Tsang (2002) that the thermal fluctuations in the LBT are a result of an external perturbation coupled with the specific test setup and geometry, all of which are not representative of the future conditions at Yucca Mountain.

1.2 THERMAL REFLUX IN OPEN BOREHOLES

For this response, the boreholes discussed are from ground support rock bolts. The discussion does not apply to boreholes resulting from surface drilling. The RAI statements concerning thermal reflux in open boreholes are based on observations of temperature oscillations from sensors emplaced in ungrouted boreholes. Green et al. (2008) reviewed several heater tests conducted within the Yucca Mountain program and described in detail evidence for such oscillations in the Climax Small-Diameter Borehole Heater Tests and in the DST. The temperature excursions in the DST occurred in ungrouted boreholes holding multipoint borehole extensometer (MPBX) assemblies, originating from the drift wall into the fractured rock. Except for the MPBX assembly, the boreholes were essentially open for axial flow of vapor or liquids. Thermal refluxing can occur in such vertical or subvertical boreholes when the borehole collar is in an above-boiling environment and the borehole end extends past the bulk rock boiling isotherm. The borehole then provides a conduit for upward movement of vapor that has been generated from pore water on the hot end. As vapor condenses on the cooler end, it provides a source of water that can flow back towards the borehole collar.

The emplacement drift ground support is described in SAR Section 1.3.4.4, as well as in *Ground Control for Emplacement Drifts for LA* (BSC 2007 Section 6.6). The initial ground support will consist of 1.5-m-long carbon steel frictional rock bolts and wire mesh. The permanent ground support will consist of radial, stainless-steel, 3-meter long Swellex-type rock bolts which fasten overlapping perforated stainless steel sheets to the drift wall.

Swellex-type rock bolts are expanded by high-pressure water such that the bolts compact the material surrounding the hole and deform to fit irregularities at the borehole wall, providing frictional and mechanical interlock (SAR Section 1.3.4.4; BSC 2007, Section 6.6.1.1, p. 82). The major portion of the interface between the rock bolt and the rock wall resembles a natural small-aperture rock fracture with many asperity contacts providing the frictional and mechanical interlock. The exception is a small, inwardly curved portion of the rock bolt tube that is not in intimate contact with the rock wall after the Swellex-type rock bolts is inflated (see Figure 6-30 in BSC 2007). To expand the bolt by high-pressure water, the inside of the bolt is sealed at both ends, with a domed face-plate at the collar end of the rock bolt. Once the rock bolt has expanded, the water is allowed to drain via a small hole in the domed face plate. Thus, boreholes equipped

with Swellex-type rock bolts will not act like completely open boreholes (or like the MPBX boreholes in the DST). There will be resistance to vapor-liquid flow processes in the asperity between the rock bolt metal sheet and the rock surface, similar to the resistance in natural rock fractures at Yucca Mountain. There will also be resistance to vapor entry into the inner portion of the rock bolt, as the metal tube excludes pore water and vapor from entering, with the exception of the small hole in the domed faced plate. The processes leading to thermal reflux are different from those occurring in completely open boreholes, and the potential for—as well as the intensity of—thermal reflux within the boreholes used for repository ground support is likely much smaller.

Split-Set type frictional rock bolts will potentially be used for the initial ground support system. The difference between the two frictional rock bolt types is that the Split-Set system exerts radial pressure against the rock as the metal tube is pushed into a hole. With respect to the potential for thermal reflux, the two systems are similar: both have a small fracture-type opening between the rock bolt and the borehole wall, and both have a metal tube that excludes pore water and vapor from entering. The Split-Set tube, however, is open at the collar and along its length, such that vapor can more readily enter from the drift and refluxing liquid can more readily escape.

Swellex-type rock bolts have been used for ground support in the heated drift of the DST. As reported in *Thermal Testing Measurements Report* (SNL 2007b) and by Green et al. (2008), observations made after conclusion of the test may indicate water entry into the heated drift. These observations include a few corroding cables on the floor of the tunnel, one instance of staining along the ceiling emanating from a rock bolt, and a few stains on floor canisters, with the locations of the stains correlated to borehole collars at the roof. With the exception of the red stains on the floor canisters, the observations were made when the test was being dismantled, so that the timing could not be determined. The red stains were first observed during a video camera run in August 2002, suggesting that the material had been deposited between April and August 2002, during the period of rapid cooling after the heaters were turned off (SNL 2007b, Section 6.3.4.3.4). The red stains on the floor canisters are mostly iron oxides, likely derived from corrosion of the carbon-steel rock bolts. It is not clear whether the materials were deposited with dripping water or fell as particles from the roof.

The DST observations provide no direct evidence that thermal reflux in boreholes equipped with Swellex-type rock bolts caused water seepage during the heating period of the test. There is no evidence of thermal seepage for the crucial time period when large volumes of water were mobilized from boiling and strong vapor-liquid flow processes occurred that increased the potential for thermal reflux. The red spots on the floor heaters may have been deposited several months after the heaters were turned off while the test block was rapidly cooling. (The rapid cooling of the heater test is not representative of repository conditions, whereby the thermal output of the waste decreases slowly and cooling of the repository is a long-term, gradual process.) All other possible indications of water entry, such as the stain on the roof, may have occurred even later, possibly after rewetting of the rock mass near the heated tunnel. Therefore, the observations of possible water entry made in the DST are consistent with the DOE thermal seepage abstraction.

The permanent ground support system is designed to last at least 100 years with minimal maintenance. While no credit for rock reinforcement is taken in the License Application beyond the preclosure period, the longevity of the stainless steel rock bolts is probably much greater (BSC 2004a, Table 4-5), meaning they are likely to persist throughout the thermal period. The temporary rock bolts, on the other hand, will be made from carbon steel and are expected to corrode early, possibly starting during preclosure and continuing into the thermal period. Boreholes associated with temporary ground support may therefore provide open conduits for thermal reflux, and, as a result, may temporarily cause some dripping of water into the drifts when the drift wall temperature is greater than 100°C. The presence of these boreholes is not explicitly accounted for in the DOE predictive model for thermal seepage (BSC 2005). As mentioned above, significant thermal reflux can only occur in vertical or subvertical boreholes when vapor is produced in the rock near the collar while the end of the borehole is at below-boiling temperatures such that the migrating vapor condenses. The time period during postclosure at which these conditions are met is relatively short for 1.5-m-long boreholes. After the thermal pulse, all open boreholes will act as capillary barriers to the unsaturated flow in the fractured rock. Simulations conducted in *Seepage Model for PA Including Drift Collapse* (BSC 2004b, Section 6.5, pp. 6-13ff) demonstrate the effective capillary-barrier behavior of an open borehole in the fractured rock surrounding an emplacement drift and show that the presence of such boreholes does not lead to seepage enhancement.

1.3 IMPACT OF WATER CHEMISTRY ON BOILING TEMPERATURE OF WATER

The potential for concentrated brine evolution to contribute to seepage at temperatures higher than the threshold is insignificant. In the DST, water samples were collected from several boreholes, indicating fluid flow through intersecting fractures and/or thermal refluxing in the boreholes. The compositions of the fluids are given in *Thermal Testing Measurements Report* (SNL 2007b, Section 6.3.4) and discussed in detail in *Drift-Scale THC Seepage Model* (SNL 2007c, Section 7.1, Table 7.1-3). Water was collected from some borehole intervals for elapsed periods up to approximately one year. All temperatures in the producing intervals were below 100°C and most waters had lower total dissolved solids (TDS) than typical pore waters sampled by centrifugation of rock samples. Modeling of the DST showed that the water compositions were consistent with condensed water interacting with minerals on fracture surfaces, with limited mixing of matrix pore water. A few samples had elevated TDS (predominantly chloride and sulfate), possibly a result of matrix pore water interacting with condensate and undergoing evaporative concentration. These samples, however, were collected at temperatures below 90°C. There was no evidence of any brine having an elevated boiling point entering or forming in open boreholes.

The minor amounts of iron-rich particulates found on floor heater canisters in the DST, also contained minor amounts of halite, calcite, and rock dust apparently originating in part from corrosion of rock bolts (SNL 2007b, Section 6.3.4.3.4). Because these deposits were predominantly composed of insoluble iron oxide particulates, the deposits are not characteristic of high ionic strength brines. The deposits also appeared during a period of rapid cooling subsequent to the heaters being turned off, which is not representative of the conditions expected at Yucca Mountain because the cooling rate is much faster than the slow cooling that would accompany the period after boiling has ceased in the future repository.

Water compositions from ambient and elevated temperatures were also reported from a heater test performed at the Climax Mine (Green et al. 2008). The water collected from the heated zone (CEH#1) had lower concentrations of silica, chloride and sulfate compared to the water collected at ambient conditions, and higher concentrations of potassium and bicarbonate. The lower silica concentrations indicate that water-rock interaction was minimal and the lower chloride and sulfate indicate that the water was initially formed from a more dilute condensed fluid. High potassium with low silica may be related to interaction with man-made materials or some cation-exchange process. Whatever the exact mechanism of formation, the water was relatively dilute and was not consistent with a fluid having a significantly elevated boiling point.

The drift-scale thermal-hydrologic-chemical (THC) seepage model (SNL 2007c) includes evaporative concentration and salt accumulation, and the resulting effects on solution composition and mobility in fractures. Boiling point elevation is not explicitly included in this model. This simplification is justified because the evaporative concentration that causes boiling point elevation also greatly reduces the amount of liquid available for seepage. In the model, when the fracture liquid saturation drops below 10^{-5} or the ionic strength goes above 4 mol/kg water, the aqueous phase is treated as nonreactive and is not concentrated further (SNL 2007c, Section 5). However, a liquid saturation of 10^{-5} is much lower than the residual saturation for flow in fractures (about 0.01), meaning no flow would occur. It is significantly lower than the typical fracture saturation at which seepage from the rock mass into the drift can occur, which is typically in the range of 0.1 to 0.5 (BSC 2005, Section 6.2.2.2.2). Results from the drift-scale THC seepage model (SNL 2007c) did not show concentrated brines above the residual saturation for fractures. This characteristic comes from the dilute nature of pore waters in the unsaturated zone at Yucca Mountain, which are relatively low in soluble salts such as NaCl. These long-term predictions are also consistent with the lack of evidence for concentrated brines or elevated boiling temperatures in the DST.

1.4 DISCUSSION OF DRIP SHIELD FUNCTION DURING THERMAL PERIOD

Boreholes used for temporary rock bolts may provide pathways for thermal reflux, which could lead to some temporary dripping of water. Thus, the extent and quantity of seepage may be greater than is explicitly considered in the TSPA-LA. The discussion below demonstrates that such dripping of water is not significant to repository performance.

Significant thermal reflux may occur only until the rock temperature near the drifts falls below boiling, which occurs by 1,400 years after closure, at the latest (SAR Figure 2.3.5-32(a)). With the drip shield functioning as a barrier to seepage, radionuclide releases from failed waste packages are insensitive to variability in seepage (see DOE response to RAI 3.2.2.1.3.6-7). In addition, the effects on seepage chemistry of degrading ground support (including corrosion of steels) are addressed in excluded FEP 2.1.06.01.0A (SNL 2008a), where it is concluded that corrosion of steels in ground support does not significantly impact aqueous chemistry of seepage waters, and therefore thermal reflux does not affect performance of the drip shield in the nominal scenario. Thus, the effects of thermal reflux are limited to those TSPA-LA modeling cases where events may cause drip shield failure prior to 1,400 years and which use the seepage abstraction.

The TSPA-LA model considers three cases which use the seepage abstraction and in which drip shield failure may occur within 10,000 years: the drip shield early failure modeling case; the seismic fault displacement modeling case; and the seismic ground motion modeling case.

1.4.1 Individual Protection Standard (10 CFR 63.311)

The total mean annual dose (summed over all modeling cases) is compared to the limit specified in the individual protection standard. The contribution of each modeling case to the total mean annual dose is shown on SAR Figure 2.4-18(a). The mean annual dose from the drip shield early failure modeling case is more than two orders of magnitude below the total mean annual dose. The magnitude of the mean annual dose from the drip shield early failure modeling case is primarily determined by the low expected number of early-failed drip shields (SAR Section 2.4.2.2.1.2.4.1); thus, increasing either the occurrence or extent of seepage in the drip shield early failure modeling case would have a negligible effect on total mean annual dose. Similarly, the fault displacement modeling case contributes only a minor amount of the total mean annual dose, due to the low frequency of fault displacement events and the expected number of waste packages affected by fault displacement (SAR Section 2.4.2.2.1.2.2.2). Also, full collapse of the drift is generally associated with fault displacement (SNL 2008b, Sections 6.6.1.3.9 and 6.6.2.1) which would lead to borehole collapse as well. Therefore, thermal reflux in open boreholes has a negligible effect on the mean annual dose from seismic fault displacement.

The mean annual dose for 10,000 years from the seismic ground motion modeling case is estimated by considering only seismic-induced stress-corrosion cracking of codisposal waste packages (SAR Section 2.4.2.2.1.1.2). The potential contributions to mean annual dose of other consequences of vibratory ground motion are analyzed in *Total System Performance Assessment Model/Analysis for the License Application* (SNL 2008b, Section 7.3.2.6.1.3) and are determined to be minor compared to the contribution from seismic-induced stress-corrosion cracking of codisposal waste packages. In particular, the potential contribution to mean annual dose from seismic events that cause drip shield failure is shown in that report (SNL 2008b, Section 7.3.2.6.1.3.2) to be negligible. Seismic events sufficient to cause drip shield failure within 10,000 years (before significant drip shield plate thinning) (SNL 2007d, Table 6-36) are also of sufficient magnitude to cause significant rockfall (SNL 2007d, Tables 6-29 and 6-30). Significant rockfall with partial or full collapse of the drifts would lead to borehole collapse as well. Therefore, thermal reflux has a negligible effect on the mean annual dose from seismic ground motion, and on the total mean annual dose to the reasonably maximally exposed individual.

1.4.2 Standards for Protection of Groundwater (10 CFR 63.331)

Compliance with the separate standards for protection of groundwater is demonstrated in SAR Section 2.4.4. The models used to demonstrate compliance with the separate standards for protection of groundwater are the same as those used to demonstrate compliance with the individual protection standard. However, because unlikely FEPs are excluded for the analysis for the separate standards for protection of groundwater, the seismic fault displacement modeling case does not contribute to the estimates of performance (SAR Section 2.4, p. 2.4-326).

Figure 8.1-10[a] of *Total System Performance Assessment Model /Analysis for the License Application* (SNL 2008b) shows that most of the estimated mean concentration of radium in groundwater results from the seismic ground motion modeling case. Because thermal reflux has a negligible effect on this modeling case, the potential effect of thermal reflux on radium concentration is negligible.

Figure 8.1-12[a] of *Total System Performance Assessment Model /Analysis for the License Application* (SNL 2008b) shows that the largest contribution to the maximum of the estimated mean gross alpha concentration in groundwater results from the seismic ground motion modeling case. The drip shield early failure modeling case contributes modestly to the overall mean concentration. The maximum of the estimated mean gross alpha concentration in groundwater is nearly four orders of magnitude below the limit specified in 10 CFR 63.331. An increase in the occurrence and volume of seepage resulting from thermal reflux may increase the mass of alpha-emitting radionuclides transported to the groundwater in the drip shield early failure modeling case. However, any potential contribution to seepage from thermal reflux would not be sufficiently large (i.e., orders of magnitude larger in volume) to alter the demonstration of compliance. Thus, the potential effect of thermal reflux on radium concentration is negligible.

Figure 8.1-15[a] of *Total System Performance Assessment Model /Analysis for the License Application* (SNL 2008b) shows that essentially all of the maximum whole body and organ dose from beta and photon emitting radionuclides results from the seismic ground motion modeling case. Because thermal reflux has a negligible effect on this modeling case, the potential effect of thermal reflux on whole body and organ doses is negligible.

1.5 SUMMARY

The potential for thermal reflux in the fractured rock mass is adequately accounted for in the predictive model and abstraction method for thermal seepage (Section 1.1). Boreholes used for temporary rock bolts may provide pathways for thermal reflux, which could lead to some dripping of water for a limited time after repository closure (Section 1.2). The potential for concentrated brine to contribute to seepage at temperatures greater than the thermal seepage threshold is insignificant (Section 1.3). Although the extent of seepage during the thermal period may be greater than that represented explicitly in the TSPA-LA, however, such seepage would not be significant to repository performance (Section 1.4).

2. COMMITMENTS TO NRC

None.

3. DESCRIPTION OF PROPOSED LA CHANGE

None.

4. REFERENCES

Birkholzer, J.T.; Mukhopadhyay, S.; and Tsang, Y.W. 2003. "The Impact of Preferential Flow on the Vaporization Barrier Above Waste Emplacement Drifts at Yucca Mountain, Nevada." *Journal of Nuclear Technology, 148*, 138 through 150.

Birkholzer, J.T. and Zhang, Y. 2006. "The Impact of Fracture-Matrix Interaction on Thermal-Hydrological Conditions in Heated Fractured Rock." *Vadose Zone Journal*, *5*, 657–672. Madison, Wisconsin: Soil Science Society of America.

BSC (Bechtel SAIC Company) 2004a. *Aqueous Corrosion Rates for Waste Package Materials.* ANL-DSD-MD-000001 REV 01. Las Vegas, Nevada: Bechtel SAIC Company. ACC: DOC.20041012.0003; DOC.20060403.0001; LLR.20080324.0021; LLR.20080519.0002.

BSC 2004b. *Seepage Model for PA Including Drift Collapse.* MDL-NBS-HS-000002 REV 03. Las Vegas, Nevada: Bechtel SAIC Company. ACC: DOC.20040922.0008; DOC.20051205.0001.

BSC 2005. *Drift-Scale Coupled Processes (DST and TH Seepage) Models.* MDL-NBS-HS-000015 REV 02. Las Vegas, Nevada: Bechtel SAIC Company. ACC: DOC.20050114.0004; DOC.20051115.0002.

BSC 2007. *Ground Control for Emplacement Drifts for LA.* 800-K0C-SSE0-00100-000-00C. Las Vegas, Nevada: Bechtel SAIC Company. ACC: ENG.20070925.0082; ENG.20080304.0028.

Green, R.; Painter, S.; Fratesi, B.; Manepally, C.; and Walter, G. 2003. *Status Report for Multiphase Flow Simulation*. San Antonio, Texas: Center for Nuclear Waste Regulatory Analyses. ACC: LLR.20070927.0115.

Green, R.T. and Prikryl, J.D. 1998. "Penetration of the Boiling Isotherm by Flow Down a Fracture." *Proceedings of the Third International Conference on Multiphase Flow, ICMF'98, Lyon, France, June 8-12, 1998*. pp. 1-7. Halle (Saale), Germany: Martin-Luther-University Halle-Wittenberg.

Green, R.T. and Prikryl, J.D. 1999. "Formation of a Dry-Out Zone Around a Heat Source in a Fractured Porous Medium." *Proceedings of the Second International Symposium on Two-Phase Flow Modelling and Experimentation Pisa, Italy, 23–26 May, 1999*. Celata, G.P., Di Marco, P., and Shah, R.K., eds. III, III-1849–III-1856. Pisa, Italy: Edizioni ETS.

Green, R.; Manepally, C.; Fedors, R.W.; and Roberts, M.M. 2008. *Examination of Thermal Refluxing in In-Situ Heater Tests*. Center for Nuclear Waste Regulatory Analyses, San Antonio, Texas.

Lin, W.; Blair, S.C.; Wilder, D.; Carlson, S.; Wagoner, J.; DeLoach, L.; Danko, G.; Ramirez, A.L.; and Lee, K. 2001. *Large Block Test Final Report*. Rev. 2. UCRL–ID–132246. Livermore, California: Lawrence Livermore National Laboratory.

Mukhopadhyay, S. and Tsang, Y.W. 2002. "Understanding the Anomalous Temperature Data From the Large Block Test at Yucca Mountain, Nevada." *Water Resources Research*, 38, (10) DOI: 10.1029/2001WRR001059.

SNL (Sandia National Laboratories) 2007a. *Abstraction of Drift Seepage.* MDL-NBS-HS-000019 REV 01 AD 01. Las Vegas, Nevada: Sandia National Laboratories. ACC: DOC.20070807.0001; DOC.20080813.0004; DOC.20081118.0049[a].

SNL 2007b. *Thermal Testing Measurements Report.* TDR-MGR-HS-000002 REV 01. Las Vegas, Nevada: Sandia National Laboratories. ACC: DOC.20070307.0010.

SNL 2007c. *Drift-Scale THC Seepage Model.* MDL-NBS-HS-000001 REV 05. Las Vegas, Nevada: Sandia National Laboratories. ACC: DOC.20071010.0004; LLR.20080408.0266.

SNL 2007d. *Seismic Consequence Abstraction.* MDL-WIS-PA-000003 REV 03. Las Vegas, Nevada: Sandia National Laboratories. ACC: DOC.20070928.0011; LLR.20080414.0012.

SNL 2008a. *Features, Events, and Processes for the Total System Performance Assessment: Analyses.* ANL-WIS-MD-000027 REV 00. Las Vegas, Nevada: Sandia National Laboratories. ACC: DOC.20080307.0003; DOC.20080407.0009; LLR.20080522.0166; DOC.20080722.0002.

SNL 2008b. *Total System Performance Assessment Model /Analysis for the License Application.* MDL-WIS-PA-000005 REV 00 AD 01. Las Vegas, Nevada: Sandia National Laboratories. ACC: DOC.20080312.0001; LLR.20080414.0037; LLR.20080507.0002; LLR.20080522.0113; DOC.20080724.0005.

Wilder, D.G.; Lin, W.; Blair, S.C.; Buscheck, T.; Carlson, R.C.; Lee, K.; Meike, A.; Ramirez, A.L.; Wagoner, J.L.; and Wang, J. 1997. *Large Block Test Status Report*. UCRL–ID–128776. Livermore, California: Lawrence Livermore National Laboratory.

NOTE: [a]Provided as an enclosure to letter from Williams to Sulima dtd 02/17/2009. "Yucca Mountain – Request for Additional Information Re: License Application (Safety Analysis Report Section 2.1), Safety Evaluation Report Volume 3 – Postclosure Chapters 2.2.1.1 and 2.2.1.3.7 – Submittal of Department of Energy Reference Citations."